Physics and Astrophysics of Compact Objects

Contents

1 Topics

The study of compact objects such as white dwarfs, neutron stars, and black holes requires the interplay between nuclear and atomic physics together with relativistic field theories, e.g., general relativity, quantum electrodynamics, quantum chromodynamics, as well as particle physics. In addition to the theoretical physics aspects, studying astrophysical scenarios characterized by the presence of at least one of the above compact objects is the focus of extensive research within our group, e.g., the physics of pulsars. This research can be divided into the following topics:

- **Nuclear and Atomic Astrophysics**. We study the properties and processes occurring in compact stars in which nuclear and atomic physics have to be necessarily applied. We focus on the properties of nuclear matter under extreme conditions of density, pressure, and temperature in compact star interiors. The matter equation of state is studied in detail, considering all the interactions between the constituents within a fully relativistic framework.

- **White Dwarfs Physics and Structure**. The aim of this part of our research is to construct the white dwarf structure within a self-consistent description of the equation of state of the interior together with the solution of the hydrostatic equilibrium equations in general relativity. Non-magnetized, magnetized, non-rotating, and rotating white dwarfs are studied. The interaction and evolution of a central white dwarf with a surrounding disk, as occurred in the aftermath of white dwarf binary mergers, is also a subject of study.

- **White Dwarfs Astrophysics**. We are interested in the astrophysics of white dwarfs, both isolated and in binaries. Magnetized white dwarfs, soft gamma repeaters, anomalous X-ray pulsars, white dwarf pulsars, cataclysmic variables, binary white dwarf mergers, and type Ia supernovae are studied. The role of a realistic white dwarf interior structure is particularly emphasized.

- **Neutron Stars Physics and Structure**. We calculate the properties of the interior structure of neutron stars using realistic models of the nuclear matter equation of state within the general relativistic equilibrium equations. Strong, weak, electromagnetic, and gravitational interactions have to be jointly taken into due account within a self-consistent, fully relativistic framework. Non-magnetized, magnetized, non-rotating, and rotating neutron stars are studied.

- **Neutron Stars Astrophysics**. We study astrophysical systems harboring neutron stars, such as isolated and binary pulsars, low and intermediate X-ray binaries, and merging double neutron stars and neutron star-white dwarf binaries. Most extreme cataclysmic events involving neutron stars and their role in explaining extraordinarily energetic astrophysical events such as gamma-ray bursts are analyzed in detail.

- **Black Hole Physics and Astrophysics**. We study the role of black holes in relativistic astrophysical systems such as gamma-ray bursts, active galactic nuclei, and galactic cores. Special attention is given to applying the theory of test particle motion both in the neutral and charged case and general relativity tests.

- **Radiation Mechanisms of Compact Objects**. We here study possible emission mechanisms of compact objects such as white dwarfs, neutron stars, and black holes. We are interested in the electromagnetic, neutrino, and gravitational-wave emission in compact object magnetospheres and accretion disks surrounding them, as well as inspiraling and merging relativistic binaries (double neutron stars, neutron star-white dwarfs, white dwarf-white dwarf, and neutron star-black holes). We also study the radiation from particle acceleration near stellar-mass and supermassive black holes by surrounding electromagnetic fields.

- **Exact and Numerical Solutions of the Einstein and Einstein-Maxwell Equations in Astrophysics**. We analyze the ability of analytic exact solutions of the Einstein and Einstein-Maxwell equations to describe the exterior spacetime of compact stars such as white dwarfs and neutron stars. For this, we compare and contrast exact (analytic) solutions with numerical solutions of the stationary axisymmetric Einstein equations. The problem of matching between interior and exterior spacetime is addressed in detail. The effect of the quadrupole moment on the proper-

ties of the spacetime is also investigated. Particular attention is given to applying exact solutions in astrophysics, e.g., the dynamics of particles around compact stars and their relevance in astrophysical systems such as X-ray binaries and gamma-ray bursts.

- **Critical Fields and Non-linear Electrodynamics Effects in Astrophysics**. We study the conditions under which ultrastrong electromagnetic fields can develop in astrophysical systems such as neutron stars and the process of gravitational collapse to a black hole. The effects of non-linear electrodynamics minimally coupled to gravity are investigated. New analytic and numeric solutions to the Einstein-Maxwell equations representing black holes or the exterior field of a compact star are obtained and analyzed. The consequences on extreme astrophysical systems, for instance, gamma-ray bursts, are studied.

2 Participants

2.1 ICRANet

- C. L. Bianco (ICRANet, Italy)
- J. A. Rueda (ICRANet, Italy)
- L. Li (ICRANet, Italy)
- R. P. Kerr (ICRANet, Italy; University of Canterbury, New Zeland)
- R. Ruffini (ICRANet, Italy)
- N. Sahakyan (ICRANet, Armenia)
- G. Vereschagin (ICRANet, Italy)
- S.-S. Xue (ICRANet, Italy)
- Y. Wang (ICRANet, Italy)

2.2 External collaborations: professors and senior researchers

- C. Arguelles (Universidad de La Plata, Argentina)
- K. Belczynski (Nicolaus Copernicus Astronomical Center, Polish Academy of Sciences, Poland)
- K. Boshkayev (Al-Farabi Kazakh National University, Kazakhstan)
- M. Bulla (Università degli Studi di Ferrara, Italy)
- R. Camargo (Universidade do Estado de Santa Catarina, Brazil)

- G. A. Carvalho (Universidade Tecnológica Federal do Paraná, Brazil; Universidade do Vale do Paraíba, Brazil; Instituto Tecnológico de Aeronáutica, Brazil)
- F. Cipolletta (Barcelona Supercomputing Center, Spain)
- C. Cherubini (Università Campus Biomedico, Italy)
- J. G. Coelho (Universidade Federal do Espírito Santo, Brazil)
- E. O. da Silva (Universidade Federal do Cariri, Brazil)
- J. C. N. de Araujo (Instituto Nacional de Pesquisas Espaciais, Brazil)
- R. C. dos Anjos (Universidade Federal do Paraná, Brazil; Universidade Federal da Fronteira Latino-Americana, Brazil; Universidade Tecnológica Federal do Paraná, Brazil)
- A. Drago (INFN, Università degli Studi di Ferrara, Italy)
- S. Filippi (Università Campus Biomedico, Italy)
- C. L. Fryer (Los Alamos National Laboratory, USA; University of Arizona, USA)
- G. A. González (Universidad Industrial de Santander, Colombia)
- C. Guidorzi (Università degli Studi di Ferrara, Italy)
- F. D. Lora-Clavijo (Universidad Industrial de Santander, Colombia)
- P. Lorén Aguilar (University of Exeter, United Kingdom)
- S. O. Kepler (Universidade Federal do Rio Grande do Sul, Brazil)
- M. Malheiro (Instituto Tecnológico de Aeronáutica, Brazil)
- R. M. Jr. Marinho (Instituto Tecnológico de Aeronáutica, Brazil)
- D. P. Menezes (Universidade Federal de Santa Catarina, Brazil)
- M. F. Mestre (Universidad de La Plata, Argentina; Instituto de Astrofisica de La Plata, Argentina)

- R. Moradi (Institute of High-Energy Physics, China; ICRANet, Italy)
- L. A. Nuñez (Universidad Industrial de Santander, Colombia)
- C. V. Rodrigues (Instituto Nacional de Pesquisas Espaciais, Brazil)
- G. Pagliara (INFN, Università degli Studi di Ferrara, Italy)
- C. Providência (University of Coimbra, Portugal)
- F. Rastegarnia (Institute of High-Energy Physics, China; ICRANet, Italy)
- C. A. Z. Vasconcellos (Universidade Federal do Rio Grande do Sul, Brazil)
- F. Tobias (Instituto Tecnológico de Aeronáutica, Brazil)
- J. D. Uribe-Suarez (Universidad Santiago de Cali, Colombia)
- F. Weber (San Diego State University, USA; University of California at San Diego, USA)
- J. I. Zuluaga (Universidad de Antioquia, Colombia)

2.3 Postdocs

- E. A. Becerra (Universidad Industrial de Santander, Colombia)
- L. Becerra (Universidad Industrial de Santander, Colombia)
- S. Campion (INFN, Sapienza University of Rome, Italy)
- R. V. Lobato (Universidad de los Andes, Bogotá, Colombia; Texas A&M University-Commerce, Commerce, USA)
- J. P. Pereira (Nicolaus Copernicus Astronomical Center, Polish Academy of Sciences, Poland)
- J. F. Rodriguez (Universidad Industrial de Santander, Colombia)
- M. F. Sousa (Universidade Federal do Paraná, Brazil)

2.4 Graduate Students

- S. V. Borges (University of Wisconsin-Milwaukee, USA)
- V. Crespi (Universidad de La Plata, Argentina)
- K. Kianfar (Instituto Tecnológico de Aeronáutica, Brazil)
- T. Ottoni (Universidade Federal do Espírito Santo, Brazil)
- G. Nurbakyt (Al-Farabi Kazakh National University, Kazakhstan)
- S. Zhang (University of Science and Technology of China, China; Università degli Studi di Ferrara, Italy)

3 Highlights 2023

The year 2023 has seen the consolidation of our scientific production trend. It has been very prolific in terms of the amount of publications but, more importantly, in terms of the quality and relevance of our publications.

The analysis of astrophysical sources requires the interplay of different areas of physics and astronomy, the reason for which we could place some of our articles in any of the different reports. To avoid such an overlapping, the Editors discuss which section of the annual report would be the best place to include a publication with such features. Therefore, in this report, we have included six newly published articles and one currently under review for publication that strictly fit the description of this section's topics. Therefore, you will also find articles where the physics and astrophysics of compact objects have been relevant, e.g., the section dedicated to gamma-ray bursts and dark matter. We refer the reader to those sections for further details on those publications.

We would like to highlight the strengthening of our international collaborations for these achievements. The seven publications summarized in this report have seen the participation of scientists from Brazil, China, Colombia, Italy, Portugal, Spain, the United Kingdom, and the USA.

We would like to highlight two of these publications. First, the article by Sousa, M. F.; Coelho, J. G.; de Araujo, J. C. N.; Guidorzi, C.; Rueda, J. A., *On the Optical Transients from Double White-dwarf Mergers*, published in The Astrophysical Journal 958, 134 (2023). This paper has received attention from the scientific community and media. It has presented the relevant and concise prediction that the forthcoming Vera Rubin Observatory will be able to pinpoint a new class of ever-detected astrophysical sources at a pace of thousands a year: the merger of binary systems of white dwarfs. These results open the way to new research on these astrophysical sources, and the Vera Rubin Observatory and the Zwicky Transient Facility research teams are already collaborating with ICRANet scientists to prepare the observational campaigns of these sources.

Below, we report some of the press releases reporting the results of our

research team:

On the ICRANet website:
http://www.icranet.org/index.php?option=com_content&task=view&id=1032&Itemid=920

Press releases in Italy:

On the University of Ferrara website:
https://www.unife.it/it/notizie/2023/scienza-cultura-e-ricerca/origine-stelle-nane

On Ansa.it
https://www.ansa.it/emiliaromagna/notizie/2023/11/02/unife-in-team-per-scoprire-or 75f3c2be-3992-4df0-80a8-49db4a4d8fcd.html

On Ferraratoday.it:
https://www.ferraratoday.it/cronaca/astrofisica-unife-icranet-brasile-scoperta-ori html

On Ultimometro.it:
https://www.ultimometro.it/uncategorized/unife-in-team-per-scoprire-origine-delle- 235580/

On 30scienze.com:
https://30science.com/2023/11/news/unife-icranet-e-brasile-insieme-per-scoprire-lo

On Estense.com:
https://www.estense.com/2023/1047157/astrofisica-unife-icranet-e-brasile-insieme-p

Press releases in Brazil:

On the Universidade Tecnológica Federal do Paraná website:
https://portal.utfpr.edu.br/noticias/geral/divulgacao-cientifica/fusoes-estelares-

On the Universidade Federal do Espírito Santo website:
https://www.ufes.br/conteudo/estudo-conduzido-por-pesquisador-da-ufes-preve-observ

Another publication worth highlighting is *Extracting the energy and angular momentum of a Kerr black hole* by J. A. Rueda and R. Ruffini, published in The European Physical Journal C 83, 960 (2023). This paper presents, for the first time in fifty years of black hole physics research, a concrete example of an astrophysically plausible electromagnetic mechanism able to extract the energy of black holes to power the most powerful astrophysical sources: gamma-ray bursts and active galactic nuclei. Exciting new research avenues are now open for further scrutiny, and we are already actively working on them.

4 Publications 2023

4.1 Refereed Journals

4.1.1 Printed

1. Sousa, M. F.; Coelho, J. G.; de Araujo, J. C. N.; Guidorzi, C.; Rueda, J. A., *On the Optical Transients from Double White-dwarf Mergers*, The Astrophysical Journal 958, 134, 2023.

   Double white-dwarf (DWD) mergers are relevant astrophysical sources expected to produce massive, highly-magnetized WDs, type Ia supernovae (SNe), and neutron stars (NSs). Although they are expected to be numerous sources in the sky, their detection has evaded the most advanced transient surveys. This article characterizes the optical transient expected from DWD mergers in which the central remnant is a stable (sub-Chandrasekhar) WD. We show that the expansion and cooling of the merger's dynamical ejecta lead to an optical emission peaking at 1–10 d post-merger, with luminosities of 10^{40}–10^{41} erg s^{-1}. We present simulations of the light-curves, spectra, and the color evolution of the transient. We show that these properties, together with the estimated rate of mergers, are consistent with the absence of detection, e.g., by The Zwicky Transient Facility (ZTF). More importantly, we show that the Legacy Survey of Space and Time (LSST) of the Vera C. Rubin Observatory will likely detect a few/several hundred per year, opening a new window to the physics of WDs, NSs, and SN Ia.

2. Rodríguez, J. F.; Rueda, J. A.; Ruffini, R.; Zuluaga, J. I.; Blanco-Iglesias, J. M.; Lorén-Aguilar, P., *Chirping compact stars: gravitational radiation and detection degeneracy with binaries* , Journal of Cosmology and Astroparticle Physics 2023, 017, 2023.

   Compressible, Riemann S-type ellipsoids can emit gravitational waves (GWs) with a chirp-like behavior (hereafter *chirping* ellipsoids, CELs).

We show that the GW frequency-amplitude evolution of CELs (mass $\sim$ 1 $M_\odot$, radius $\sim 10^3$ km, polytropic equation of state with index $n \approx 3$) is indistinguishable from that emitted by double white dwarfs and by extreme mass-ratio inspirals (EMRIs) composed of an intermediate-mass (e.g. 10^3 $M_\odot$) black hole and a planet-like (e.g. 10^{-4} $M_\odot$) companion, in the frequency interval within the detector sensitivity band in which the GW emission of these systems is quasi-monochromatic. For reasonable astrophysical assumptions, the local universe density rate of CELs, double white dwarfs, and EMRIs in the mass range here considered are very similar, posing a detection-degeneracy challenge for space-based GW detectors. We outline the astrophysical implications of this CEL-binary detection degeneracy by space-based GW-detection facilities.

3. Rueda, J. A.; Ruffini, R., *Extracting the energy and angular momentum of a Kerr black hole*, The European Physical Journal C 83, 960, 2023.

   It has been thought for decades that rotating black holes (BHs) power the energetic gamma-ray bursts (GRBs) and active galactic nuclei (AGNs), but the mechanism that extracts the BH energy has remained elusive. We here show that the solution to this problem arises when the BH is immersed in an external magnetic field and ionized low-density matter. For a magnetic field parallel to the BH spin, the induced electric field accelerates electrons outward and protons inward in a conical region, centered on the BH rotation axis, and of semi-aperture angle $\theta \approx 60^\circ$ from the BH rotation axis. For an antiparallel magnetic field, protons and electrons exchange their roles. The particles that are accelerated outward radiate off energy and angular momentum to infinity. The BH powers the process by reducing its energy and angular momentum by capturing polar protons and equatorial electrons with net negative energy and angular momentum. The electric potential allows for negative energy states outside the BH ergosphere, so the latter does not play any role in this electrodynamical BH energy extraction process.

4. Becerra, L. M.; Fryer, C. L.; Rodriguez, J. F.; Rueda, J. A.; Ruffini, R., *Neutron Star Binaries Produced by Binary-Driven Hypernovae, Their Mergers, and the Link between Long and Short GRBs*, Universe 9, 332, 2023.

   The binary-driven hypernova (BdHN) model explains long gamma-ray bursts (GRBs) associated with supernovae (SNe) Ic through physical episodes that occur in a binary composed of a carbon-oxygen (CO) star

and a neutron star (NS) companion in close orbit. The CO core collapse triggers the cataclysmic event, originating the SN and a newborn NS (hereafter νNS) at its center. The νNS and the NS accrete SN matter. BdHNe are classified based on the NS companion fate and the GRB energetics, mainly determined by the orbital period. In BdHNe I, the orbital period is a few minutes, so the accretion causes the NS to collapse into a Kerr black hole (BH), explaining GRBs of energies $> 10^{52}$ erg. BdHN II, with longer periods of tens of minutes, yields a more massive but stable NS, accounting for GRBs of 10^{50}–10^{52} erg. BdHNe III have still longer orbital periods (e.g., hours), so the NS companion has a negligible role, which explains GRBs with a lower energy release of $< 10^{50}$ erg. BdHN I and II might remain bound after the SN, so they could form NS-BH and binary NS (BNS), respectively. In BdHN III, the SN likely disrupts the system. We perform numerical simulations of BdHN II to compute the characteristic parameters of the BNS left by them, their mergers, and the associated short GRBs. We obtain the mass of the central remnant, whether it is likely to be a massive NS or a BH, the conditions for disk formation and its mass, and the event's energy release. The role of the NS nuclear equation of state is outlined.

5. Pereira, J. P.; Rueda, J. A., *Matching Slowly Rotating Spacetimes Split by Dynamic Thin Shells*, Universe 9, 305, 2023.

   We investigated within the Darmois–Israel thin-shell formalism the match of neutral and asymptotically flat, slowly rotating spacetimes (up to second order in the rotation parameter) when their boundaries are dynamic. It has several important applications in general relativistic systems, such as black holes and neutron stars, which we exemplify. We mostly focused on the stability aspects of slowly rotating thin shells in equilibrium and the surface degrees of freedom on the hypersurfaces splitting the matched slowly rotating spacetimes, e.g., surface energy density and surface tension. We show that the stability upon perturbations in the spherically symmetric case automatically implies stability in the slow rotation case. In addition, we show that, when matching slowly rotating Kerr spacetimes through thin shells in equilibrium, the surface degrees of freedom can decrease compared to their Schwarzschild counterparts, meaning that the energy conditions could be weakened. The frame-dragging aspects of the match of slowly rotating spacetimes are also briefly discussed.

6. Wang, Yu; Becerra, L. M.; Fryer, C. L.; Rueda, J. A.; Ruffini, R., *GRB 171205A: Hypernova and Newborn Neutron Star*, The Astrophysical Journal 945, 95, 2023.

   GRB 171205A is a low-luminosity, long-duration gamma-ray burst (GRB) associated with SN 2017iuk, a broad-line type Ic supernova (SN). It is consistent with having been formed in the core collapse of a widely separated binary, which we have called the binary-driven hypernova of type III. The core collapse of the CO star forms a newborn NS (νNS) and the SN explosion. Fallback accretion transfers mass and angular momentum to the νNS, here assumed to be born non-rotating. The accretion energy injected into the expanding stellar layers powers the prompt emission. The multiwavelength power-law afterglow is explained by the synchrotron radiation of electrons in the SN ejecta, powered by energy injected by the spinning νNS. We calculate the amount of mass and angular momentum gained by the νNS and the νNS rotational evolution. The νNS spins up to a period of 47 ms, then releases its rotational energy, powering the synchrotron emission of the afterglow. The paucity of the νNS spin explains the low-luminosity characteristic and that the optical emission of the SN from the nickel radioactive decay outshines the optical emission from the synchrotron radiation. From the νNS evolution, we infer that the SN explosion had to occur at most 7.36 h before the GRB trigger. Therefore, for the first time, the analysis of the GRB data leads to the time of occurrence of the CO core collapse, leading to the SN explosion and the electromagnetic emission of the GRB event.

4.1.2 Submitted for publication

1. Becerra, L. M.; Cipolletta, F.; Fryer, C. L.; Menezes, D. P.; Providência, C.; Rueda, J. A.; Ruffini, R., *Occurrence of gravitational collapse in the accreting neutron stars of binary-driven hypernovaer*, submitted to The Astrophysical Journal.

   The binary-driven hypernova (BdHN) model proposes long gamma-ray bursts (GRBs) originate in binaries composed of a carbon-oxygen (CO) star and a neutron star (NS) companion in close orbit. The CO core collapse triggers the GRB. It generates a newborn NS (νNS) and a supernova (SN) that accretes onto the NS and the νNS. The accre-

tion is highly super-Eddington, rapidly transferring mass and angular momentum to the stars. We perform three-dimensional, smoothed-particle-hydrodynamics simulations of BdHNe. We use up-to-date nuclear equations of state (EOS), with and without hyperons, to describe the NS interior and calculate the structure evolution in full general relativity. We assess the binary parameters leading either NS to the critical mass for gravitational collapse into a black hole (BH) and the occurrence time, $t_{\rm col}$. We include a non-zero angular momentum of the NSs: $t_{\rm col}$ ranges from seconds to hours for decreasing NS initial angular momentum values. BdHNe I, the most compact (about five minutes orbital period) and energetic, releasing $\gtrsim 10^{52}$ erg, show prompt BH formation. They form NS-BH binaries with tens of kyr merger timescale by gravitational-wave emission. BdHNe II do not form BHs and release $\lesssim 10^{52}$ erg. They form NS-NS binaries with similar merger timescales. In some BdHNe II, either NS can become supramassive, i.e., above the critical mass of a non-rotating NS. Magnetic braking can lead to a delayed collapse into a BH in tens of days for 10^{13} G magnetic field, leading to BH-BH or NS-BH with tens of kyr merger timescale.

The Astrophysical Journal, 958:134 (7pp), 2023 December 1 https://doi.org/10.3847/1538-4357/ad022f

On the Optical Transients from Double White-dwarf Mergers

M. F. Sousa[1,2,3], J. G. Coelho[2,4], J. C. N. de Araujo[2], C. Guidorzi[5,6,7], and J. A. Rueda[3,5,8,9,10]
[1] Programa de Pós-Graduação em Física e Astronomia, Universidade Tecnológica Federal do Paraná, Avenida sete de setembro 3165, 80230-901, Curitiba, PR, Brazil
[2] Divisão de Astrofísica, Instituto Nacional de Pesquisas Espaciais, Avenida dos Astronautas 1758, 12227–010, São José dos Campos, SP, Brazil
[3] ICRANet,-Ferrara, Dipartimento di Fisica e Scienze della Terra, Università degli Studi di Ferrara, Via Saragat 1, I-44122 Ferrara, Italy
[4] Núcleo de Astrofísica e Cosmologia (Cosmo-Ufes) and Departamento de Física, Universidade Federal do Espírito Santo, 29075–910, Vitória, ES, Brazil
[5] Department of Physics and Earth Science, University of Ferrara, Via Saragat 1, I-44122 Ferrara, Italy
[6] INFN—Sezione di Ferrara, Via Saragat 1, I-44122 Ferrara, Italy
[7] INAF—Osservatorio di Astrofisica e Scienza dello Spazio di Bologna, Via Piero Gobetti 101, I-40129 Bologna, Italy
[8] ICRANet, Piazza della Repubblica 10, I-65122 Pescara, Italy
[9] ICRA, Dipartamento di Fisica, Sapienza Università di Roma, Piazzale Aldo Moro 5, I-00185 Rome, Italy
[10] INAF, Istituto di Astrofisica e Planetologia Spaziali, Via Fosso del Cavaliere 100, I-00133 Rome, Italy
Received 2023 July 20; revised 2023 September 1; accepted 2023 October 9; published 2023 November 20

Abstract

Double white dwarf (DWD) mergers are relevant astrophysical sources expected to produce massive, highly magnetized white dwarfs (WDs), supernovae (SNe) Ia, and neutron stars (NSs). Although they are expected to be numerous sources in the sky, their detection has evaded the most advanced transient surveys. This article characterizes the optical transient expected from DWD mergers in which the central remnant is a stable (sub-Chandrasekhar) WD. We show that the expansion and cooling of the merger's dynamical ejecta lead to an optical emission peaking at 1–10 days postmerger, with luminosities of 10^{40}–10^{41} erg s^{-1}. We present simulations of the light curves, spectra, and the color evolution of the transient. We show that these properties, together with the estimated rate of mergers, are consistent with the absence of detection, e.g., by the Zwicky Transient Facility. More importantly, we show that the Legacy Survey of Space and Time of the Vera C. Rubin Observatory will likely detect a few/several hundred per year, opening a new window to the physics of WDs, NSs, and SNe Ia.

Unified Astronomy Thesaurus concepts: White dwarf stars (1799); Stellar mergers (2157); Compact binary stars (283); Compact objects (288); Visible sources (2108)

1. Introduction

The number of double white dwarfs (DWDs) in the Milky Way (MW) merging within a Hubble time has been estimated to be (5–7) $\times$ 10^{-13} yr^{-1} $M_{\odot}^{-1}$ (Maoz & Hallakoun 2017; Maoz et al. 2018). Using a stellar mass and density of MW-like galaxies of $6.4 \times 10^{10}\,M_{\odot}$ and $0.016\,\mathrm{Mpc}^{-3}$ (Kalogera et al. 2001), it translates into a local cosmic merger rate of $\mathcal{R}_{\rm DWD} \approx (5\text{–}7) \times 10^{5}\ \mathrm{Gpc}^{-3}\,\mathrm{yr}^{-1}$. The above classifies DWD mergers among the most numerous cataclysmic events.

Three fates of the central remnant of a DWD merger can be envisaged: a fast-rotating (and possibly highly magnetized) white dwarf (WD), a supernova (SN) of Type Ia, or a neutron star (NS). The binary's component masses, the presence (or genesis) of high magnetic fields (García-Berro et al. 2012), and the rate of mass and angular momentum transfer from a surrounding debris disk are among the critical physical ingredients that determine the central object's fate (see, e.g., Becerra et al. 2018b, 2019, and references therein). Based on the above, the relevance of DWDs has been highlighted in various astrophysical scenarios, e.g.,:

1. The double-degenerate scenario (Iben & Tutukov 1984; Webbink 1984) proposes that unstable thermonuclear fusion can be ignited in the central remnant of DWD mergers, leading to one of the most likely explanations of SNe Ia (see, e.g., Neopane et al. 2022 and references therein). Indeed, the DWD merger rate is sufficient to explain the rate of SNe Ia, which is about 5–8 times smaller (see, e.g., Ruiter et al. 2009; Maoz et al. 2018).
2. DWD mergers have been, for a long time, thought to be the main channel leading to the observed WDs with high magnetic fields in the range 10^{6}–10^{9} G (Külebi et al. 2009; Ferrario et al. 2015; Kepler et al. 2016).
3. A fraction of DWD mergers can explain the population of massive WDs of $\sim$1 $M_{\odot}$ (see Maoz et al. 2018; Cheng et al. 2020; Kilic et al. 2023b, and references therein). See also Section 4.
4. Interestingly, most of those massive WDs are highly magnetic (see, e.g., Kepler et al. 2016). Additionally, Legacy Survey of Space and Time (LSST) will observe more than 150 million WDs at the final depth of its stacked 10 yr survey (Fantin et al. 2020).
5. Indeed, it has been shown that the recently discovered isolated, highly magnetic, rapidly rotating WDs, Zwicky Transient Facility (ZTF) J190132.9+145808.7 (Caiazzo et al. 2021), and SDSS J221141.80+113604.4 (Kilic et al. 2021) could have been formed in DWD mergers (see Sousa et al. 2022 for details).
6. Massive, highly magnetized, fast-rotating WDs formed in DWD mergers have been proposed to explain soft gamma repeaters and anomalous X-ray pulsars, i.e., magnetars (Malheiro et al. 2012; Rueda et al. 2013; Coelho & Malheiro 2014; Coelho et al. 2014, 2017; Mukhopadhyay & Rao 2016; Cáceres et al. 2017; Otoniel et al. 2019; Sousa et al. 2020a, 2020b; Borges et al. 2020), fast radio bursts (Kashiyama et al. 2013), and overluminous SNe Ia (Das et al. 2013; Deb et al. 2022).

7. The Laser Interferometer Space Antenna expects to detect the gravitational-wave (GW) radiation from many compact (orbital periods shorter than hours), detached DWDs (see, e.g., Stroeer & Vecchio 2006; Carvalho et al. 2022; Korol et al. 2022).

Despite the above theoretical and observational richness, additional physical phenomena in DWD mergers have remained unexplored. We aim to characterize them in this article. First of all, given that $\mathcal{R}_{\rm DWD} \sim (5\text{–}8)\mathcal{R}_{\rm SN-Ia}$, we must conclude that there is a considerable population of DWD mergers that do not produce SNe Ia (see, also, Cheng et al. 2020). This article focuses on such systems, especially those where the central remnant is a massive WD (see Section 2). Section 3 shows that the dynamical ejecta from DWD mergers produces a fast-rising and fast-declining optical emission, peaking at ∼1 day postmerger, from its cooling driven by the expansion. The energy injected by the central remnant (e.g., by accretion winds and/or pulsar-like emission) is considered. We exemplify such optical transient theoretically and observationally using fiducial model parameters. Section 4 discusses how our findings compare with the known optical transients population. We show the Bright Transient Survey (Perley et al. 2020) of ZTF has not detected/identified any of them.

Finally, we discuss our main conclusions in Section 5, including the consistency of our theoretical predictions with the lack of detections by the ZTF of DWD mergers' optical transients. Furthermore, we provide an upper limit for the number of detections expected by the forthcoming LSST of the Vera C. Rubin Observatory. Details on the theoretical modeling of the expected light curves and spectra are given in the Appendix.

2. Merging Binary and Postmerger Configuration Properties

We are interested in DWD mergers leading to a central remnant that is a stable, sub-Chandrasekhar WD. Given the mass distribution of observed WDs, we expect that sub-Chandra mergers can lead to massive WDs in the $1.0 \lesssim M \lesssim 1.4\ M_\odot$ range. In principle, such WDs might be fastly rotating with periods $P \gtrsim 0.5$ s (see, e.g., Boshkayev et al. 2013). Such postmerged WD can avoid exploding as an SN Ia if, during its evolution, its central density remains below some specific value estimated to be a few 10^9 g cm^{-3} (see, e.g., Becerra et al. 2018b, 2019, and references therein for details).

Numerical simulations show that the merger of a DWD, in general, develops a rigidly rotating, central core surrounded by a hot, convective corona with differential rotation and a Keplerian disk that hosts nearly all the mass of the disrupted secondary star (Benz et al. 1990; Guerrero et al. 2004; Lorén-Aguilar et al. 2009; Longland et al. 2012; Raskin et al. 2012; Zhu et al. 2013; Dan et al. 2014; Becerra et al. 2018b). These compact-object mergers expel small amounts of mass in the dynamical phase of the merger. Dan et al. (2014) provided analytic functions that fit the results of their numerical simulations. Concerning the ejected mass, it can be estimated by

$$m_{\rm ej} \approx \frac{0.0001807M}{-0.01672 + 0.2463q - 0.6982q^2 + q^3}, \qquad (1)$$

where $M = m_1 + m_2$ is the total binary mass and $q \equiv m_2/m_1 \leqslant 1$ is the binary mass ratio. Equation (1) tells us that, typically, DWD mergers eject $m_{\rm ej} \sim 10^{-3}\ M_\odot$. Despite this amount of matter being negligible relative to the system mass, we will show that it is responsible for the transient electromagnetic emission in the early postmerger evolution.

Table 1
Parameter Values Used to Model Thermal and Synchrotron Radiation from the Expansion of Ejected Material

Parameter	Fiducial Value
$m_{\rm ej}$ ($10^{-3}\ M_\odot$)	1.00
n	1.00
m	9.00
$R_{*,0}$ (10^{11} cm)	1.00
$v_{*,0}$ (10^9 cm s^{-1})	1.00
H_0 (10^{46} erg s^{-1})	1.00
t_c/t_*	1.00
δ	1.30
κ (cm^2 g^{-1})	0.20

3. Expected Light Curves and Spectra

We now turn to the results from modeling the emission of the expanding ejecta. As we have recalled, about $10^{-3}\ M_\odot$ are ejected from the system during the final dynamical phase of the merger. This ejecta expands nearly radially at about the escape velocity, namely, 10^8–10^9 cm s^{-1}. In the early postmerger evolution, accretion winds further power the ejecta (see, e.g., Becerra et al. 2018a; Rueda et al. 2019). Magnetic braking and nuclear reactions can also contribute to the energy budget but to a much lesser extent, unless the central remnant is a superChandsekhar WD or a neutron star (see, e.g., Yu et al. 2019). In Appendix, we present our theoretical model to calculate the thermal evolution of the expanding ejecta subjected to the injection of energy from the central remnant. The model parameters are the ejecta mass ($m_{\rm ej}$), the index defining the radial falloff of the density profile (m), the self-similar expansion index (n), the initial position and velocity of the innermost ejecta layer ($R_{*,0}$ and $v_{*,0}$), the parameters defining the power injected by the central remnant (H_0, t_c, and δ), and the optical opacity (κ). We refer the reader to Appendix for technical details.

Table 1 lists the model parameters and the corresponding fiducial values we adopted to exemplify the model. Figure 1 shows the corresponding light curves (luminosity as a function of time), predicted by the theoretical model in Appendix, in the visible (r band) and the infrared (i and K_s bands).

From the light curves in Figure 1, we see that the thermal emission due to the expansion of the ejecta peak luminosity is $\sim 10^{40}$–10^{41} erg s^{-1}, at about 11–12 days postmerger. The transparency time is $t_{{\rm tr},*} \approx 1.55 \times 10^5$ s $\approx$1.79 days. Figure 2 shows the spectra $\nu F(\nu, t)$ at selected times, where $F(\nu, t) = J_{\rm cool}(\nu, t)$ is the spectral density, as given by Equation (A16).

4. DWD Population, Merger Rate, and Massive WDs

Although the electromagnetic detection of DWDs is a challenging observational task, the increasing quality, sensitivity, and capacity of performing accurate surveys by novel optical observational facilities (e.g., the SDSS, ZTF, and Gaia) and the refinement of observational techniques have led to a tenfold increase in the number of observed DWDs in the MW in the last 20 yr: from around 14 by 2000 (Nelemans et al. 2001) to about 150 by 2022 (Korol et al. 2022). That number

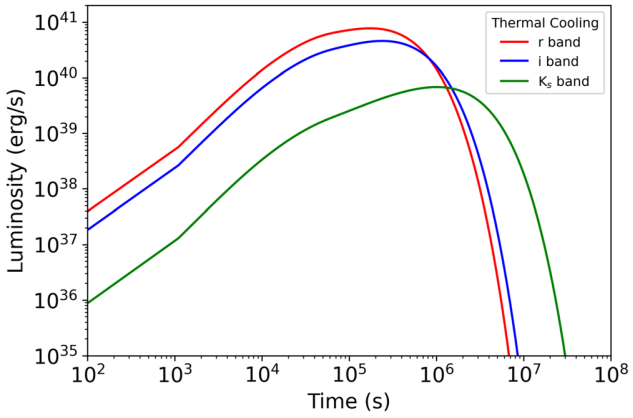

Figure 1. Emission from the expanding, cooling ejecta at early times (solid lines) in the visible (r band) and in the infrared (i and K_s bands). We refer to Appendix for details on the theoretical model.

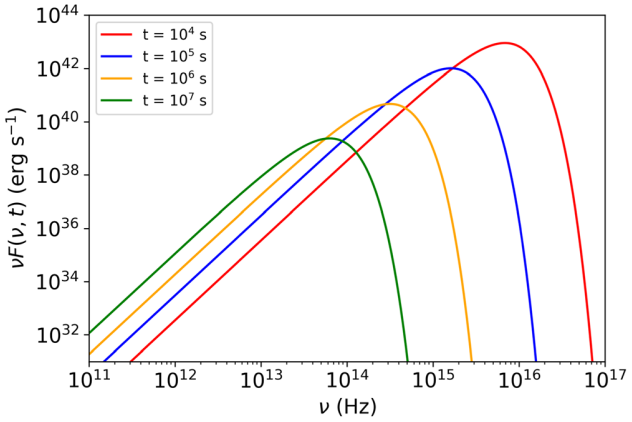

Figure 2. Emission spectra from the expanding, cooling ejecta at selected postmerger times. We refer to Appendix for details on the theoretical model.

has already increased (see, e.g., Kosakowski et al. 2023), also in view of the rapidly growing number of observed WDs in binaries in recent data from the Gaia Mission and ZTF, of which an appreciable percentage are expected to be DWDs (see, e.g., Brown et al. 2023; Jiménez-Esteban et al. 2023; Kosakowski et al. 2023; Parsons et al. 2023).

Using population synthesis models that matched the at-the-time number of observed DWDs, i.e., 14, in their pioneering work, Nelemans et al. (2001) estimated the MW hosts about 2.5×10^8 DWDs and a DWD merger rate $\approx 2.2 \times 10^{-2}$ yr^{-1}. Up-to-date analyses that match the increasing number of known DWDs have confirmed their estimate. We shall use the estimates by Maoz et al. (2018), to which we refer the reader for details. They estimated a DWD merger rate per WD of $\mathcal{R}_{\rm DWD} = (9.7 \pm 1.1) \times 10^{-12}$ yr^{-1}. This estimate can be translated into a DWD merger rate per unit stellar mass by dividing it by the stellar mass to WD number ratio (15.5 ± 1.8) $M_\odot$ per WD, leading to $\mathcal{R}_{\rm DWD} \approx (5\text{–}7) \times 10^{-13}$ yr^{-1} $M_\odot^{-1}$. It is worth noticing that this number agrees with the initial estimate by Nelemans et al. (2001) when multiplied by the MW stellar mass. Assuming a constant star formation rate over the MW lifetime, these figures imply that $\sim$10% of the Galactic WDs have merged with another WD. Therefore, as discussed in Maoz et al. (2018), this inferred fraction of already-merged DWDs may explain the high-mass bump in the WD mass function (see also Kilic et al. 2023b). However, some massive WDs may have formed from different channels (see, e.g., the case of J004917.14-252556.81 in Kilic et al. 2023a).

The above result agrees with our basic assumption that a considerable fraction of DWD mergers do not lead to SNe Ia but to massive WDs (rapidly rotating and possibly highly magnetic). Therefore, attention must be given to the possibility of establishing the link between observed massive WDs and their possible DWD merger progenitors. The success of this task needs the observational determination of the WD parameters (e.g., mass, radius, rotation period, temperature, and magnetic field strength) and the accurate modeling of the merger and postmerger evolution of the system. Fortunately, there is a growing effort in both directions. Numerical simulations focusing on the merging phase of DWDs started in the '90s and have considerably improved over the years (see, e.g., Benz et al. 1990; Guerrero et al. 2004; Lorén-Aguilar et al. 2009; Longland et al. 2012; Raskin et al. 2012; Zhu et al. 2013; Dan et al. 2014; Becerra et al. 2018b). Theoretical analyses to constrain the physics of the postmerger remnant and to determine its possible fate either as a disrupting explosion (SN Ia); a stable, massive WD; or gravitational collapse to an NS, including magnetic fields, rotation, and general relativistic effects, have also gained interest and been performed in the last decade (see, e.g., Schwab et al. 2012; Shen et al. 2012; Ji et al. 2013; Kashiyama et al. 2013; Beloborodov 2014; Schwab et al. 2016; Becerra et al. 2018b; Rueda et al. 2018; Shen et al. 2019; Neopane et al. 2022). Although there is still room for improvements in the merger and postmerger modeling, these works have already allowed us to test the viability of the connection between massive WDs and their possible DWD progenitors on a theoretical basis. For instance, Sousa et al. (2022) has positively assessed such a connection for the isolated, highly magnetic, rapidly rotating WDs ZTF J190132.9 +145808.7 (Caiazzo et al. 2021) and SDSS J221141.80 +113604.4 (Kilic et al. 2021), leading to the parameters of the possible DWD progenitor, which were found to agree with those of the DWD observed population.

Having set the theoretical and observational basis for the connection between DWD mergers and massive WDs, we next discuss the electromagnetic transient associated with such an astrophysical system, theoretically featured in Section 2, from the observational viewpoint.

5. Observed Populations of Fast Transients

In the last decades, the advent of wide-field, high-cadence surveys led to the discovery of several classes of fast ($t_{\rm rise} \lesssim$ 10 days) transients, with luminosities spanning several decades (see Pastorello & Fraser 2019 for a review). The so-called "fast blue optical transients" (FBOTs) are blue and fast rising, with peak luminosities in the range $-16 \gtrsim M_{g,\rm peak} \gtrsim -22$ (e.g., Drout et al. 2014; Tanaka et al. 2016; Pursiainen et al. 2018; Tampo et al. 2020) and are also referred to as "rapidly evolving transients" or "fast-evolving luminous transients." The source AT2018cow (known as "the cow"), at 60 Mpc, represents the best-studied case of this class. It exhibited some unprecedented characteristics: rise time of a few days; $L_p \sim 4 \times 10^{44}$ erg s^{-1}; mostly featureless spectra with blackbody temperatures above 10^4 K during the first 15 days with large expansion velocities ($\sim 0.1c$); hard X-ray and variable soft X-ray emission; and radio brightness with $L_{\nu,p} \sim 4 \times 10^{28}$ erg s^{-1} Hz^{-1} at 8.5 GHz (Ho et al. 2019; Margutti et al. 2019; Perley et al. 2019; see also Coppejans et al. 2020; Ho et al. 2020; Perley et al. 2021;

Ho et al. 2023; Matthews et al. 2023 for the few analogous cases yet observed). These properties suggest that a large amount of radioactive nickel cannot explain the high luminosity, and the relatively short effective diffusion timescale points to a low ejecta mass. In contrast, the long-lived X-ray variability suggests a compact and long-lived inner engine. Owing to their extreme peak luminosity from radio to hard X-rays, these FBOTs are hardly compatible with a DWD merger since the power injected from the central remnant at those times is lower than the observed luminosities.

In parallel, other transients that share comparably fast rise times (∼12–15 days) but are significantly less luminous have also been discovered, with peak luminosities in the gap between novae and supernovae. A class that raised interest is that of so-called calcium-rich transients ($-13 \gtrsim M_V \gtrsim -17$; Perets et al. 2010; Kasliwal et al. 2012; De et al. 2020), which exhibit a strong [Ca II] emission in the nebular phase spectra with a high [Ca II]/[O I] ratio. These share similar photospheric velocities with typical core-collapse Ib/c SNe. Still, their environment is strongly different from the latter since they prefer remote locations in the outskirts of early-type galaxies, even more than Type Ia SNe and short gamma-ray bursts, indicative of a very old progenitor population (Lunnan et al. 2017). In this respect, a fraction of these transients could result from mergers of helium and oxygen/neon WDs (Shen et al. 2019). The local volumetric rate of Ca-rich, hydrogen-poor transients is estimated to be ≳15% of the Type Ia rate (De et al. 2020). The variety in peak luminosity and spectroscopic properties probably stems from a heterogeneous class of progenitors.

Some low-luminosity gap transients are still likely to be less energetic SNe. In particular, the so-called intermediate-luminosity red transients (Berger et al. 2009; Bond et al. 2009) have a peak luminosity in the range $-12 \gtrsim M_V \gtrsim -15$, relatively long rise times and postpeak plateaus that resemble Type II-L and II-P SNe. Although there is consensus that the progenitors are 8–15 $M_\odot$ stars in dusty cocoons, eruptive formation of a massive WD or eruptions from binary interactions could contribute to the observed population (Pastorello & Fraser 2019).

A few gap transients $M_V \gtrsim -13$ mag, characterized by double or even triple-peaked light curves, have been proposed as a scaled-up version of red novae (typically less luminous than −10 mag) and, as such, are often referred to as luminous red novae (see Kulkarni et al. 2007; Pastorello et al. 2019 and references therein). Their photometric evolution is reminiscent of eruptive variables such as V1309 Scorpii, whose final brightening was interpreted as the merger of a contact binary (Tylenda et al. 2011).

Figure 3 summarizes the zoo of the fast transients as observed with the ZTF Bright Transient Survey (Perley et al. 2020) in the peak luminosity–duration plane. We show the region where our predictions on DWD mergers lie: despite the relatively high expected volumetric rate, this region is still poorly explored. Upcoming surveys such as the LSST (Ivezić et al. 2019) are expected to boost the number of promising candidates for DWD mergers.

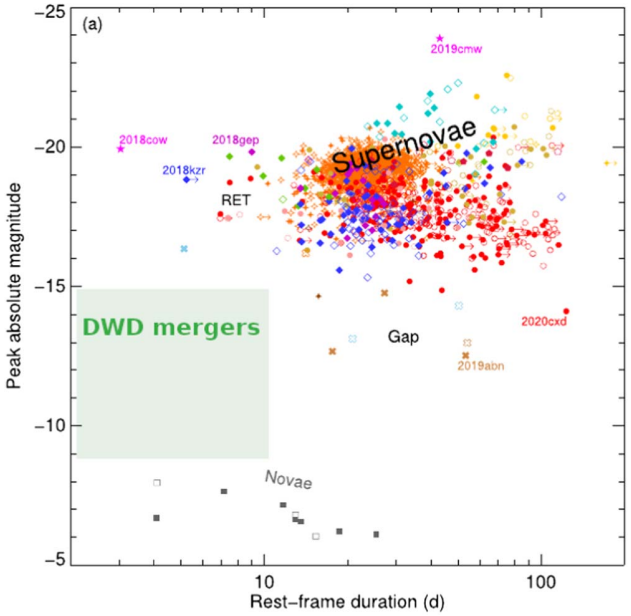

Figure 3. Different populations of fast transients observed with the ZTF Bright Transient Survey (Perley et al. 2020). The shaded box highlights where we expect most DWD mergers should lie. Figure adapted from Perley et al. (2020).

6. Discussion and Conclusions

We have estimated the optical transient from DWD mergers leading to stable, massive, fast-rotating WDs. The emission arises from the cooling down of the dynamical ejecta of the merger, about $10^{-3} M_\odot$, that expands at 10^8–10^9 cm s^{-1}. The ejecta is powered by the early activity of the central remnant, mainly fallback accretion (see, e.g., Rueda et al. 2019, and references therein, and Appendix for a comparison of accretion power with nuclear energy and magnetic braking). Inspired by numerical simulations, we assumed spherical expansion. The theoretical model includes a power-law density profile and self-similar expansion. We solve the energy balance equation and determine the ejecta's thermal history (time evolution), estimating its photospheric emission and color evolution.

We have shown that the peak of the optical emission occurs at times 1–10 days, with a luminosity $L_p = 10^{40}$–10^{41} erg s^{-1}, for typical parameters expected for these DWD mergers (see Table 1); see Figures 1 and 2 for the light curves and spectra, respectively. Although our model makes some approximations, we expect it to catch the main physics of these systems robustly. Therefore, further model refinements should not appreciably change the above qualitative and quantitative picture.

With this in mind, we turned to the observational considerations. Indeed, detecting the optical counterpart of DWD mergers would have several relevant consequences in physics and astrophysics. To mention some:

1. It will constrain the fraction of mergers producing SNe Ia, giving crucial hints for the SN Ia–associated physics, e.g., the unstable thermonuclear fusion and detonation (see Schwab et al. 2012; Shen et al. 2012; Ji et al. 2013; Schwab et al. 2016; Neopane et al. 2022; and references therein).
2. If the rate of mergers leading to SN Ia will turn out lower than the SN Ia observed rate, it would imply the necessity of also having at work the single-degenerate scenario for their explanation (see, e.g., Han & Podsiadlowski 2004).
3. It will alert facilities on ground and space to look for associated emissions at higher energies, e.g., in the X- and gamma-rays, constraining the physics of the central remnant such as magnetic fields and rotation

(see, e.g., Ji et al. 2013; Kashiyama et al. 2013; Beloborodov 2014; Becerra et al. 2018b; Rueda et al. 2018).
4. It will confirm DWD mergers as the formation channel of massive, fast-rotating WDs.
5. At late postmerger times, the central WD might be observed accompanied by a debris disk (see, e.g., Külebi et al. 2013; Rueda et al. 2013; Becerra et al. 2018b; Neopane et al. 2022; and references therein). Thus, it will be interesting to compare forthcoming advanced infrared-optical-UV survey estimates of the rate of WDs with debris disk (Fantin et al. 2020) and the DWD merger rate estimates.
6. It will constrain the physics of the gravitational collapse of WDs into NSs while simultaneously possibly confirming DWD mergers as a formation channel of NSs.

Thus, in Section 4, we checked whether current observational facilities could have observed such optical transients. We compare and contrast the model predictions with the emergence population of optical transients in the literature. Our analysis showed that the optical transients from DWD mergers presented here do not match the observed features of FBOTs, fast-evolving luminous transients (i.e., cow-like objects), and calcium-rich transients. A plot of the peak absolute magnitude as a function of the rest-frame time duration for the transients detected by the ZTF Bright Transient Survey (see Figure 3), highlighting the region the DWD merger optical transients should occupy, reveals overwhelmingly the above result.

Therefore, no optical transient from DWD mergers has ever been detected. Does this result agree with the model prediction? The limiting magnitude for detection by ZTF is $m_{\rm ZTF,\ lim} = 19$ mag (Perley et al. 2020). Assuming the peak luminosity $L_p = 10^{40}$ erg s^{-1}, this turns into a detection horizon $d_{\rm ZTF,lim} \sim 11$ Mpc. Using an expected volumetric rate for DWD mergers of 4×10^5 Gpc^{-3} yr^{-1} (see Section 1), the upper limit to the expected number of events by ZTF is $\sim$2, considering the duty cycle of the survey. This result is consistent with our findings and the expectation that not all DWD mergers produce stable WDs: a fraction should lead to SNe Ia and another to NSs as central remnants.

We can apply the same kind of calculation to LSST, for which 5σ limiting magnitudes for single exposures in filters g and r (the same considered for ZTF in Figure 3) are 24.5 and 24.0, respectively.[11] Under these favorable conditions, the detection horizon becomes $d_{\rm LSST,lim} \sim$ 110–140 Mpc, corresponding to a gain by $\sim 10^3$ in the expected detection rate.

The above analysis brings us to one of the main conclusions: in the transition from ZTF to LSST, the electromagnetic (optical) counterparts of DWD mergers will finally become observable, likely a few/several hundred per year, opening a new window to the physics of WDs, NSs, and SN Ia.

Acknowledgments

M.F.S. thanks CAPES-PrInt (88887.351889/2019-00) and Fundação Araucária for the financial support. J.G.C. is grateful for the support of FAPES (1020/2022, 1081/2022, 976/2022, 332/2023), CNPq (311758/2021-5), and FAPESP (2021/01089-1). J.C.N.A. thanks CNPq (307803/2022-8) for partial financial support.

[11] https://www.lsst.org/scientists/keynumbers

Appendix
Emission from the Cooling of the Expanding Ejecta

For modeling the thermal emission of the expanding ejecta, we must consider that the layers reach transparency at different times in a nonhomogeneous distribution of matter. The present model generalizes the model presented in Rueda et al. (2019). Numerical simulations show that the ejected matter expands nearly radially, so we consider a spherically symmetric distribution. The ejecta extends at radii $r_i \in [R_*, R_{\rm max}]$, with corresponding velocities $v_i \in [v_*, v_{\rm max}]$, in self-similar expansion

$$r_i(t) = r_{i,0}\hat{t}^n, \quad v_i(t) = n\frac{r_i(t)}{t} = v_{i,0}\hat{t}^{n-1}, \tag{A1}$$

where $\hat{t} \equiv t/t_*$, being $t_* \equiv nR_{*,0}/v_{*,0}$ the characteristic expansion timescale, which is the same for all layers given the condition of self-similarity. Here, $r_{i,0}$ and $v_{i,0}$ are the initial radius and velocity of the layer. The case $n = 1$ corresponds to a uniform expansion.

The density at the position $r = r_i$ is given by

$$\rho(r_i) = \frac{(3-m)}{4\pi}\frac{m_{\rm ej}}{R_{*,0}^3}\frac{(R_*/r_i)^m}{\left[\left(\frac{R_{\rm max}}{R_*}\right)^{3-m} - 1\right]}\hat{t}^{-3n}, \tag{A2}$$

where $m_{\rm ej}$ is the total mass of the ejecta, and m is a positive constant. The distribution and time evolution given by Equation (A2) ensure that at any time, the total mass of the ejecta, i.e., the volume integral of the density, equals $m_{\rm ej}$.

We divide the ejecta into N shells defined by the $N+1$ radii

$$r_{i,0} = R_{*,0} + i\frac{(R_{\rm max,0} - R_{*,0})}{N}, \quad i = 0, 1, \ldots, N, \tag{A3}$$

so the width and mass of each shell are, respectively, $\Delta r = (R_{\rm max} - R_*)/N$, and

$$\begin{aligned} m_i &= \int_{r_i}^{r_{i+1}} 4\pi r^2 \rho(r) dr \\ &\approx \frac{4\pi}{m-3} r_i^3 \rho(r_i)\left[1 - \left(1 + \frac{\Delta r}{r_i}\right)^{3-m}\right], \end{aligned} \tag{A4}$$

so given the decreasing density with distance, the inner layers are more massive than the outer layers. The number of shells to be used must satisfy the constraint that the sum of the shells' mass gives the total ejecta mass, i.e.,

$$\sum_{j=1}^{N} m_j = m_{\rm ej}. \tag{A5}$$

We have introduced the discrete index $j = i + 1$ to differentiate the counting of the shells from the counting of radii given by Equation (A3). In this work, we use $N = 100$ shells, ensuring that Equation (A5) is satisfied with 99% of accuracy.

Under the assumption that the shells do not interact with each other, we can estimate the evolution of the ith shell from the energy conservation equation

$$\dot{E}_i = -P_i\,\dot{V}_i - L_{{\rm cool},i} + H_{{\rm inj},i}, \tag{A6}$$

where $V_i = (4\pi/3)r_i^3$, E_i, and P_i are the volume, energy, and pressure of the shell, while $H_{{\rm inj},i}$ is the power injected from the

central remnant that is thermalized in the shell, and

$$L_{\mathrm{cool},i} \approx \frac{cE_i}{r_i(1+\tau_{\mathrm{opt},i})} \tag{A7}$$

is the bolometric luminosity radiated by the shell, $\tau_{\mathrm{opt,i}}$ being the optical depth.

Assuming a spatially constant gray opacity throughout the ejecta, the optical depth of the radiation emitted by the ith layer is given by

$$\tau_{\mathrm{opt,i}} = \int_{\infty}^{r_i} \kappa\rho(r)dr = \int_{R_{\max}}^{r_i} \kappa\rho(r)dr = \tau_{i,0}\hat{t}^{-2n},$$
$$\tau_{i,0} \equiv \frac{m-3}{m-1}\frac{\kappa m_{\mathrm{ej}}}{4\pi R_{*,0}^2}\frac{\left[\left(\frac{R_*}{r_i}\right)^{m-1} - \left(\frac{R_*}{r_{\max}}\right)^{m-1}\right]}{\left[1-\left(\frac{R_*}{R_{\max}}\right)^{m-3}\right]}, \tag{A8}$$

where we have used Equation (A2), and κ is the opacity.

We adopt a radiation-dominated equation of state for the ejecta, so at every position, $E_i \approx 3P_i\,V_i$. The power injected into the ejecta originates from the newborn central WD (Rueda et al. 2019). This energy is absorbed and thermalized, becoming a heating source for the expanding matter. The power-law decreasing density, Equation (A2), suggests that the more inner the layer, the more radiation it should absorb. To account for this effect, we weigh the heating source for each shell using the mass fraction, i.e.,

$$H_{\mathrm{inj},i} = \frac{m_i}{m_{\mathrm{ej}}}H_{\mathrm{inj}}, \tag{A9}$$

where m_i is the shell's mass, and adopt the following form for the heating source

$$H_{\mathrm{inj}} = H_0\left(1+\frac{t}{t_c}\right)^{-\delta}, \tag{A10}$$

where H_0 and δ are model parameters. This function can model the power injected by the pulsar's spindown by magnetic braking and accretion winds. We expect that power released from accretion dominates the early times. For instance, for fallback accretion parameters $H_0 = 10^{46}$ erg s^{-1}, $\delta = 1.3$, and $t_c = t_*$ (Rueda et al. 2019), with $t_* = 10^2$ s, we obtain $H_{\mathrm{inj}} \approx 2\times 10^{43}$ erg s^{-1} at $t = 10^4$ s. We can set an upper limit on the energy injected from nuclear reactions, e.g., by nickel decay, assuming nickel amounts to the entire ejecta mass, i.e., $M_{\mathrm{Ni}} = m_{\mathrm{ej}} \sim 10^{-3}M_\odot$. In that case, reactions would inject $L_{\mathrm{Ni}} = 3.9\times 10^{10}M_{\mathrm{Ni}}\,e^{-t/(8.8\,d)} \sim 10^{41}$ erg s^{-1} by that time, which is still much smaller than the expected power injected by fallback accretion. Likewise, magnetic braking leads to negligible energy injection from rotational energy loss at early times. For example, a WD with a dipole magnetic field of strength $B_d = 10^9$ G, radius $R = 10^8$ cm, initial rotation period $P_0 = 10$ s ($\Omega_0 = 2\pi/P_0 \approx 0.6$ rad s^{-1}), and moment of inertia $I = 10^{49}$ g cm^2 has a characteristic magnetic braking timescale $t_{\mathrm{sd}} = T/L_{\mathrm{sd}} \approx 2\times 10^7$ yr, where $T = (1/2)I\Omega_0^2$ is the initial rotational energy and $L_{\mathrm{d}} = (2/3)B_d^2R^6\Omega_0^4/c^3$ the initial spindown power due to magnetic dipole braking. Therefore, at times $t \lesssim t_{\mathrm{sd}} \approx 6\times 10^{14}$ s, the spindown power is $L_{\mathrm{d}} \approx 4\times 10^{33}$ erg s^{-1}. From the above, we safely assume a single source of injection power, modeled by Equation (A10), bearing in mind that other power inputs could be considered but which should have a negligible effect in the early postmerger transient.

The position of the shell that reaches transparency gives the photospheric radius at a time t. Namely, the shell's position with optical depth $\tau_{\mathrm{opt,\ i}}[r_i(t)] = 1$. Using Equation (A8), we obtain

$$R_{\mathrm{ph}} = \frac{R_{\max,0}\hat{t}^n}{\left[1+\frac{m-1}{m-3}\frac{4\pi R_{*,0}^2}{\kappa m_{\mathrm{ej}}}\frac{\left[1-\left(\frac{R_*}{R_{\max}}\right)^{m-3}\right]}{\left(\frac{R_*}{R_{\max}}\right)^{m-1}}\hat{t}^{2n}\right]^{\frac{1}{m-1}}}. \tag{A11}$$

Equation (A11) shows that when the entire ejecta is optically thick, $R_{\mathrm{ph}} = R_{\max}$. Then, the transparency reaches the inner shells to the instant over which $R_{\mathrm{ph}} = R_*$, at $t = t_{\mathrm{tr},*}$, when the entire ejecta has become transparent. The time $t_{\mathrm{tr},*}$ is found from the condition $\tau_{\mathrm{opt},*}[R_*(t_{\mathrm{tr},*})] = 1$, and is given by

$$\hat{t}_{\mathrm{tr},*} = \left\{\frac{m-3}{m-1}\frac{\kappa m_{\mathrm{ej}}}{4\pi R_{*,0}^2}\left(\frac{R_*}{R_{\max}}\right)^{m-1}\frac{\left[\left(\frac{R_{\max}}{R_*}\right)^{m-1}-1\right]}{\left[1-\left(\frac{R_*}{R_{\max}}\right)^{m-3}\right]}\right\}^{\frac{1}{2n}}. \tag{A12}$$

At $t < t_{\mathrm{tr},*}$, the photospheric radius evolves as $R_{\mathrm{ph}} \propto t^{\frac{n(m-3)}{m-1}}$, while at later times, $R_{\mathrm{ph}} \propto t^n$.

The sum of the luminosity of the shells gives the bolometric luminosity

$$L_{\mathrm{bol}} = \sum_{j=1}^{N} L_{\mathrm{cool},j}, \tag{A13}$$

so the effective temperature of the blackbody emission, T_s, can be obtained from the Stefan–Boltzmann law, i.e.,

$$T_s = \left(\frac{L_{\mathrm{bol}}}{4\pi R_{\mathrm{ph}}^2\sigma}\right)^{1/4}, \tag{A14}$$

where σ is the Stefan–Boltzmann constant. The power per unit frequency, per unit area, is given by Planck's spectrum

$$B_\nu = \frac{2\pi h\nu^3}{c^2}\frac{1}{e^{\frac{h\nu}{k_BT_s}}-1}, \tag{A15}$$

where ν is the radiation frequency, h and k_B are the Planck and Boltzmann constants. Therefore, the spectral density (power per unit frequency) given by the thermal cooling at a frequency ν is

$$J_{\mathrm{cool}}(\nu, t) = 4\pi R_{\mathrm{ph}}^2(t)B_\nu(\nu, t), \tag{A16}$$

and the luminosity radiated in the frequency range $[\nu_1, \nu_2]$ can be then obtained as

$$L_{\mathrm{cool}}(\nu_1, \nu_2; t) = \int_{\nu_1}^{\nu_2} J_{\mathrm{cool}}(\nu, t)d\nu. \tag{A17}$$

The parameter $v_{\max,0}$ has no appreciable effect in the evolution, so it cannot be constrained from the data. This happens because most of the mass is concentrated in the innermost layers, so they dominate the thermal evolution. For self-consistency of the model, we have set $v_{\max,0} = 2v_{*,0}$ (so $R_{\max,0} = 2R_{*,0}$). As for the initial value of the internal

energy of the shells, $E_i(t_0)$, we have set them to the initial kinetic energy of each layer, $E_i = (1/2)m_i v_i(t_0)^2$.

ORCID iDs

M. F. Sousa https://orcid.org/0000-0002-5438-3460
J. G. Coelho https://orcid.org/0000-0001-9386-1042
J. C. N. de Araujo https://orcid.org/0000-0003-4418-4289
C. Guidorzi https://orcid.org/0000-0001-6869-0835
J. A. Rueda https://orcid.org/0000-0003-4904-0014

References

Becerra, L., Boshkayev, K., Rueda, J. A., & Ruffini, R. 2019, MNRAS, 487, 812
Becerra, L., Guzzo, M. M., Rossi-Torres, F., et al. 2018a, ApJ, 852, 120
Becerra, L., Rueda, J. A., Lorén-Aguilar, P., & García-Berro, E. 2018b, ApJ, 857, 134
Beloborodov, A. M. 2014, MNRAS, 438, 169
Benz, W., Cameron, A. G. W., Press, W. H., & Bowers, R. L. 1990, ApJ, 348, 647
Berger, E., Soderberg, A. M., Chevalier, R. A., et al. 2009, ApJ, 699, 1850
Bond, H. E., Bedin, L. R., Bonanos, A. Z., et al. 2009, ApJL, 695, L154
Borges, S. V., Rodrigues, C. V., Coelho, J. G., Malheiro, M., & Castro, M. 2020, ApJ, 895, 26
Boshkayev, K., Rueda, J. A., Ruffini, R., & Siutsou, I. 2013, ApJ, 762, 117
Brown, A. J., Parsons, S. G., van Roestel, J., et al. 2023, MNRAS, 521, 1880
Cáceres, D. L., de Carvalho, S. M., Coelho, J. G., de Lima, R. C. R., & Rueda, J. A. 2017, MNRAS, 465, 4434
Caiazzo, I., Burdge, K. B., Fuller, J., et al. 2021, Natur, 595, 39
Carvalho, G. A., Anjos, R. C. d., Coelho, J. G., et al. 2022, ApJ, 940, 90
Cheng, S., Cummings, J. D., Ménard, B., & Toonen, S. 2020, ApJ, 891, 160
Coelho, J. G., Cáceres, D. L., de Lima, R. C. R., et al. 2017, A&A, 599, A87
Coelho, J. G., & Malheiro, M. 2014, PASJ, 66, 14
Coelho, J. G., Marinho, R. M., Malheiro, M., et al. 2014, ApJ, 794, 86
Coppejans, D. L., Margutti, R., Terreran, G., et al. 2020, ApJL, 895, L23
Dan, M., Rosswog, S., Brüggen, M., & Podsiadlowski, P. 2014, MNRAS, 438, 14
Das, U., Mukhopadhyay, B., & Rao, A. R. 2013, ApJL, 767, L14
De, K., Kasliwal, M. M., Tzanidakis, A., et al. 2020, ApJ, 905, 58
Deb, D., Mukhopadhyay, B., & Weber, F. 2022, ApJ, 926, 66
Drout, M. R., Chornock, R., Soderberg, A. M., et al. 2014, ApJ, 794, 23
Fantin, N. J., Côté, P., & McConnachie, A. W. 2020, ApJ, 900, 139
Ferrario, L., de Martino, D., & Gänsicke, B. T. 2015, SSRv, 191, 111
García-Berro, E., Lorén-Aguilar, P., Aznar-Siguán, G., et al. 2012, ApJ, 749, 25
Guerrero, J., García-Berro, E., & Isern, J. 2004, A&A, 413, 257
Han, Z., & Podsiadlowski, P. 2004, MNRAS, 350, 1301
Ho, A. Y. Q., Perley, D. A., Gal-Yam, A., et al. 2023, ApJ, 949, 120
Ho, A. Y. Q., Perley, D. A., Kulkarni, S. R., et al. 2020, ApJ, 895, 49
Ho, A. Y. Q., Phinney, E. S., Ravi, V., et al. 2019, ApJ, 871, 73
Iben, I., Jr., & Tutukov, A. V 1984, ApJS, 54, 335
Ji, S., Fisher, R. T., García-Berro, E., et al. 2013, ApJ, 773, 136
Jiménez-Esteban, F. M., Torres, S., Rebassa-Mansergas, A., et al. 2023, MNRAS, 518, 5106
Ivezić, Ž., Kahn, S. M., Tyson, J. A., et al. 2019, ApJ, 873, 111
Kalogera, V., Narayan, R., Spergel, D. N., & Taylor, J. H. 2001, ApJ, 556, 340
Kashiyama, K., Ioka, K., & Mészáros, P. 2013, ApJL, 776, L39
Kasliwal, M. M., Kulkarni, S. R., Gal-Yam, A., et al. 2012, ApJ, 755, 161
Kepler, S. O., Pelisoli, I., Koester, D., et al. 2016, MNRAS, 455, 3413
Kilic, M., Córsico, A. H., Moss, A. G., et al. 2023a, MNRAS, 522, 2181
Kilic, M., Kosakowski, A., Moss, A. G., Bergeron, P., & Conly, A. A. 2021, ApJL, 923, L6
Kilic, M., Moss, A. G., Kosakowski, A., et al. 2023b, MNRAS, 518, 2341
Korol, V., Hallakoun, N., Toonen, S., & Karnesis, N. 2022, MNRAS, 511, 5936
Kosakowski, A., Brown, W. R., Kilic, M., et al. 2023, ApJ, 950, 141
Külebi, B., Ekşi, K. Y., Lorén-Aguilar, P., Isern, J., & García-Berro, E. 2013, MNRAS, 431, 2778
Külebi, B., Jordan, S., Euchner, F., Gänsicke, B. T., & Hirsch, H. 2009, A&A, 506, 1341
Kulkarni, S. R., Ofek, E. O., Rau, A., et al. 2007, Natur, 447, 458
Longland, R., Lorén-Aguilar, P., José, J., García-Berro, E., & Althaus, L. G. 2012, A&A, 542, A117
Lorén-Aguilar, P., Isern, J., & García-Berro, E. 2009, A&A, 500, 1193
Lunnan, R., Kasliwal, M. M., Cao, Y., et al. 2017, ApJ, 836, 60
Malheiro, M., Rueda, J. A., & Ruffini, R. 2012, PASJ, 64, 56
Maoz, D., & Hallakoun, N. 2017, MNRAS, 467, 1414
Maoz, D., Hallakoun, N., & Badenes, C. 2018, MNRAS, 476, 2584
Margutti, R., Metzger, B. D., Chornock, R., et al. 2019, ApJ, 872, 18
Matthews, D. J., Margutti, R., Metzger, B. D., et al. 2023, RNAAS, 7, 126
Mukhopadhyay, B., & Rao, A. R. 2016, JCAP, 2016, 007
Nelemans, G., Yungelson, L. R., Portegies Zwart, S. F., & Verbunt, F. 2001, A&A, 365, 491
Neopane, S., Bhargava, K., Fisher, R., et al. 2022, ApJ, 925, 92
Otoniel, E., Franzon, B., Carvalho, G. A., et al. 2019, ApJ, 879, 46
Parsons, S. G., Hernandez, M. S., Toloza, O., et al. 2023, MNRAS, 518, 4579
Pastorello, A., & Fraser, M. 2019, NatAs, 3, 676
Pastorello, A., Mason, E., Taubenberger, S., et al. 2019, A&A, 630, A75
Perets, H. B., Gal-Yam, A., Mazzali, P. A., et al. 2010, Natur, 465, 322
Perley, D. A., Fremling, C., Sollerman, J., et al. 2020, ApJ, 904, 35
Perley, D. A., Ho, A. Y. Q., Yao, Y., et al. 2021, MNRAS, 508, 5138
Perley, D. A., Mazzali, P. A., Yan, L., et al. 2019, MNRAS, 484, 1031
Pursiainen, M., Childress, M., Smith, M., et al. 2018, MNRAS, 481, 894
Raskin, C., Scannapieco, E., Fryer, C., Rockefeller, G., & Timmes, F. X. 2012, ApJ, 746, 62
Rueda, J. A., Boshkayev, K., Izzo, L., et al. 2013, ApJL, 772, L24
Rueda, J. A., Ruffini, R., Wang, Y., et al. 2018, JCAP, 10, 006
Rueda, J. A., Ruffini, R., Wang, Y., et al. 2019, JCAP, 2019, 044
Ruiter, A. J., Belczynski, K., & Fryer, C. 2009, ApJ, 699, 2026
Schwab, J., Quataert, E., & Kasen, D. 2016, MNRAS, 463, 3461
Schwab, J., Shen, K. J., Quataert, E., Dan, M., & Rosswog, S. 2012, MNRAS, 427, 190
Shen, K. J., Bildsten, L., Kasen, D., & Quataert, E. 2012, ApJ, 748, 35
Shen, K. J., Quataert, E., & Pakmor, R. 2019, ApJ, 887, 180
Sousa, M. F., Coelho, J. G., & de Araujo, J. C. N. 2020a, MNRAS, 492, 5949
Sousa, M. F., Coelho, J. G., & de Araujo, J. C. N. 2020b, MNRAS, 498, 4426
Sousa, M. F., Coelho, J. G., de Araujo, J. C. N., Kepler, S. O., & Rueda, J. A. 2022, ApJ, 941, 28
Stroeer, A., & Vecchio, A. 2006, CQGra, 23, S809
Tampo, Y., Tanaka, M., Maeda, K., et al. 2020, ApJ, 894, 27
Tanaka, M., Tominaga, N., Morokuma, T., et al. 2016, ApJ, 819, 5
Tylenda, R., Hajduk, M., Kamiński, T., et al. 2011, A&A, 528, A114
Webbink, R. F. 1984, ApJ, 277, 355
Yu, Y., Chen, A., & Wang, B. 2019, ApJ, 870, L23
Zhu, C., Chang, P., van Kerkwijk, M. H., & Wadsley, J. 2013, ApJ, 767, 164

Journal of Cosmology and Astroparticle Physics
An IOP and SISSA journal

Chirping compact stars: gravitational radiation and detection degeneracy with binaries

J.F. Rodríguez[a,c,*] **J.A. Rueda**,[b,c,d,e,f] **R. Ruffini**,[b,c,g] **J.I. Zuluaga**,[h] **J.M. Blanco-Iglesias**[i,j] **and P. Lorén-Aguilar**[i,j]

[a]Escuela de Física, Universidad Industrial de Santander,
Ciudad Universitaria, Bucaramanga 680002, Colombia
[b]ICRA, Dipartimento di Fisica, Sapienza Università di Roma,
Piazzale Aldo Moro 5, I-00185 Roma, Italy
[c]ICRANet, Piazza della Repubblica 10, I-65122 Pescara, Italy
[d]ICRANet-Ferrara, Dip. di Fisica e Scienze della Terra, Università di Ferrara,
Via Saragat 1, I-44122 Ferrara, Italy
[e]Dipartimento di Fisica e Scienze della Terra, Università di Ferrara,
Via Saragat 1, I-44122 Ferrara, Italy
[f]INAF, Istituto di Astrofisica e Planetologia Spaziali,
Via Fosso del Cavaliere 100, 00133 Rome, Italy
[g]Istituto Nazionale di Astrofisica,
Viale del Parco Mellini 84, I-00136 Rome, Italy
[h]Solar, Earth and Planetary Physics Group (SEAP) Instituto de Física — FCEN,
Universidad de Antioquia,
Calle 67 No. 53–108, Medellín, Colombia
[i]Departament de Física, Universitat Politècnica de Catalunya,
c/Esteve Terrades, 5, 08860 Castelldefels, Spain
[j]School of Physics, University of Exeter,
Stocker Road, Exeter EX4 4QL, U.K.

E-mail: joferoru@correo.uis.edu.co, jorge.rueda@icra.it, ruffini@icra.it,
jorge.zuluaga@udea.edu.co, josemiguelblancoiglesias@gmail.com,
P.Loren-Aguilar@exeter.ac.uk

Received February 1, 2023
Revised August 24, 2023
Accepted September 21, 2023
Published October 6, 2023

*Corresponding author.

https://doi.org/10.1088/1475-7516/2023/10/017

JCAP10(2023)017

Abstract. Compressible, Riemann S-type ellipsoids can emit gravitational waves (GWs) with a chirp-like behavior (hereafter *chirping* ellipsoids, CELs). We show that the GW frequency-amplitude evolution of CELs (mass $\sim 1\,\mathrm{M}_\odot$, radius $\sim 10^3\,\mathrm{km}$, polytropic equation of state with index $n \approx 3$) is indistinguishable from that emitted by double white dwarfs and by extreme mass-ratio inspirals (EMRIs) composed of an intermediate-mass (e.g. $10^3\,\mathrm{M}_\odot$) black hole and a planet-like (e.g. $10^{-4}\,\mathrm{M}_\odot$) companion, in the frequency interval within the detector sensitivity band in which the GW emission of these systems is quasi-monochromatic. For reasonable astrophysical assumptions, the local universe density rate of CELs, double white dwarfs, and EMRIs in the mass range here considered are very similar, posing a detection-degeneracy challenge for space-based GW detectors. We outline the astrophysical implications of this CEL-binary detection degeneracy by space-based GW-detection facilities.

Keywords: gravitational waves / sources, gravitational wave detectors, gravitational waves / experiments, gravitational waves / theory

ArXiv ePrint: 1907.10532

JCAP10(2023)017

Contents

1 Introduction

Space-based, gravitational wave (GW) interferometers such as *LISA* [1], *TianQin* [2] and *Taiji* [3] have the potential to detect low-frequency GWs and thus to give details of a different set of astrophysical objects with respect to the ones detectable by Earth-borne interferometers such as LIGO/Virgo. Specifically, *LISA* is sensitive to the frequency range 10^{-5}–1 Hz [4, 5], and *TianQin* in the range 10^{-4}–0.1 Hz [2].

Among the main astrophysical targets expected for these detectors are the so-called extreme mass-ratio inspirals (EMRIs), namely binaries with symmetric mass-ratios $\nu \equiv q/(1+q)^2 \approx q \equiv m_2/m_1 \ll 1$. EMRIs that fall within the aforementioned GW frequency range are, for example, binaries composed of a supermassive (e.g. $m_1 \sim 10^6$–$10^9\,\mathrm{M}_\odot$) or intermediate-mass (e.g. $m_1 \sim 10^2$–$10^3\,\mathrm{M}_\odot$) black hole, accompanied by a stellar-mass object (e.g. $m_2 \sim \mathrm{M}_\odot$) or, more interestingly (for the purposes of the present work), a substellar object (e.g. $m_2 \ll \mathrm{M}_\odot$), respectively (see eg. [6] and references therein).

Another target for GW detectors is represented by triaxial objects (e.g., deformed compact stars) emitting gravitational radiation while approaching axial symmetry. Searches for GWs from deformed neutron stars have been conducted in LIGO/Virgo detectors in the Hz-kHz band (e.g. [7, 8]). So far, no analogous sources in the sub-Hz frequency region appear to have been considered possible targets of *LISA* even for different types of stellar objects. These sources could help to test astrophysical and relativistic objects, such as white dwarfs and low-mass compact objects, in physical regimes not previously explored and with unprecedented precision.

We show in this work that:

1. Triaxial, white dwarf-like compact objects emit quasi-monochromatic detectable GWs in the *LISA* frequency sensitivity band;

2. Their GW emission (spectrum, spanned frequency range, and time evolution), becomes almost indistinguishable from that of some binaries, specifically detached double white dwarfs and EMRIs in the case of intermediate-mass black holes with planet-like companions.

JCAP10(2023)017

We aim to characterize the above detection degeneracy. This challenge makes difficult the unambiguous identification of these objects by space-based interferometers, also given their expected comparable rates.

The article is organized as follows. In section 2, we recall the main physical properties of the compressible, triaxial ellipsoid-like object relevant for this work, which we name *chirping ellipsoid* (CEL). The properties of the GW emission from a CEL are investigated in section 3. We identify white dwarf-like objects as the kind of CEL that could mimic the GW emission from some binaries. In section 4, we summarize the main quantities relevant to estimating the detectability by space-based interferometers of the GWs from CELs. We also define when we can consider GWs monochromatic in the interferometer band. Having defined these key ingredients, we identify in section 5 the binary systems for which a detection degeneracy with CEL occurs. We refer to them as CEL equivalent binaries. Section 6 is devoted to giving estimates of the rates of CEL and the equivalent binaries. Finally, in section 7, we draw our conclusions.

2 Evolution of compressible ellipsoids

The study of equilibrium configurations of rotating self-gravitating systems using analytic methods (e.g., [9]) allows us to estimate the gravitational radiation emitted by rotating stars. In [10–13] incompressible rotating stars were studied following a quasi-static evolution approach. In particular, it was shown that Kelvin's circulation, $C \equiv \pi a_1 a_2 (\zeta + 2\Omega)$,[1] is conserved when the dynamics is only driven by gravitational radiation reaction [13]. Hereafter, the principal axes of the ellipsoid are denoted by (a_1, a_2, a_3), the angular velocity of rotation around a_3 by Ω, and the vorticity in the same direction by ζ. In [14, 15] it was studied the GW emission of compressible, rotating stars with matter described by a polytropic equation of state, i.e., $P = K\rho^{1+1/n}$, where P is the pressure, ρ the matter density, and n and K are the polytropic index and constant.

We are interested in the GW emission of Riemann type-S ellipsoids [9], which are not axially symmetric but whose equilibrium sequences of constant circulation can be constructed.

There are two main sequences of rotating triaxial ellipsoids: the *Jacobi-like* (spinning-up by angular momentum loss) with $|\zeta| < 2|\Omega|$ and the *Dedekind-like* (spinning-down) with $|\zeta| > 2|\Omega|$ [14, 15]. For the purposes pursued here, we address systems along the Jacobi-like sequence and, in virtue of its expected radiation signature, we call them *chirping ellipsoids*, CEL.

Paper [15] studied the case of a newborn neutron star described by a polytropic index $n \leq 1$. In that case, the spin-up sequence has a first chirp-like epoch (i.e. frequency and amplitude increase; see figure 7 in [15]) and both the spin-down and spin-up epochs are in principle detectable by interferometers such as LIGO/Virgo [15, 16]. No other values of the polytropic index, of interest e.g. for white dwarfs, have been explored in depth.

We follow the treatment of compressible ellipsoids by [14, 17] and refer the reader there for technical details. The dynamical timescale, and hence the unit of time, in our calculations will be $\tau_{\rm CEL} = 1/\sqrt{\pi G \bar{\rho}_0}$, where $\bar{\rho}_0$ is the mean density of the non-rotating star with the same polytropic index and total mass M, but with radius R_0 different from the mean radius $R = (a_1 a_2 a_3)^{1/3}$ of the compressible ellipsoid [14].

When the polytropic index is close to 3, the value of $\Omega/\sqrt{\pi G \bar{\rho}_0}$ along the equilibrium sequence is of the order of 10^{-2}. With this information, we can infer the kind of astrophysical

[1] Not to be confused with the compactness parameter denoted by *calligraphic* $\mathcal{C}$.

JCAP10(2023)017

object whose GWs are within the frequency band of space-based detectors. For instance, for a GW frequency of the order of the minimum noise of *LISA* i.e. $f \sim 10\,\mathrm{mHz}$ (see figure 6 in section 4), then $\bar{\rho}_0 \sim 5 \times 10^7\,\mathrm{g\,cm^{-3}}$, which is a typical average density of a white dwarf (see, e.g., [18]).

3 GW emission of a CEL

In the weak-field, low-velocity approximation, the GW power of a rotating object is [19–21]

$$\frac{dE}{dt} = -\frac{32}{5}\frac{G}{c^5}\Omega^6(I_{11} - I_{22})^2, \tag{3.1}$$

where $I_{ii} = \kappa_n M a_i^2/5$, with κ_n a structure constant that depends on the polytropic index. We recall that the GW is quadrupole dominant and the angular frequency is twice the rotational one, i.e. $\omega = 2\Omega$.

The GW amplitude

$$h_0 = 4\frac{G}{c^4 D}(\pi f)^2(I_{11} - I_{22}), \tag{3.2}$$

where f is the GW frequency, and D is the distance to the source and the typical GW emission timescale,

$$\tau_{\mathrm{GW}} = \frac{f}{\dot{f}} = \Omega\frac{dE}{d\Omega}\frac{dt}{dE}, \tag{3.3}$$

are obtained from the equilibrium sequence of Riemann type-S ellipsoids described in section 2; see figure 1.

It can be seen from figure 1 that these CELs can be considered as *quasi-monochromatic*, i.e., $\tau_{\mathrm{GW}} \gg T_{\mathrm{obs}}$, where T_{obs} is the observing time of the space-based detector. This feature is very important to assess the detectability and degeneracy properties. Figure 1 also shows that these spin-up CELs have a chirp-like early epoch, i.e. both the frequency and amplitude increase with time.

Different circulations converge during this early phase, characterized by axes ratios $\lambda_2 = a_2/a_1, \lambda_3 = a_3/a_1 \lesssim 0.7$. The smaller the polytropic index, the more deformed the star is during this chirping epoch.

We have identified CELs with deformed white dwarf-like objects. We show in figure 3 isodensity contours of a CEL with polytropic index $n = 2.95$, when the axes ratios are $\lambda_2 = 0.74, \lambda = 0.80$. At this stage, the object rotates with angular velocity $\Omega/\sqrt{\pi G\bar{\rho}_0} = 0.037$. All the contours represent self-similar ellipsoids, and the density profile is the same as the one of the non-rotating polytrope with the same index n and radius R_0 [14], shown in figure 2. At this point of the evolution $R/R_0 = 14.81$, which implies that for a CEL with $M = 1.2\,\mathrm{M}_\odot$ the axes are $a_1 = 7.1 \times 10^9, a_2 = 5.2 \times 10^9, a_3 = 5.6 \times 10^9\,\mathrm{cm}$. When we compare with the simulations of double white dwarf mergers, evidently, there is a problem in scale that comes from the fact that the CEL is very expanded, nearly one order of magnitude compared with the non-rotating configuration. It is important to mention that this point of the CEL evolution is near the end of the chirp $\Omega_{\mathrm{end}}/\sqrt{\pi G\bar{\rho}_0} \approx 0.04$.

We advance the possibility that these CELs might be the aftermath of double white dwarf mergers. Numerical simulations (see, e.g., [22–26]) have shown that the merged object is composed of a central white dwarf made of the undisrupted primary white dwarf and a corona made with nearly half of the disrupted secondary. The central remnant is surrounded

JCAP10(2023)017

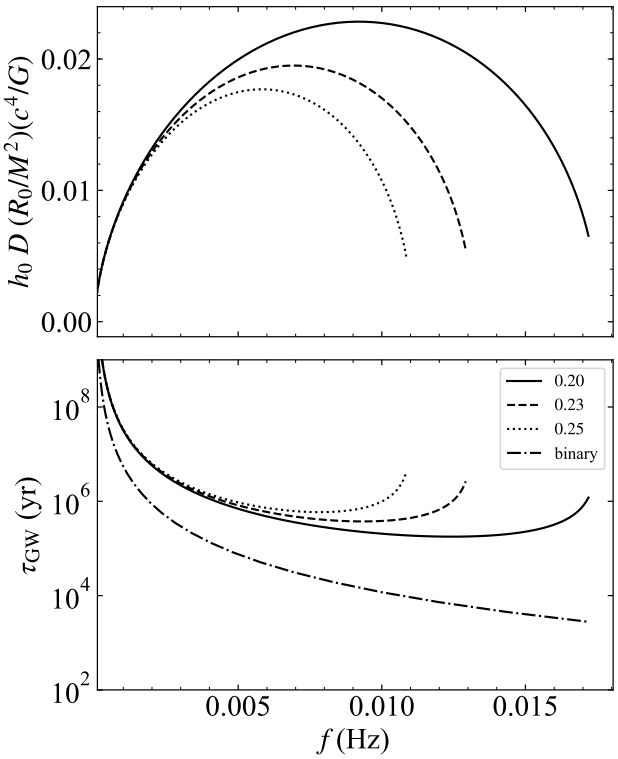

Figure 1. GW amplitude (upper panel) and timescale (lower panel) as a function of the GW frequency (in Hz) for a compressible CEL with polytropic index $n = 2.95$. The CEL mass is $M = 1.0\,\mathrm{M}_\odot$, the same as the non-rotating spherical star with radius $R \approx 6000\,\mathrm{km}$. For comparison purposes, the dot-dashed lines show a binary with chirp mass equal to the CEL mass. The systems are quasi-monochromatic, i.e. $\tau_{\rm GW} \gg T_{\rm obs}$, at the frequency band of spaced-borne detectors.

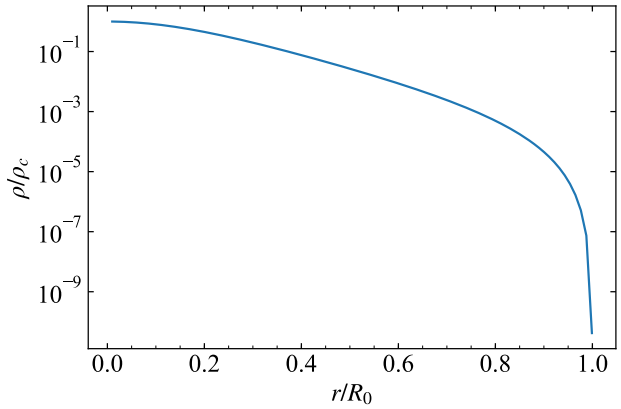

Figure 2. Density profile of a self-gravitating, non-rotating object whose internal matter is described by a polytropic equation of state with $n = 2.95$.

by a Keplerian disk with a mass given by the rest of the disrupted secondary because very little mass ($\sim 10^{-3}\,\mathrm{M}_\odot$) is ejected during the merger.

To validate the above hypothesis, we have performed smoothed-particle-hydrodynamics (SPH) simulations of double white dwarf mergers to compare the structure of the post-merger,

JCAP10(2023)017

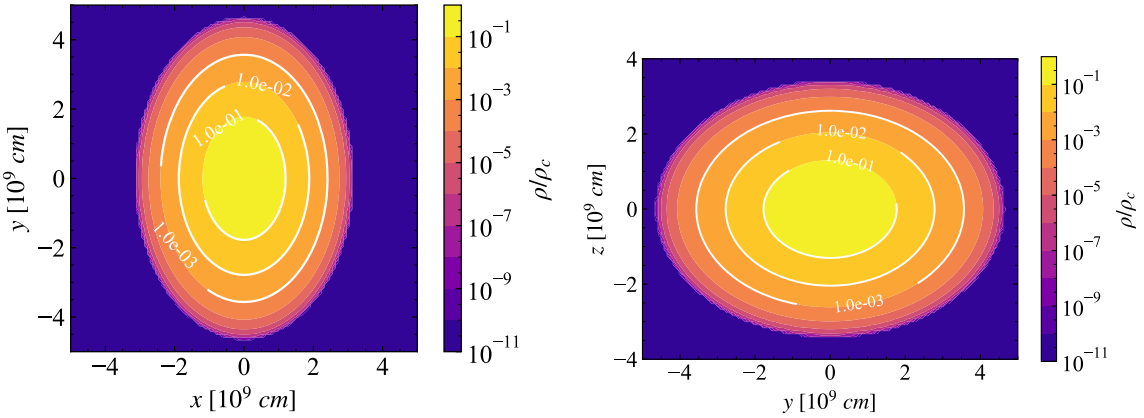

Figure 3. Isodensity curves of a CEL with polytropic index $n = 2.95$, $M_{\rm CEL} = 1.2\,{\rm M}_\odot$, and central density $\rho_c = 1.2 \times 10^8\,{\rm g\,cm^{-3}}$, rotating with angular velocity $\Omega/\sqrt{\pi G \bar{\rho}_0} = 0.037$. All the curves are *self-similar* to the ellipsoid with axes ratio $a2/a_1 = 0.74$ and $a_3/a_1 = 0.80$. The compactness of the corresponding non-rotating configuration, with the same mass, is $\mathcal{C} = 0.44 \times 10^{-4}$.

central white dwarf remnant with the one of the CEL. In figure 4, we show the density color map on the orbital and polar plane of a $0.6 + 0.6\,{\rm M}_\odot$ merger at about 9 orbital periods after the starting time of the mass transfer. The two white dwarfs have merged, forming a newborn central white dwarf remnant. By comparing figures 3 and 4, we can conclude that the density and radii of the central white dwarf, the product of a merger, are similar to the ones of our relevant CELs, which validate our initial guess.

Turning to the comparison with a binary, we computed, as a first guess, the GW emission for a binary with total mass, $M_{\rm bin} = m_1 + m_2$, and a chirp mass, $M_{\rm chirp} = M_{\rm bin}\nu^{3/5}$ ($\nu \approx q \equiv m_2/m_1$), equal to the mass of the CEL. We found that the timescale and amplitude evolution of the binary is of the same order of magnitude as the ones of a CEL. Hence, we conjecture that the two signals can have similar waveforms sweeping the same frequency interval simultaneously.

The GWs from these CELs, besides their early chirping-like behavior, are highly monochromatic. Hence, this poses a detection-degeneracy issue with other monochromatic systems, such as some kind of binaries, which we identify in section 5.

For a more detailed and quantitative study of the waveforms, we used the non-dimensional parameter

$$Q_\omega \equiv \frac{\omega^2}{\dot{\omega}} = \frac{d\phi}{d\ln\omega} = 2\pi\frac{dN}{d\ln f} = 2\Omega^2\frac{dE}{d\Omega}\frac{dt}{dE}, \tag{3.4}$$

where ϕ is GW phase and N the number of cycles. This parameter is an intrinsic measure of the phase-time evolution [29], and is (gauge) invariant under time and phase shifts.

We make an empirical fit of Q_ω for CEL with different indexes n, and different values of the compactness parameter $\mathcal{C} = GM_{\rm CEL}/(c^2 R_0)$. The fitting function is:

$$Q_\omega^{\rm CEL} \approx \frac{\mathcal{A}_n}{\mathcal{C}^{5/2}}\left[\frac{\omega}{\sqrt{\pi G\bar{\rho}_0}}\right]^\alpha \tag{3.5}$$

where the values of $\mathcal{A}_n$ and α, as obtained fitting the waveforms of CELs with different polytropic structure constants, are shown in table 1.

JCAP10(2023)017

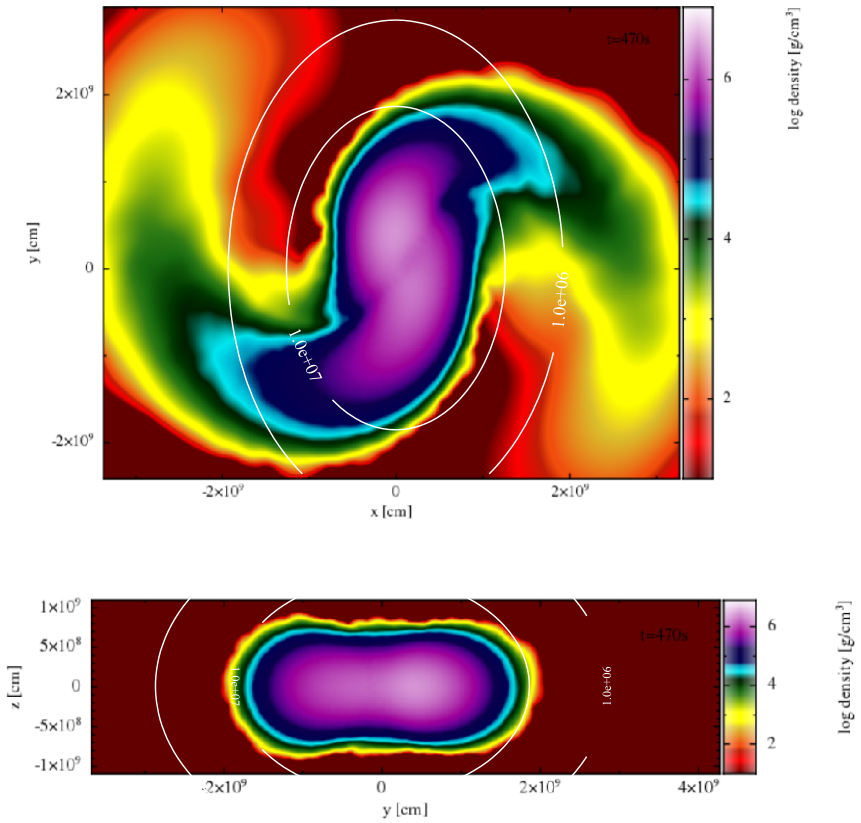

Figure 4. Density map of a section in the orbital plane (top panel) and in the polar plane (bottom panel) of a $0.6 + 0.6\,M_\odot$ double white dwarf merger simulated with 5×10^4 SPH particles. This snapshot is taken 9 orbital periods after mass transfer begins. The simulation was performed with an adapted version of PHANTOM [27]. This figure has been created using SPLASH (Price 2007), an SPH visualization tool publicly available at http://users.monash.edu.au/∼dprice/splash [28].

n	κ_n	k_1	k_2	k_3	$\mathcal{A}_n$	α
2.0	0.38712	1.1078	0.71618	1.6562	4.003	−1.222
2.5	0.27951	1.4295	0.67623	1.4202	4.060	−1.447
2.7	0.24109	1.55971	0.66110	1.33194	5.926	−1.365
2.9	0.20530	1.69038	0.64630	1.24621	4.940	−1.571
2.95	0.19676	1.72309	0.64265	1.22511	4.369	−1.614
2.97	0.19340	1.73617	0.64119	1.21669	3.760	−1.640
2.99	0.19005	1.74925	0.63973	1.20829	3.817	−1.652

Table 1. Polytropic structure constants $(n, \kappa_n, k_1, k_2, k_3)$ and the Q_ω power-law empirical fitting parameters.

The function Q_ω for both the CEL and the binary has a power-law behavior but with a different exponent. The negative exponent implies that both have a monotonically increasing frequency. In the case of the CEL, this behavior can be understood from the conservation of circulation and the interplay of compressibility and vorticity. Riemann S-type ellipsoids have internal motions with uniform vorticity contributing to the total angular momentum. In

JCAP10(2023)017

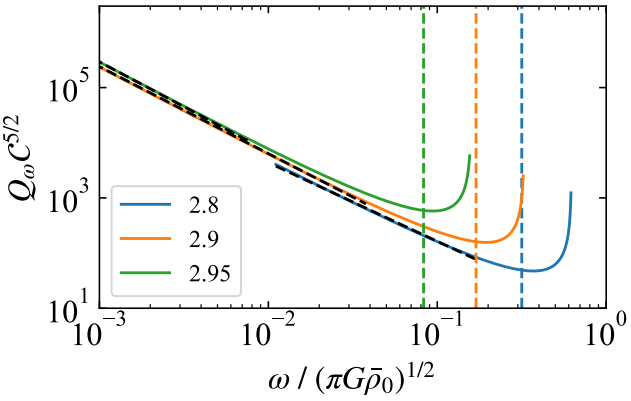

Figure 5. Intrinsic phase-time evolution for a Riemann S-type spinning-up ellipsoid (CEL) with polytropic indexes $n = 2.8, 2.9, 2.95$ (blue, orange, green), normalized by the compactness parameter $\mathcal{C}$. Fits are shown as black dashed curves. The vertical dashed line represents the end of the chirping regime for each index, i.e. the frequency where the GW amplitude reaches the maximum.

spin-up configurations, the radiation of angular momentum induces a vorticity loss. However, since the circulation is conserved, this loss must be compensated with a change in the angular velocity and the axes a_1, a_2. Thus, the spin-up of a CEL has two "components": one due to the change in geometry that depends on the compressibility, and the other one due to the decrease of vorticity. The compressibility of the object changes with the polytropic index, inducing the behavior seen in table 1 (e.g. when $n \to 3$ $\alpha \to -5/3$).[2]

Empirical power-laws, such as that in eq. (3.5), can be used to compute analytically the phase-time evolution of the GW. The frequency and phase are the functions of $\tau = t_\infty - t$, where t_∞ is the time the frequency formally diverges. For binaries with point-like components, the GW frequency diverges when the orbital separation approaches zero. In a real CEL, this time is never achieved since the object "leaves" the chirping regime at a time $t_{\rm end}$ with a finite angular frequency $\omega_{\rm end}$ (see dashed lines in figure 5).

4 GW detectability

For our analysis, we assume that the matched filtering technique is used to analyze the GW data. In this case, the expected signal-to-noise ratio is given by (see e.g. [32])

$$\left(\frac{S}{N}\right)^2 = \langle \rho^2 \rangle = 2 \times 4 \int_{f_0}^{f_1} \frac{\langle |F_+ \tilde{h}_+ + F_\times \tilde{h}_\times|^2 \rangle}{S_n(f)} df \tag{4.1}$$

where f_0 and f_1 are the initial and final observed GW frequencies, $\tilde{h}_+(f), \tilde{h}_\times(f)$ are the Fourier transforms of the GW polarizations, $F_+, F_\times$ are the detector antenna patterns, and $S_n(f)$ is the power spectrum density of the detector noise. The factor 2 comes from considering two Michelson interferometers (6 total laser beams).

As a first approximation, the modulation of the projection onto the detector is estimated by performing an average over the source position and polarization angle. The inclination

[2] A similar behavior but for an *axially symmetric* rotating star (Maclaurin spheroid) has been pointed out in [30]. There, it has been shown that when $n \to 3$, the star can spin up by losing angular momentum (see also [31] for a detailed analysis).

JCAP10(2023)017

of the angular velocity with respect to the line of sight has also been averaged. The Fourier transform of the GW polarizations, $\tilde{h}_+$ and $\tilde{h}_\times$, can be obtained with the stationary phase method [20]. As usual, the characteristic amplitude is:

$$h_c \equiv h_0\sqrt{\frac{dN}{d\ln f}} \overset{\text{opt}}{=} f\sqrt{2(|\tilde{h}_+|^2 + |\tilde{h}_\times|^2)}, \tag{4.2}$$

where the second identity is true *only* when the CEL is optimally oriented. The expected (angle averaged) signal-to-noise ratio is related to the latter characteristic amplitude by

$$\langle\rho^2\rangle = \frac{6}{25}\int_{f_0}^{f_1}\frac{h_c^2}{f^2 S_n(f)}df. \tag{4.3}$$

Since these CEL are quasi-monochromatic, the expected signal-to-noise ratio can be readily estimated with the "reduced" characteristic amplitude, $\tilde{h}_c$, defined as [33]:

$$\tilde{h}_c(f) = h_0(f)\sqrt{N} = h_0(f)\sqrt{fT_{\rm obs}},$$

that applied to eq. (4.3) implies

$$\langle\rho^2\rangle \propto \frac{\tilde{h}_c^2(f_0)}{f_0 S_n(f_0)}. \tag{4.4}$$

Figure 6 shows $\tilde{h}_c$ for a CEL with $n = 2.95$ and $M_{\rm CEL} = 1.0\,{\rm M}_\odot$. Furthermore, in order to illustrate the frequency vs. time evolution of the CEL, we show in the same figure a panel with the time to reach the end of the chirping regime, $\tau_{\rm end} = t_{\rm end} - t$. At $\tau_{\rm end} = 0$ this CEL reaches the GW frequency of $\approx 9.20\,$mHz, after which the GW amplitude decreases.

For a distance between the detector and the source of 1 kpc used in figure 6, $\tilde{h}_c$ is well above the *LISA* noise curve, at least near the end of the chirping regime, so the GW is in principle detectable. The typical value of $\omega/(\pi G\bar{\rho}_0)^{1/2}$ during the chirping phase is $\sim 10^{-5}$–10^{-1}. For typical densities of a white dwarf $\sim 10^6$–$10^9\,{\rm g\,cm^{-3}}$, the frequency is $\sim 10^{-6}$–$10\,$Hz, inside the *LISA* sensitivity band. The detectability properties obtained from eqs. (4.2) and (4.3) are reported in the last column of table 2.

In addition, the CEL can be regarded as monochromatic in some part of their lifetime. Figure 5 shows that the evolution is rather slow at low frequencies, and becomes slower when $n \to 3$. Thus, the CEL is expected to be monochromatic in those regions.

Specifically, whether a GW is monochromatic depends on the detector's frequency resolution or frequency bin, $T_{\rm obs}^{-1}$, on the signal-to-noise ratio, and the frequency evolution of the CEL. The errors in estimating the frequency and its change rate by matched filtering are [36]

$$\Delta f = 0.22\left(\frac{\langle\rho\rangle}{10}\right)^{-1} T_{\rm obs}^{-1}, \tag{4.5}$$

$$\Delta\dot{f} = 0.43\left(\frac{\langle\rho\rangle}{10}\right)^{-1} T_{\rm obs}^{-2}, \tag{4.6}$$

which are frequency independent for $T_{\rm obs} \gtrsim 2\,$yr. The ratio of the error in $\dot{f}$, to the rate of change of the frequency of a CEL can be used to determine its "monochromaticity" [36], i.e.

$$F \equiv \frac{\Delta\dot{f}}{\dot{f}}. \tag{4.7}$$

Thus, a source can be assumed as monochromatic for the detector if $F > 1$. We show this criterion for different polytropic indices in figure 7, from which it is confirmed that in some parts of the sensitivity band, the CELs are monochromatic.

JCAP10(2023)017

$M_{\rm CEL}$ ($\rm M_\odot$)	$\mathcal{C}$ (10^{-4})	$f_{\rm end}^{\rm CEL}$ (mHz)	$M_{\rm chirp}$ ($\rm M_\odot$)	m_1 ($\rm M_\odot$)	m_2 ($\rm M_\odot$)	$f_{\rm end}^{\rm bin}$ (mHz)	Type-like	f_0 (mHz)	$\Delta\phi_{\rm 1y}$	$\frac{\Delta h_0}{h_0}\big\vert_{\rm 1y}$	$\frac{D_{\rm CEL}}{D_{\rm bin}}$	SNR
1.0	2.5	9.20	0.32	1940.62	0.0001	0.053	EMRI	0.05	3.631×10^{-10}	5.937×10^{-13}	0.778	und.
			0.28	0.35	0.30	13.38	PG1101+364	1.0	5.004×10^{-5}	2.515×10^{-9}	0.773	0.687
			0.24	0.45	0.18	7.76	J0106-1003	3.0	5.018×10^{-3}	6.455×10^{-8}	0.835	9.079
1.4	20.0	148.70	0.48	2916.81	0.0015	0.064	EMRI	0.05	5.521×10^{-10}	9.322×10^{-13}	0.808	und.
			0.45	0.59	0.45	19.92	WD0028-474	1.0	3.868×10^{-5}	3.106×10^{-9}	0.776	1.511
			0.43	0.52	0.47	21.30	WD0135-052	3.0	2.660×10^{-3}	6.344×10^{-8}	0.766	23.88
			0.42	0.51	0.45	20.25	WD1204-450	6.0	4.148×10^{-2}	4.377×10^{-7}	0.763	119.89
			0.41	0.47	0.47	21.48	WD1704-481[3]	9.0	2.135×10^{-1}	1.375×10^{-6}	0.764	145.73

Table 2. Parameters of a CEL with $n = 2.95$ and some of its equivalent binaries. The CEL is characterized by the mass and the compactness $\mathcal{C}$ obtained from the relativistic Feynman-Metropolis-Teller equation of state [18]. We calculated the parameters of CEL so that there is a degeneracy with the corresponding binary. We emphasize that the degeneration is potentially subject to the naturalness of the existence of the triaxial object; see discussion below eq. (6.4). The frequency at the end of the chirping phase of the CEL is denoted by $f_{\rm end}^{\rm CEL}$, i.e. when the CEL reaches its maximum GW amplitude. For each CEL, the chirp mass and the mass of the components of the equivalent binary are shown in the fourth, fifth, and sixth columns, respectively. The frequency at the end of the binary chirping regime, $f_{\rm end}^{\rm bin}$, is reported in the seventh column. This value is set, for the case of double white dwarfs, by the point when one of the stars reaches Roche-lobe overflow and, for the case of an EMRI, by the point of tidal disruption, assuming $R_2 \approx 70,000\,\rm km$ for the radius of the less massive component of the EMRI, m_2. The binary type is shown in the eighth column. When the system is a double white dwarf, the name of the most similar observed system is shown. For more details on the double white dwarfs, we refer the reader to [35], and references therein. The initial observing frequency f_0 is shown in the ninth column. The two systems' phase and relative amplitude differences after 1 yr are shown in the next two columns. The ratio of the distance of both systems, assuming optimal orientations, is shown in the twelfth column. The corresponding signal-to-noise ratio of the CEL, located at $D_{\rm CEL} = 1\,\rm kpc$, for an observing time of 1 yr from when $f = f_0$ is shown in the last column.

[3]Same chirp mass.

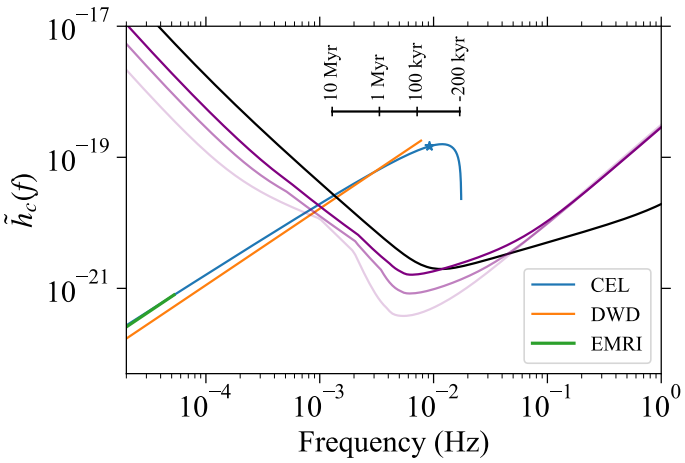

Figure 6. Reduced characteristic amplitude, $\tilde{h}_c$, of a CEL, a double white dwarf, and an EMRI. The CEL has a mass $M_{\rm CEL} = 1.0\,{\rm M}_\odot$ and compactness $\mathcal{C} \approx 2.5 \times 10^{-4}$ (blue), according to the relativistic Feynman-Metropolis-Teller equation of state [18]. The polytropic index is $n = 2.95$ and is located at a distance $D = 1\,{\rm kpc}$. The observing time has been set to $T_{\rm obs} = 2\,{\rm yr}$. The blue dot at $f_{\rm end} \approx 9.20\,{\rm mHz}$ marks the end of the chirping regime of the CEL. The inset shows a chart with the time to reach the end of the chirp, $\tau_{\rm end}$. The EMRI is composed of $m_1 = 1940.62\,{\rm M}_\odot$, $m_2 = 10^{-4}\,{\rm M}_\odot$; it is located at $D = 1.29\,{\rm kpc}$, and its evolution is shown up to the tidal-disruption frequency (green). The double white dwarf is composed of $m_1 = 0.45\,{\rm M}_\odot$, $m_2 = 0.18\,{\rm M}_\odot$; it is located at $D = 1.20\,{\rm kpc}$, and its evolution is shown up to the point of Roche-lobe overflow (orange). For more details, see table 2. Fits of the noise amplitude spectral density of *LISA* are shown as purple continuous lines with decreasing intensity for the configurations N2A1L4, N2A2L4, and N2A5L4, from top to bottom, respectively (see [34] for the explicit form of the fits and conventions meaning). The amplitude spectral density of the *TianQin* project detector is shown as a black continuous curve [2].

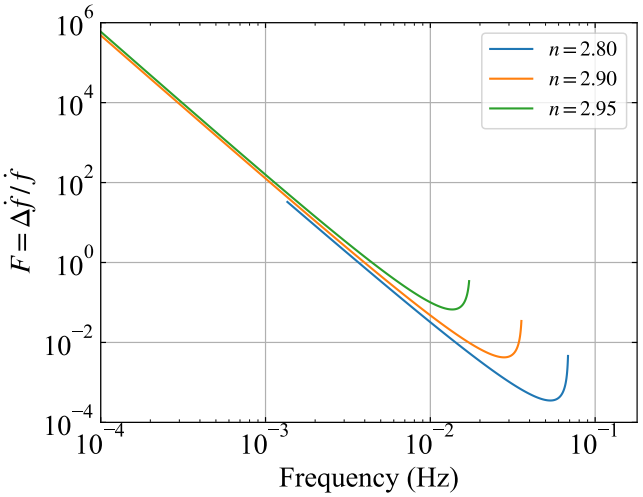

Figure 7. Ratio of $\Delta\dot{f}$, error in estimating the time derivative of the frequency, to the value $\dot{f}$ of CELs with different polytropic indices, $F = \Delta\dot{f}/\dot{f}$. The ratio was obtained assuming $(S/N) = 10$ and $T_{\rm obs} = 2\,{\rm yr}$. When $F > 1$, the error in estimating the frequency is larger than the theoretical value of the CEL, i.e., the time derivative of f is inside the error, and the system can be regarded as monochromatic [36]. For $f \lesssim 3\,{\rm mHz}$, CELs are monochromatic for the adopted detection value.

JCAP10(2023)017

Summarizing, our estimates indicate that CELs are detectable for 1 yr of observation (see table 2), given they have appreciable deformation and are close enough, $D \lesssim 1\,\mathrm{kpc}$. Detectability depends also on the frequency. The system is monochromatic at very low frequencies, $f < 1\,\mathrm{mHz}$. Still, its GW amplitude (at $D = 1\,\mathrm{kpc}$) is not high enough to accumulate sufficient signal-to-noise ratio in 1 yr to be detected (see table 2 and figure 6).

5 CEL-binary degeneracy

We now compare the above results with the ones associated with specific binary systems. In the quasi-circular orbit approximation, the intrinsic phase-time parameter of a binary has a power-law exponent equal to $-5/3$. For a CEL whose equation of state is modeled as an ultra-relativistic degenerate electron gas ($n = 3$), the intrinsic phase has the same exponent as the binary, which confirms our initial hypothesis. Therefore, there exists a binary system, with an appropriate value of the chirp mass, that matches the phase-time evolution of the CEL (see below).

When $\alpha = -5/3$, the dependence on the compactness in eq. (3.5) disappears. It is interesting that this behavior finds a simple physical explanation in a compact star such as a white dwarf: the ultra-relativistic limit for a Newtonian self-gravitating star made of fermions is approached when $\rho \to \infty$, namely when $R \to 0$. In this limit, the star properties become radius-independent when the critical mass is reached.

For each CEL at a given frequency, a binary system with the same intrinsic phase-time evolution parameter Q_ω exists. Hereafter, we illustrate the analysis with a CEL whose polytropic index is close to 3, ie. $n = 2.95$. It can be seen that at $\omega/\sqrt{\pi G \bar{\rho}_0} \sim 10^{-3}$ the chirp mass is $\sim 0.4\,\mathrm{M}_\odot$ and scales with the compactness, $\mathcal{C}_{1.4}^{3/2}$, where $\mathcal{C}_{1.4} \equiv \mathcal{C}/(2 \times 10^{-3})$ (see figure 8).

To give a complete vision of the CEL-binary degeneracy, we show in figure 9 the chirp mass of the equivalent binary as a function of the observed frequency and the mass of the CEL ($n = 2.95$). The mass-radius relation of the non-rotating white dwarf-like object has been obtained for a Chandrasekhar-like equation of state, i.e. the pressure is given by the electron degeneracy pressure while the density is given by the nuclei rest-mass density.[4]

For a given chirp mass, there is a degeneracy in the masses of the binary components, i.e. there exist many combinations of m_1 and m_2 produce CEL equivalent binaries (see figure 10). Here, we focus on two types of equivalent binaries: 1) detached double white dwarfs and 2) EMRIs composed of an intermediate-mass black hole and a planet-like object. It is worth mentioning that the chirp mass of observed detached double white dwarfs, with the currently measured parameters, ranges from 0.23 to $0.61\,\mathrm{M}_\odot$ [35]. For illustration purposes, we calculated some equivalent binaries to a CEL ($n = 2.95$), and show the results in table 2.

In the limit $n \to 3$, the following relation must be satisfied to have identical phase-time evolution:

$$\frac{3}{5} 2^{7/3} \mathcal{A}_3 \left(\frac{3}{4}\right)^{5/6} = \left(\frac{M_{\mathrm{CEL}}}{M_{\mathrm{bin}}}\right)^{5/3} \frac{1}{\nu}. \tag{5.1}$$

The right-hand side of the last expression is of the order of $(M_{\mathrm{CEL}}/M_{\mathrm{bin}})^{5/3}\nu^{-1} \approx 10$ (see table 1). Consequently, when the chirp mass, $M_{\mathrm{chrip}} = M_{\mathrm{bin}}\nu^{3/5}$, and the mass of the CEL are of the same order, both waveforms have the same phase-time evolution. Equation (5.1),

[4] Differences in the white dwarf mass-radius relation for more general equation of state are negligible for the scope of this work (see, e.g., [18]).

JCAP10(2023)017

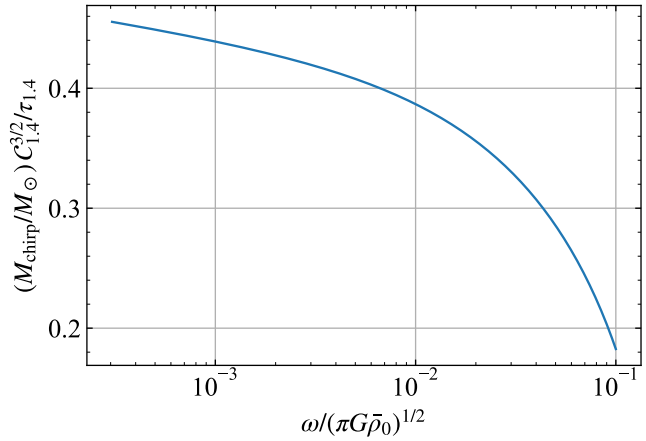

Figure 8. Chirp mass of the binary with the same intrinsic phase-time evolution Q_ω of a CEL of $n = 2.95$, at a GW angular frequency ω. The value has been normalized by $\mathcal{C}_{1.4} \equiv \mathcal{C}/(2 \times 10^{-3})$ and $\tau_{1.4} \equiv (\pi G\bar{\rho}_0/\bar{\rho}_{1.4})^{-1/2}$, where $\bar{\rho}_{1.4}$ is the mean density of a non-rotating white dwarf with mass $1.4\,\mathrm{M}_\odot$ and radius $R_{\rm WD} \approx 1000\,\mathrm{km}$, according to the mass-radius relation obtained from the relativistic Feynman-Metropolis-Teller equation of state [18]. Therefore, the values shown in this plot correspond to a CEL with $M_{\rm CEL} = 1.4\,\mathrm{M}_\odot$, $\mathcal{C} = 2 \times 10^{-3}$.

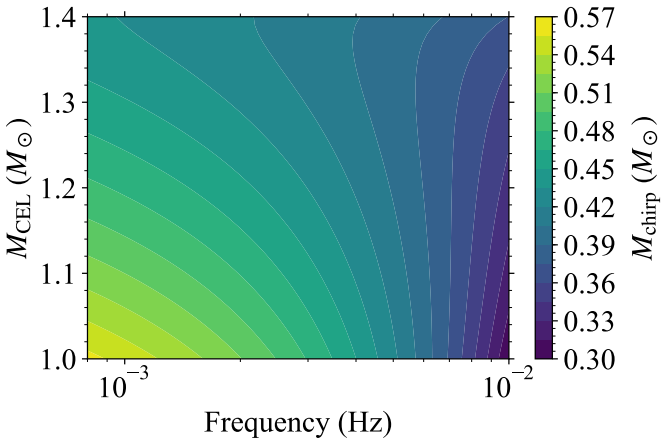

Figure 9. Contours of constant chirp mass of the equivalent binary as a function of the CEL mass and the observed frequency. In general, the chirp mass of the equivalent binary depends on the $\mathcal{C}$, $M_{\rm CEL}$, and the observed frequency f. However, once the equation of state is selected, the mass-radius relation is fixed, implying that $M_{\rm chirp}$ depends only on $M_{\rm CEL}$ and f. We have here used for the white dwarf the "Chandrasekhar" equation of state (see text for details).

can be used to estimate readily the equivalent chirp mass. It is worth mentioning that in the actual calculation, we used the intrinsic phase-time parameter given by the numerical solution of the Riemann S-type sequence and not the one given by the fit.

When the chirp mass has been matched, the two systems have nearly equal phase-time evolution and are, in practice, indistinguishable in their phases. This feature can be appreciated in figure 11, where we compare and contrast the intrinsic phase-time evolution of a CEL and binary systems with matching and non-matching (but close) chirp mass. Some LISA targets that do not match the phase-time evolution of a CEL are an EMRI composed

JCAP10(2023)017

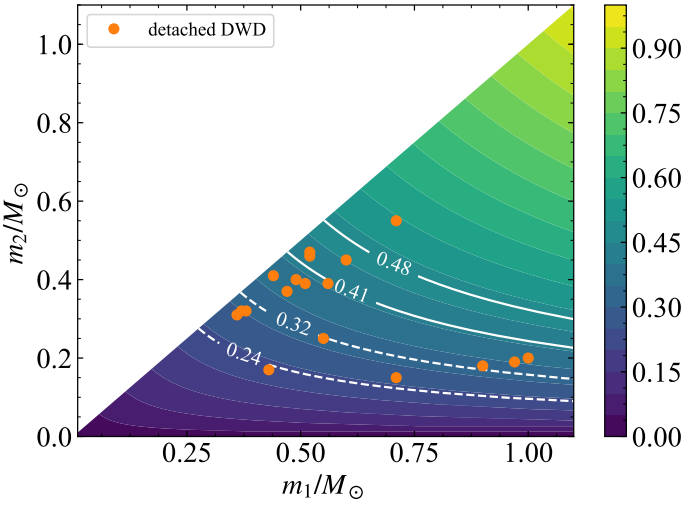

Figure 10. Contours of constant chirp mass of binaries in the mass range of double white dwarfs. Observed detached double white dwarfs with measured parameters [35] are shown as orange circles. The continuous white contour lines correspond a binary with $M_{\rm chirp} = (0.41, 0.48)\,{\rm M}_\odot$, which matches the Q_ω of a CEL with $\mathcal{C} = 2 \times 10^{-3}$, at $f = (9.00, 0.05)\,{\rm mHz}$, respectively. The dashed white contour lines correspond to a binary with $M_{\rm chirp} = (0.24, 0.32)\,{\rm M}_\odot$, which matches the Q_ω of a CEL with $\mathcal{C} = 2.5 \times 10^{-4}$, at $f = (3.00, 0.05)\,{\rm mHz}$, respectively.

of a massive black hole, e.g. $m_1 = 10^5\,{\rm M}_\odot$ and $m_2 = 1\,{\rm M}_\odot$, or a binary neutron star, e.g. $m_1 = m_2 = 1.3\,{\rm M}_\odot$. However, a double white dwarf (also a known LISA target) like J0651, currently the second shortest orbital period known GW emitter in the mHz frequency band [37], has a chirp mass close to the matching one; thus, its phase-time evolution around 1 mHz is nearly equal to the CEL under consideration (see figure 11).

It could be argued that the signal match is not exact for the range of frequencies considered. However, it must be noticed that, since both systems are quasi-monochromatic, differences between the evolution parameters appear when the frequency changes appreciably. They become out of phase only when the observation is performed over very long periods of time $\gg 4\,{\rm yr}$.

We now estimate how much the systems get out of phase by integrating $\Delta Q_\omega = |Q_\omega^{\rm CEL} - Q_\omega^{\rm bin}|$, during 1 yr, i.e.

$$\Delta\phi_{\rm 1y} = \int_{\omega_0}^{\omega_{\rm 1yr}} \Delta Q_\omega d\ln\omega, \tag{5.2}$$

where ω_0 is the initial observed GW angular frequency and $\omega_{\rm 1yr}$ is the GW angular frequency after 1 yr. The results are presented in table 2. As observed, phase differences are extremely small for most of the considered values of $M_{\rm CEL}$ and n. The systems (CEL and binary) are monochromatic at very low frequencies and show full degeneracy.

Regarding the GW amplitude, we found that $h_c \propto f^{-1/5}$ and this holds almost for any n. Therefore, the reference amplitude h_0 scales as $h_0 \propto f^{-1/5-\alpha/2}$.

Although in the limit $n \to 3$ the intrinsic phase-time evolution of the CEL and the binary tend to follow the same power-law exponent, the CEL amplitude $h_0 \propto f^{0.63}$ grows with a different (but nearly equal) exponent. For example, once some chirp mass has matched the phase, the distance to the source can be chosen to match the GW amplitudes. We have found that the distances must be of the same order. Again, since the exponents are nearly

JCAP10(2023)017

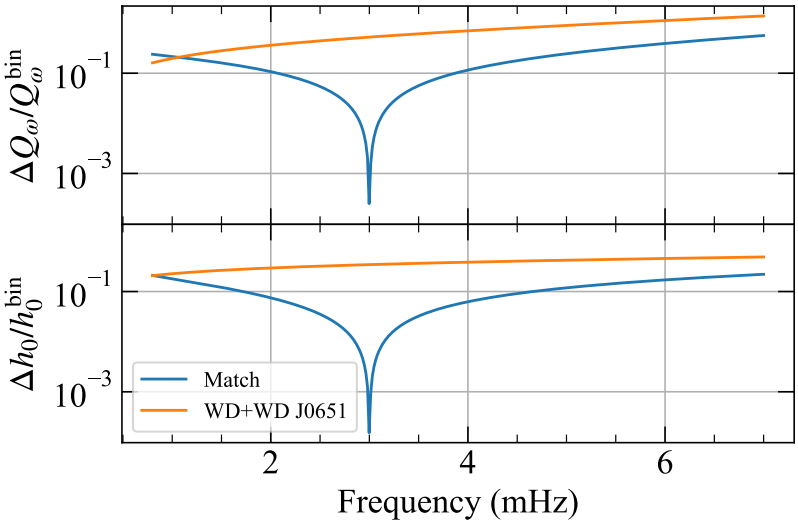

Figure 11. Residuals of comparison of the GW phase (top panel) and amplitude (bottom panel), of a CEL ($n = 2.95$) with $M_{\rm CEL} = 1.0\,{\rm M}_\odot$ and $\mathcal{C} = 2.5 \times 10^{-4}$, and an equivalent binary system with $M_{\rm bin} = 0.24\,{\rm M}_\odot$. The binary matches the Q_ω of the CEL at $f = 3\,{\rm mHz}$ (dip in the residuals). For reference, we also show in orange, the residual of comparing the CEL signal with that of the detached double white dwarf J0651 ($M_{\rm chirp} = 0.31\,{\rm M}_\odot$). The compared binaries are located at the same distance from the detector, while the ratio of the distances to the EMRI and the CEL is $D_{\rm bin}/D_{\rm CEL} = 1.2$.

equal and the evolution during observing time is slow, the GW amplitudes remain nearly equal, as shown in the examples of table 2 and figure 11.

The end of the chirp regime for a binary depends on its nature. For the case of a double white dwarf, this is generally given by the Roche-lobe overflow. Thus, we set this frequency using the Eggleton approximate formula for the effective Robe-lobe radius [38]. The radius of each component has been obtained assuming a polytropic equation of state with $n = 1.5$ [39], since in this case, the matching binary has low-mass components. Roche-lobe overflow frequencies for selected double white dwarfs are reported in table 2. For the case of an EMRI, the limit is due to the tidal disruption of the less massive component. The GW frequency at tidal disruption is:

$$f_{\rm td} \approx (G m_2/R_2^3)^{1/2}/(2.4^{3/2}\pi),$$

where R_2 is the radius of the (less massive) component m_2, and the tidal radius is $r_{\rm td} \approx 2.4 q^{-1/3} R_2$ [9] (see also table 2).

The above detection degeneracy might be broken since the chirping phase of the CEL and the binary, owing to Roche-lobe overflow or tidal disruption, end at different frequencies. It would then be possible to discriminate between systems by observing above some frequency. For instance, if the observation is carried out near and beyond the Roche-lobe overflow frequency, the continuation of a chirping power-law with exponent $\approx -5/3$, will point to a CEL ($n = 2.95$). In contrast, if the power-law changes, this will hint at the possibility that the system is a double white dwarf that just filled one of its Roche-lobes. In addition, degeneracy between an EMRI and a CEL is broken, owing to the fact the former can not be *individually* detected by currently planned space-based detectors (see table 2).

JCAP10(2023)017

Finally, in the low-velocity, weak-field limit, any monochromatic GW can be *considered* as being radiated from a deformed (not axially symmetric) rotating star. Equivalently, any monochromatic GW can be thought as produced from a circular binary. The correspondence between monochromatic GWs and sources is not one-to-one. The appropriate identification of the source (if possible) relies on the astrophysical implications of the characterizing parameters and/or additional astronomical data, such as the relative abundance of the two systems.

In summary, the above results show that given a CEL *with n close to 3*, a binary system can be found whose *GW chirping evolution during observing times* matches the one of the CEL, and vice-versa. When this chirping evolution is not identifiable due to the slow intrinsic evolution, short periods of observation, or both, the system's true nature would be highly uncertain.

As already stated, CELs can be monochromatic. Thus, detection degeneracy extends to even more systems. Namely, in the monochromatic regime, there is a degeneracy between CELs, or between CELs and binaries with parameters different from previously found. This kind of degeneracy will be addressed elsewhere.

6 Rate of equivalent binaries and CEL

Next, to assess the impact of the binary-CEL detection-degeneracy, we estimate the rate of both sources in the local universe for the sensitivity of *LISA* at the frequencies of interest (figure 6). We adopt the source parameters of table 2.

The equivalent EMRIs found for the CEL are formed by an intermediate-mass black hole with a mass in the range $m_1 = 500$–$3000\,\mathrm{M}_\odot$ and a substellar, planet-like object $m_2 \approx \nu m_1 = (0.7\text{–}4)\times 10^{-3}\,\mathrm{M}_\odot$. The latter mass range corresponds approximately to masses between the one of Saturn ($M_{\mathrm{Sat}} = 3\times 10^{-4}\,\mathrm{M}_\odot$) and the one of Jupiter ($M_{\mathrm{Jup}} \sim 10^{-3}\,\mathrm{M}_\odot$). Intermediate-mass black holes in this mass range have been suggested by observations and simulations, at least for the case of dynamically, old globular clusters (see e.g. [40]). It has also been suggested that dwarf spheroidal galaxies may harbor intermediate-mass black holes in their cores (see e.g. [41]). In the latter case, however, the galaxy core may also be explainable as a dark matter concentration alternative to the intermediate-mass black hole [42].

Even if the association of intermediate-mass black holes with planetary-mass objects is absent in the literature, extensive work has been done testing different dynamical processes in the core of young stellar clusters, able (at least numerically) to drive the formation of intermediate mass-ratio binary inspirals (IMRIs). These IMRIs typically include an intermediate-mass black hole and a compact stellar object (stellar-mass black holes, neutron stars, or main sequence stars). These results, at least for our purposes, can shed some light on the odd systems here considered.

We assume that those dynamical mechanisms operate independently of the mass of the captured compact object (obeying the equivalence principle). If this assumption is true, the challenge is whether planetary-sized objects could be found at the core of globular clusters and dwarf spheroidals.

Planetary formation in globular clusters has been a matter of debate for several decades [43–46]. Still, and against all odds, to the date of writing, at least one planet has been discovered in the globular cluster M4. The planet has a similar Jupiter-like mass and orbits a binary system formed by the millisecond pulsar PSR B1620-26 and a white dwarf [47]. More intriguingly, the system is located close to the cluster core, where the dynamical lifetime of

JCAP10(2023)017

planetary systems is much lower than the estimated binary age. This suggests that, at least in this case, the planet originally formed around its host star (the white dwarf's progenitor) while being far from the center. The star and its planet (or its entire planetary system) then migrate towards the center, encountering in the process the pulsar. Once there, the system may become unstable in a timescale of 10^8 yr (see eq. 5 in [47]), and the planet will probably be detached from the system and eventually captured by the intermediate-mass black hole. The details of this process will also depend on the complex dynamics of the cluster [48–50].

Let us assume that a fraction f of the stars in the outer regions of a dynamically evolved globular cluster have planetary companions, and a fraction g of them migrates towards the center in a multi-Gyr timescale. Further, we assume that once there, most systems become unstable, and the intermediate-mass black hole captures planets. Under these conditions, the formation rate of EMRIs at a given globular cluster can be estimated as $10^{-9} f \cdot g \cdot N_\star \, \mathrm{yr}^{-1}$. The number of globular clusters in the local Universe is uncertain, but it can be estimated within the local group (which occupies a volume of $4\,\mathrm{Mpc}^{-3}$). The Milky Way contain around 200 (see e.g. [51] and references there in); Andromeda has the largest number with 460 ± 70 [52]; M33 has only 30 [53]; while the Large Magellanic Cloud has around 13 [54]. Assuming at least 1 globular cluster in the ~ 30 dwarf galaxies of the local group, the total number of globular clusters within 1 Mpc will be $\sim 10^3$. If only a fraction α of them contain an intermediate-mass black hole with a mass as large as that able to mimic the signal of a CEL, namely $10^3\,\mathrm{M}_\odot$, the rate of EMRIs will be $R_{\rm EMRI} = 10^{-6} \alpha \cdot f \cdot g \cdot N_\star \, \mathrm{yr}^{-1}$. Assuming $N_\star \sim 10^6$, $\alpha = 0.2$–1, $f = 0.5$, $g = 0.1$–1, this rate becomes:

$$R_{\rm EMRI} = 0.02 - 0.5 \ \mathrm{yr}^{-1}. \tag{6.1}$$

Another family of the identified equivalent binary systems corresponds to double white dwarfs. Since we are interested in the systems that can enter the interferometer frequency band, we now adopt double white dwarfs that can merge within the Hubble time. The merger rate of these systems in a typical galaxy is estimated to be $(1\text{–}80) \times 10^{-13}\,\mathrm{yr}^{-1}\,\mathrm{M}_\odot^{-1}$ (at 2σ) [55, 56]. Thus, using $M = 6.4 \times 10^{10}\,\mathrm{M}_\odot$ for the Milky Way [57], we obtain:

$$R_{\rm DWD} = 0.0064 - 0.512 \ \mathrm{yr}^{-1}. \tag{6.2}$$

Turning to the CEL, we have seen that their structure (mass, radii, compactness, equation of state, etc.) points to a white dwarf-like nature. Deformed white dwarfs can result from mass transfer from a companion, see e.g. [58]. The rate at which these events occur might be close to that of novae, which has been estimated in the Milky Way to be ~ 10–$80\,\mathrm{yr}^{-1}$ [59] and, more recently, ~ 27–$81\,\mathrm{yr}^{-1}$ [60]. If we assume that a fraction β of all white dwarfs potentially becoming novae undergone a spin-up transition, the CEL rate may be as high as:

$$R_{\rm CEL} = (10 - 80)\beta \ \mathrm{yr}^{-1}. \tag{6.3}$$

Another, possibly more plausible mechanism for the formation of highly-deformed white dwarfs is the merging of double white dwarfs. Numerical simulations show that, when the merger does not lead to a type Ia supernova, the merged configuration is made of three regions [22–26, 61, 62]: a rigidly rotating, central white dwarf, on top of which there is a hot, differentially-rotating, convective corona, surrounded by a Keplerian disk. The corona comprises about half of the mass of the totally disrupted secondary star, while the rest of the secondary mass belongs to the disk since a small mass ($\sim 10^{-3}\,\mathrm{M}_\odot$) is ejected. The rigid core+corona configuration has a structure that resembles our CEL or triaxial object after the

JCAP10(2023)017

chirping regime (see figure 4). Depending on the merging components masses, the central remnant can be a massive (1.0–1.5 $M_\odot$), fast rotating ($P = 1$–10 s) white dwarf [31, 63].

We adopt the view that the deformed white dwarfs result from double white dwarf mergers that do not lead to type Ia supernovae since the latter should lead to total disruption of the merged remnant, see figure 4. We estimate the merger rate as the rate (6.2), subtracted off the type Ia supernova rate that is about (12–22)% of it [64]. Therefore, by requiring the double white dwarf merger channel to cover the supernova Ia population, we obtain a lower limit to the rate of deformed white dwarfs from such mergers, potentially observable as a CEL within the Milky Way. Thus, we obtain:

$$R_{\rm CEL} = \gamma(\epsilon)(0.0056 - 0.45)\ {\rm yr}^{-1} \tag{6.4}$$

Since only eccentric mergers give rise to the final ellipsoidal-shape object, see e.g., [65], $\gamma(\epsilon)$ is a parameter indicating that fraction. Given that not all Riemann-S ellipsoids behave as a CEL, but only those with appreciable deformation (the chirping nature occurs at the beginning of the evolution, see figure 5), γ is a function the ellipticity, $\epsilon \equiv (I_{11} - I_{22})/(I_{11} + I_{22})$. As far as we know, this parameter has not been obtained from simulations or observations. The possible observation of GW radiation from CELs or EM (see, e.g. [66]) could constrain this parameter. On the other hand, this rate can be very similar to the EMRI rate estimated before (see eq. (6.1)). Using an extrapolating factor of Milky Way equivalent galaxies, whose volume is $0.016\,{\rm Mpc}^{-3}$ [57], the above rate implies a local cosmic rate of $(0.74$–$5.94)\times 10^6\,{\rm Gpc}^{-3}\,{\rm yr}^{-1}$.

Therefore, we found that EMRIs, double white dwarfs, and CELs (here identified as deformed white dwarfs) could be numerous. The rates of CELs, as a function of the ellipticity, could be comparable to the ones of EMRIs and double white dwarfs.

Although the above rate of EMRIs is as high as that of the double white dwarf mergers or that of the CEL, they do not represent an important source of degeneracy since the signal-to-noise ratio in one-year time of observation is very low, impeding their detection as *single sources* by GW detectors (see table 2). However, given their very likely high occurrence rate, they might represent an important source of GW stochastic background, which will be studied elsewhere.

Under these conditions, the CEL-double white dwarf potential degeneracy is a significant problem. The unambiguous identification of these sources would need to pinpoint its sky position and/or be able to observe above the frequency of Roche-lobe overflow of the less massive white dwarf in the double white dwarf system (see figure 6 and table 2). Whether or not this would be achievable by the planned space-based facilities GW-detection remains a question to be answered. Still, it can be done via joint electromagnetic observations or future arrays of space-based interferometers.

7 Conclusions

Compressible, Riemann S-type ellipsoids with a polytropic index $n \gtrsim 2.7$, that we have called CELs, emit quasi-monochromatic GWs with a frequency that falls in the sensitivity band of planned space-based detectors (eg. *LISA* and *TianQin*; see figure 1). Inside the sensitivity band, CELs evolve sufficiently slowly to remain quasi-monochromatic during the planned observation times. These sources exhibit a chirp-like behavior similar to binary systems. In the limit $n \to 3$, as inferred from empirical fits shown in table 1, both systems have the same intrinsic phase-time evolution Q_ω. This behavior is due to the change in the compressibility of the CEL with n.

JCAP10(2023)017

CELs located at galactic distances are detectable by planned space-based detectors during one year of observation (see last column of table 2). We refer to CELs as those triaxial objects with *appreciable* deformation, so they exhibit a chirping nature. We have found that within the detectors sensitivity band, a CEL ($2.9 \lesssim n < 3.0$) having intrinsic, quasi-monochromatic parameters, $h_0, f, \dot{f}$, or equivalently h_0, Q_ω can have the same values of those of a binary, see figure 8 and table 2. Namely, given a quasi-monochromatic binary characterized by its frequency, chirp mass, and distance, it can be found a CEL mass and distance, whose waveform at the same frequency has the same $\dot{f}$ (or Q_ω) and amplitude of the binary. In this sense, CEL and quasi-monochromatic binaries could be degenerated, given the naturalness of CELs' existence to be determined. We have here pinpointed two kinds of quasi-monochromatic binaries potentially degenerated with CELs: double white dwarfs and EMRIs composed of an intermediate-mass black hole and a planet-like object.

The completely different physical nature of CELs and such binaries should allow, in principle, to distinguish them. Following this reasoning, we have found that the final frequency of the quasi-monochromatic chirping behavior of a binary is set, in the case of EMRIs (intermediate-mass black hole-planet), by the tidal disruption, or in the case of a double white dwarf, by Roche-lobe overflow. The tidal disruption frequency of this system is $\sim 10^{-5}\,\mathrm{Hz}$. These EMRIs cannot be detected as single sources by space-based detectors since they do not accumulate enough signal-to-noise ratio in the observing time (see table 2). Thus, CELs and EMRIs do not pose the problem of detection degeneracy. For the systems considered in this work, the following relation is in general satisfied: $f_{\mathrm{td}} < f_{\mathrm{RLOF}} < f_{\mathrm{end}}^{\mathrm{CEL}}$. Consequently, observing a quasi-monochromatic GW (with chirp mass $\sim 0.5\,\mathrm{M}_\odot$) above the Roche-lobe overflow frequency would strongly indicate a CEL. Below frequencies $\sim 10^{-2}\,\mathrm{Hz}$, the CELs and binaries are degenerated and cannot be distinguished using only GW data. In those cases, the electromagnetic data will be crucial in determining the real nature of the GW source.

Because of the relevance of this result for space-based detectors, we have discussed the current estimates of the occurrence rate of this kind of system. For the deformed white dwarfs, we adopted the view that they can be formed either by accretion from a companion or by double white dwarf mergers (see figure 4). Surprisingly, we found that rates of EMRIs, double white dwarf, and CELs could be comparable (see the discussion below eq. (6.4)). Although EMRIs cannot be individually resolved, their occurrence rate makes them a plausible stochastic GW source that deserves a detailed analysis. However, this issue is beyond the scope of the present article and will be addressed elsewhere. From the present first approach, we can conclude that there might be a potential GW source *confusion*, for individually resolved events in the frequency range $f \lesssim 10\,\mathrm{mHz}$, between double white dwarfs and CELs. Despite this issue, it is possible to do science with these sources. Indeed, we have presented some possible solutions for the detection-degeneracy problem and encourage the scientific community to explore additional ones.

Acknowledgments

JMBL thanks support from the FPU fellowship by Ministerio de Educación Cultura y Deporte from Spain. J.F.R. thanks financial support from the Patrimonio Autónomo — Fondo Nacional de Financiamiento para la Ciencia, la Tecnología y la Innovación Francisco José de Caldas (MINCIENCIAS — COLOMBIA) under the grant No. 110685269447 RC-80740-465-2020, project 69553, and from the Universidad Industrial de Santander, VIE, Contrato de financiamiento RC No. 003-1598/Registro Contractual 2023000357.

JCAP10(2023)017

References

[1] LISA collaboration, *Laser Interferometer Space Antenna*, arXiv:1702.00786 [INSPIRE].

[2] TianQin collaboration, *TianQin: a space-borne gravitational wave detector*, *Class. Quant. Grav.* **33** (2016) 035010 [arXiv:1512.02076] [INSPIRE].

[3] W.-R. Hu and Y.-L. Wu, *The Taiji Program in Space for gravitational wave physics and the nature of gravity*, *Natl. Sci. Rev.* **4** (2017) 685 [INSPIRE].

[4] L. Barack and C. Cutler, *LISA capture sources: Approximate waveforms, signal-to-noise ratios, and parameter estimation accuracy*, *Phys. Rev. D* **69** (2004) 082005 [gr-qc/0310125] [INSPIRE].

[5] P. Amaro-Seoane et al., *Low-frequency gravitational-wave science with eLISA/NGO*, *Class. Quant. Grav.* **29** (2012) 124016 [arXiv:1202.0839] [INSPIRE].

[6] S. Babak et al., *Science with the space-based interferometer LISA. V: Extreme mass-ratio inspirals*, *Phys. Rev. D* **95** (2017) 103012 [arXiv:1703.09722] [INSPIRE].

[7] LIGO Scientific and Virgo collaborations, *Full Band All-sky Search for Periodic Gravitational Waves in the O1 LIGO Data*, *Phys. Rev. D* **97** (2018) 102003 [arXiv:1802.05241] [INSPIRE].

[8] LIGO Scientific and Virgo collaborations, *First search for gravitational waves from known pulsars with Advanced LIGO*, *Astrophys. J.* **839** (2017) 12 [arXiv:1701.07709] [*Erratum ibid.* **851** (2017) 71] [INSPIRE].

[9] S. Chandrasekhar, *Ellipsoidal Figures of Equilibrium*, Dover Publications, New Haven, U.S.A. (1963).

[10] A. Ferrari and R. Ruffini, *Theoretical Implications of the Second Time Derivative of the Period of the Pulsar NP 0532*, *Astrophys. J. Lett.* **158** (1969) L71.

[11] S. Chandrasekhar, *The Effect of Gravitational Radiation on the Secular Stability of the Maclaurin Spheroid*, *Astrophys. J.* **161** (1970) 561.

[12] S. Chandrasekhar, *The Evolution of the Jacobi Ellipsoid by Gravitational Radiation*, *Astrophys. J.* **161** (1970) 571.

[13] B.D. Miller, *The Effect of Gravitational Radiation-Reaction on the Evolution of the Riemann S-Type Ellipsoids*, *Astrophys. J.* **187** (1974) 609.

[14] D. Lai, F.A. Rasio and S.L. Shapiro, *Ellipsoidal figures of equilibrium - Compressible models*, *Astrophys. J. Suppl.* **88** (1993) 205 [INSPIRE].

[15] D. Lai and S.L. Shapiro, *Gravitational radiation from rapidly rotating nascent neutron stars*, *Astrophys. J.* **442** (1995) 259 [astro-ph/9408053] [INSPIRE].

[16] LIGO Scientific and Virgo collaborations, *Search for Post-merger Gravitational Waves from the Remnant of the Binary Neutron Star Merger GW170817*, *Astrophys. J. Lett.* **851** (2017) L16 [arXiv:1710.09320] [INSPIRE].

[17] D. Lai, F.A. Rasio and S.L. Shapiro, *Hydrodynamic instability and coalescence of binary neutron stars*, *Astrophys. J.* **420** (1994) 811 [astro-ph/9304027] [INSPIRE].

[18] M. Rotondo, J.A. Rueda, R. Ruffini and S.-S. Xue, *The Relativistic Feynman-Metropolis-Teller theory for white dwarfs in general relativity*, *Phys. Rev. D* **84** (2011) 084007 [arXiv:1012.0154] [INSPIRE].

[19] L.D. Landau and E.M. Lifshitz, *The classical theory of fields*, Pergamon Press, Oxford, U.K. (1975).

[20] M. Maggiore, *Gravitational Waves. Volume 1: Theory and Experiments*, Oxford University Press, Oxford, U.K. (2008).

JCAP10(2023)017

[21] C.W. Misner, K.S. Thorne and J.A. Wheeler, *Gravitation*, Princeton University Press, Princeton, U.S.A. (2017).

[22] W. Benz, A.G.W. Cameron, W.H. Press and R.L. Bowers, *Dynamic Mass Exchange in Doubly Degenerate Binaries. I. 0.9 and 1.2 M_{sun} Stars*, *Astrophys. J.* **348** (1990) 647.

[23] P. Lorén-Aguilar, J. Isern and E. García-Berro, *High-resolution smoothed particle hydrodynamics simulations of the merger of binary white dwarfs*, *Astron. Astrophys.* **500** (2009) 1193.

[24] C. Raskin, E. Scannapieco, C. Fryer, G. Rockefeller and F.X. Timmes, *Remnants of Binary White Dwarf Mergers*, *Astrophys. J.* **746** (2012) 62 [arXiv:1112.1420] [INSPIRE].

[25] C. Zhu, P. Chang, M. van Kerkwijk and J. Wadsley, *A Parameter-Space Study of Carbon-Oxygen White Dwarf Mergers*, *Astrophys. J.* **767** (2013) 164 [arXiv:1210.3616] [INSPIRE].

[26] M. Dan, S. Rosswog, M. Brüggen and P. Podsiadlowski, *The structure and fate of white dwarf merger remnants*, *Mon. Not. Roy. Astron. Soc.* **438** (2014) 14 [arXiv:1308.1667] [INSPIRE].

[27] D.J. Price et al., *PHANTOM: A Smoothed Particle Hydrodynamics and Magnetohydrodynamics Code for Astrophysics*, *Publ. Astron. Soc. Austral.* **35** (2018) 31 [arXiv:1702.03930] [INSPIRE].

[28] D.J. Price, *SPLASH: An interactive visualisation tool for Smoothed Particle Hydrodynamics simulations*, *Publ. Astron. Soc. Austral.* **24** (2007) 159 [arXiv:0709.0832] [INSPIRE].

[29] T. Damour, A. Nagar and S. Bernuzzi, *Improved effective-one-body description of coalescing nonspinning black-hole binaries and its numerical-relativity completion*, *Phys. Rev. D* **87** (2013) 084035 [arXiv:1212.4357] [INSPIRE].

[30] S.L. Shapiro, S.A. Teukolsky and T. Nakamura, *Spin-up of a Rapidly Rotating Star by Angular Momentum Loss*, *Astrophys. J.* **357** (1990) L17.

[31] L. Becerra, J.A. Rueda, P. Loren-Aguilar and E. Garcia-Berro, *The Spin Evolution of Fast-Rotating, Magnetized Super-Chandrasekhar White Dwarfs in the Aftermath of White Dwarf Mergers*, *Astrophys. J.* **857** (2018) 134 [arXiv:1804.01275] [INSPIRE].

[32] L.S. Finn, *Detection, measurement and gravitational radiation*, *Phys. Rev. D* **46** (1992) 5236 [gr-qc/9209010] [INSPIRE].

[33] É.É. Flanagan and S.A. Hughes, *Measuring gravitational waves from binary black hole coalescences: 1. Signal-to-noise for inspiral, merger, and ringdown*, *Phys. Rev. D* **57** (1998) 4535 [gr-qc/9701039] [INSPIRE].

[34] A. Klein et al., *Science with the space-based interferometer eLISA: Supermassive black hole binaries*, *Phys. Rev. D* **93** (2016) 024003 [arXiv:1511.05581] [INSPIRE].

[35] A. Rebassa-Mansergas et al., *Orbital periods and component masses of three double white dwarfs*, *Mon. Not. Roy. Astron. Soc.* **466** (2017) 1575 [arXiv:1612.00217].

[36] R. Takahashi and N. Seto, *Parameter estimation for galactic binaries by LISA*, *Astrophys. J.* **575** (2002) 1030 [astro-ph/0204487] [INSPIRE].

[37] J.J. Hermes et al., *Rapid Orbital Decay in the 12.75-minute WD+WD Binary J0651+2844*, *Astrophys. J. Lett.* **757** (2012) L21 [arXiv:1208.5051] [INSPIRE].

[38] P.P. Eggleton, *Approximations to the radii of Roche lobes*, *Astrophys. J.* **268** (1983) 368 [INSPIRE].

[39] S. Chandrasekhar, *An introduction to the study of stellar structure*, Dover, New York, U.S.A. (1967).

[40] I. Mandel, D.A. Brown, J.R. Gair and M.C. Miller, *Rates and Characteristics of Intermediate-Mass-Ratio Inspirals Detectable by Advanced LIGO*, *Astrophys. J.* **681** (2008) 1431 [arXiv:0705.0285] [INSPIRE].

JCAP10(2023)017

[41] P.B. Graff, A. Buonanno and B.S. Sathyaprakash, *Missing Link: Bayesian detection and measurement of intermediate-mass black-hole binaries*, *Phys. Rev. D* **92** (2015) 022002 [arXiv:1504.04766] [INSPIRE].

[42] C.R. Argüelles, A. Krut, J.A. Rueda and R. Ruffini, *Novel constraints on fermionic dark matter from galactic observables II: Galaxy scaling relations*, *Phys. Dark Univ.* **24** (2019) 100278 [arXiv:1810.00405] [INSPIRE].

[43] S. Sigurdsson, *Planets in globular clusters?*, *Astrophys. J. Lett.* **399** (1992) L95.

[44] M.B. Davies and S. Sigurdsson, *Planets in 47 tuc*, *Mon. Not. Roy. Astron. Soc.* **324** (2001) 612 [astro-ph/0104336] [INSPIRE].

[45] M.E. Beer, A.R. King and J.E. Pringle, *The Planet in M4: Implications for planet formation in globular clusters*, *Mon. Not. Roy. Astron. Soc.* **355** (2004) 1244 [astro-ph/0409762] [INSPIRE].

[46] N. Soker and A. Hershenhorn, *Expected Planets in Globular Clusters*, *Mon. Not. Roy. Astron. Soc.* **381** (2007) 334 [arXiv:0704.1067] [INSPIRE].

[47] E.B. Ford, K.J. Joshi, F.A. Rasio and B. Zbarsky, *Theoretical implications of the psr b1620-26 triple system and its planet*, *Astrophys. J.* **528** (2000) 336 [astro-ph/9905347] [INSPIRE].

[48] G. Meylan and D.C. Heggie, *Internal dynamics of globular clusters*, *Astron. Astrophys. Rev.* **8** (1997) 1 [astro-ph/9610076] [INSPIRE].

[49] H. Baumgardt, J. Makino, P. Hut, S. McMillan and S.F. Portegies Zwart, *A dynamical model for the globular cluster g1*, *Astrophys. J. Lett.* **589** (2003) L25 [astro-ph/0301469] [INSPIRE].

[50] J.M. Fregeau, M.A. Gurkan, K.J. Joshi and F.A. Rasio, *Monte Carlo simulations of globular cluster evolution. 3. Primordial binary interactions*, *Astrophys. J.* **593** (2003) 772 [astro-ph/0301521] [INSPIRE].

[51] D. Camargo, *Five New Globular Clusters Discovered in the Galactic Bulge*, *Astrophys. J. Lett.* **860** (2018) L27.

[52] P. Barmby and J.P. Huchra, *M31 globular clusters in the hst archive: I. cluster detection and completeness*, *Astron. J.* **122** (2001) 2458 [astro-ph/0107401] [INSPIRE].

[53] W.E. Harris, *Globular cluster systems in galaxies beyond the local group*, *Ann. Rev. Astron. Astrophys.* **29** (1991) 543 [INSPIRE].

[54] S. van den Bergh, *Were the LMC globular clusters formed in a disk?*, *Astron. J.* **127** (2004) 897 [astro-ph/0311322] [INSPIRE].

[55] D. Maoz and N. Hallakoun, *The binary fraction, separation distribution and merger rate of white dwarfs from SPY*, *Mon. Not. Roy. Astron. Soc.* **467** (2017) 1414 [arXiv:1609.02156] [INSPIRE].

[56] D. Maoz, N. Hallakoun and C. Badenes, *The separation distribution and merger rate of double white dwarfs: improved constraints*, *Mon. Not. Roy. Astron. Soc.* **476** (2018) 2584 [arXiv:1801.04275] [INSPIRE].

[57] V. Kalogera, R. Narayan, D.N. Spergel and J.H. Taylor, *The Coalescence rate of double neutron star systems*, *Astrophys. J.* **556** (2001) 340 [astro-ph/0012038] [INSPIRE].

[58] P. Loren-Aguilar, J. Isern and E. Garcia-Berro, *Smoothed Particle Hydrodynamics simulations of white dwarf collisions and close encounters*, *Mon. Not. Roy. Astron. Soc.* **406** (2010) 2749 [arXiv:1004.4783] [INSPIRE].

[59] H.-L. Chen, T.E. Woods, L.R. Yungelson, M. Gilfanov and Z. Han, *Modelling nova populations in galaxies*, *Mon. Not. Roy. Astron. Soc.* **458** (2016) 2916 [arXiv:1602.07849] [INSPIRE].

[60] A.W. Shafter, *The Galactic Nova Rate Revisited*, *Astrophys. J.* **834** (2017) 196 [arXiv:1606.02358].

JCAP10(2023)017

[61] J. Guerrero, E. García-Berro and J. Isern, *Smoothed Particle Hydrodynamics simulations of merging white dwarfs*, *Astron. Astrophys.* **413** (2004) 257.

[62] R. Longland, P. Lorén-Aguilar, J. José, E. García-Berro and L.G. Althaus, *Lithium production in the merging of white dwarf stars*, *Astron. Astrophys.* **542** (2012) A117 [arXiv:1205.2538] [INSPIRE].

[63] J.A. Rueda et al., *A white dwarf merger as progenitor of the anomalous X-ray pulsar 4U 0142+61?*, *Astrophys. J. Lett.* **772** (2013) L24 [arXiv:1306.5936] [INSPIRE].

[64] A.J. Ruiter, K. Belczynski and C.L. Fryer, *Rates and Delay Times of Type Ia Supernovae*, *Astrophys. J.* **699** (2009) 2026 [arXiv:0904.3108] [INSPIRE].

[65] G. Aznar-Siguán, E. García-Berro, P. Lorén-Aguilar, N. Soker and A. Kashi, *Smoothed Particle Hydrodynamics simulations of the core-degenerate scenario for Type Ia supernovae*, *Mon. Not. Roy. Astron. Soc.* **450** (2015) 2948 [arXiv:1503.02444] [INSPIRE].

[66] M.F. Sousa, J.G. Coelho, J.C.N. de Araujo, S.O. Kepler and J.A. Rueda, *The Double White Dwarf Merger Progenitors of SDSS J2211+1136 and ZTF J1901+1458*, *Astrophys. J.* **941** (2022) 28 [arXiv:2208.09506] [INSPIRE].

JCAP10(2023)017

Eur. Phys. J. C (2023) 83:960
https://doi.org/10.1140/epjc/s10052-023-12153-y

THE EUROPEAN PHYSICAL JOURNAL C

Regular Article - Theoretical Physics

Extracting the energy and angular momentum of a Kerr black hole

J. A. Rueda[1,2,3,4,5,a], **R. Ruffini**[1,2,6,b]

[1] ICRANet, Piazza della Repubblica 10, 65122 Pescara, Italy
[2] ICRA, Dipartimento di Fisica, Sapienza Università di Roma, P.le Aldo Moro 5, 00185 Rome, Italy
[3] ICRANet-Ferrara, Dipartimento di Fisica e Scienze della Terra, Università degli Studi di Ferrara, Via Saragat 1, 44122 Ferrara, Italy
[4] Dipartimento di Fisica e Scienze della Terra, Università degli Studi di Ferrara, Via Saragat 1, 44122 Ferrara, Italy
[5] INAF, Istituto de Astrofisica e Planetologia Spaziali, Via Fosso del Cavaliere 100, 00133 Rome, Italy
[6] INAF, Viale del Parco Mellini 84, 00136 Rome, Italy

Received: 4 September 2023 / Accepted: 14 October 2023

Abstract It has been thought for decades that rotating black holes (BHs) power the energetic gamma-ray bursts (GRBs) and active galactic nuclei (AGNs), but the mechanism that extracts the BH energy has remained elusive. We here show that the solution to this problem arises when the BH is immersed in an external magnetic field and ionized low-density matter. For a magnetic field parallel to the BH spin, the induced electric field accelerates electrons outward and protons inward in a conical region, centered on the BH rotation axis, and of semi-aperture angle $\theta \approx 60°$ from the BH rotation axis. For an antiparallel magnetic field, protons and electrons exchange their roles. The particles that are accelerated outward radiate off energy and angular momentum to infinity. The BH powers the process by reducing its energy and angular momentum by capturing polar protons and equatorial electrons with net negative energy and angular momentum. The electric potential allows for negative energy states outside the BH ergosphere, so the latter does not play any role in this electrodynamical BH energy extraction process.

1 Introduction

In this article, we show an electrodynamical process that efficiently extracts the rotational energy of BHs. The mechanism works for stellar-mass BHs in strong magnetic fields that power GRBs and supermassive BHs in weak magnetic fields that power AGNs. A critical ingredient for this discussion is one of the most relevant concepts of BHs, the Christodoulou-Ruffini-Hawking mass-energy formula [1–3]. In its most general form, for a charged, rotating BH, it reads[1]

$$M^2 = \left(M_{\rm irr} + \frac{Q^2}{4M_{\rm irr}}\right)^2 + \frac{J^2}{4M_{\rm irr}^2}, \tag{1}$$

which relates the BH mass-energy, M, to three independent pieces, the *irreducible* mass, $M_{\rm irr}$, the charge, Q, and the angular momentum, J. The radius of the BH horizon is $r_H = M + \sqrt{M^2 - a^2 - Q^2}$, being $a = J/M$, the angular momentum per unit mass. Equation (1) implies a great corollary: part of the BH energy is extractable, i.e., $E_{\rm ext} = M - M_{\rm irr} \geq 0$, and it amounts up to 50% of the mass-energy of a non-rotating, charged BH (in the extreme case $Q = M$), and up to 29% in a neutral, rotating BH (in the extreme case $a = M$). It is worth noticing that the above percentages are obtained under the nontrivial assumption that the BH irreducible mass remains constant during the energy extraction process. For fifty years as of this writing, the concept of BHs being energy storehouses usable by nature has permeated relativistic astrophysics at the theoretical and experimental levels.

To explain the most powerful transients in the Universe, GRBs, stellar-mass (i.e., of a few $M_\odot$) BHs should release up to a few 10^{54} erg in a few seconds. The supermassive BHs (of up to $10^9 M_\odot$), to power AGNs, release luminosities of up to 10^{46} erg s^{-1} for billion years. Existing models of AGNs attempt to explain the emission with massive jets powered by an accretion disk around the BH, and most GRB models have inherited the same idea (see, e.g., [4,5], and references therein). Accretion disk models use gravitational energy, whose low efficiency makes it costly to power the most energetic processes in these relativistic sources.

[a] e-mail: jorge.rueda@icra.it (corresponding author)
[b] e-mail: ruffini@icra.it

[1] We use geometric units $c = G = 1$ unless otherwise specified.

Published online: 24 October 2023

The binary-driven hypernova (BdHN) model of GRBs has proposed as *inner engine* of the high-energy emission in the gigaelectronvolt (GeV) domain, a Kerr BH surrounded by low-density matter and a magnetic field, modeled by the Wald solution [6–8]. For an aligned and parallel (to the BH spin axis) magnetic field, the induced electric field in the polar region accelerates electrons outwardly, reaching ultrarelativistic energies and emitting synchrotron and high-energy curvature radiation. In [7,9], the model has been applied with $M = 4.4M_\odot$, $a/M = 0.4$, and $B_0 = 4 \times 10^{10}$ G to the energetic GRB 190114C, and extended to AGNs, e.g., for the supermassive BH in M87*, with $M = 6 \times 10^9 M_\odot$, $a/M = 0.1$, and $B_0 = 10$ G. These works have focused on the emission of escaping particles assuming by energy conservation that the Kerr BH pays for the energy radiated to infinity. On this basis, the evolution of the BH mass, angular momentum, and irreducible mass as the system radiates have been determined (see, e.g., [7,10]). However, the mechanism for which the BH loses energy and angular momentum has remained unexplained.

Thus, extracting the BH energy is tantalizing and crucial in relativistic astrophysics. The first mechanism of BH energy extraction was the mechanical Penrose process [11]. A particle of energy E_1 splits into two particles of energy E_2 and E_3 that, by energy conservation, fulfill $E_3 = E_1 - E_2$. So, $E_3 > E_1$ if $E_2 < 0$, and the BH reduces its mass by $\delta M = E_2 < 0$ and angular momentum by $\delta J = L_2 < 0$ by absorbing such a particle. The split must occur in the BH *ergosphere*, where negative energy (and associated negative angular momentum) states exist. We shall see that the ergosphere does not play any role in the electrodynamical mechanism presented here.

It was soon demonstrated that the Penrose process is either unrealizable or inefficient (see, e.g., [12–14]). Thus, numerous works have searched for alternatives. For example, from the mechanical viewpoint, the *collisional* Penrose process has received much attention (see, e.g., [15–18]). Generalizations of the Penrose process, i.e., the same three-body problem, accounting for electromagnetic fields, can be found, e.g., in [19–21], and references therein. In parallel, increasing research has been devoted to electromagnetic fields to extract the BH energy. The idea of matter-dominated plasma accreting onto a Kerr BH by Ruffini and Wilson [22], further developed in the Blandford-Znajek mechanism [23], which proposes that poloidal and toroidal magnetic field lines threading the BH extract its rotational energy. Without entering into the discussion of whether or not such a mechanism can operate in accreting rotating BHs, its efficiency, and power should be at most (although unlikely) that of the surrounding accretion disk [24,25]. Numerical, relativistic magnetohydrodynamics and particle-in-cell simulations have also studied the problem (e.g., [26–28]). In the above literature, it is assumed (or achieved under specific conditions) that the density of charged particles in the magnetosphere is high enough to shorten any electric field so that *force-free* electrodynamics applies. Those magnetospheres fulfill magnetic dominance, i.e., $B^2 - E^2 > 0$, and lack accelerating electric fields, i.e., $\mathbf{E} \cdot \mathbf{B} = 0$ everywhere. Those systems can not accelerate charged particles and emit radiation. To alleviate this drawback, it has been borrowed from pulsar theory the concept of *gaps* [29,30], limited regions in the magnetosphere where the force-free condition is violated, leading to regions where $\mathbf{E} \cdot \mathbf{B} \neq 0$ (e.g., [23,26]).

Most numerical simulations of BH magnetospheres use as initial condition the Wald solution of the Einstein-Maxwell equations [31], which describes a Kerr BH immersed in a test magnetic field, asymptotically uniform and aligned (parallel or antiparallel) to the BH spin. The Wald solution contains large regions where $\mathbf{E} \cdot \mathbf{B} \neq 0$ (see next section below). The force-free condition is achieved if the charge density in the magnetosphere exceeds the Goldreich–Julian value [32], $n_{\rm GJ} = \Omega B_0/(2\pi c\, e)$, where Ω is the angular velocity of the corotating magnetic field lines. Since the BH angular velocity is $\Omega_H = a/(2\, M r_H)$, for $M = 4M_\odot$, $a/M = 1$, $B_0 = 10^{13}$ G, we obtain $\rho_{\rm GJ} = m_p n_{\rm GJ} \approx 5 \times 10^{-9}$ g cm^{-3}. Although it looks like a very small value easy to exceed, numerical simulations show that, e.g., the matter density around the BH formed from the gravitational collapse of a neutron star in a BdHN can be as low as $\rho \sim 10^{-14}$ g cm^{-3} [33,34], and the matter to electromagnetic energy density ratio as low as $8\pi\rho/B_0^2 \sim 10^{-10}$. These physical conditions are far from the ones explored in numerical simulations of screening plasma leading to force-free conditions starting from the Wald solution (see, e.g., [27,28], in which both quantities have much higher values).

Bearing the above in mind, we hold on to the Wald solution and show a process that occurs in its electromagnetic field configuration, where $\mathbf{E} \cdot \mathbf{B} \neq 0$, allowing the Kerr BH rotational energy extraction. This overcomes the original difficulty brought by the condition $\mathbf{E} \cdot \mathbf{B} = 0$ in Ruffini and Wilson [22] and Blandford and Znajek [23] treatments.

2 The electromagnetic field

In spheroidal Boyer–Lindquist coordinates (t, r, θ, ϕ), the Kerr BH metric reads [35][2]

$$ds^2 = -\left(1 - \frac{2Mr}{\Sigma}\right) dt^2 + \frac{\Sigma}{\Delta} dr^2 + \Sigma\, d\theta^2 + \frac{A}{\Sigma} \sin^2\theta\, d\phi^2 - \frac{4aMr}{\Sigma} \sin^2\theta\, dt\, d\phi, \tag{2}$$

[2] We use geometric units $c = G = 1$ unless otherwise specified.

where $\Sigma = r^2 + a^2\cos^2\theta$, $\Delta = r^2 - 2Mr + a^2$, $A = (r^2+a^2)^2 - \Delta a^2\sin^2\theta$, being M and $a = J/M$, respectively, the BH mass and angular momentum per unit mass.

The electromagnetic four-potential of the Wald solution for an uncharged, rotating BH is given by [31]

$$A_\mu = \frac{B_0}{2}\,\psi_\mu + a\,B_0\,\eta_\mu, \tag{3}$$

where B_0 is the asymptotic magnetic field strength, and $\eta^\mu = \delta^\mu_t$ and $\psi^\mu = \delta^\mu_\phi$ are the time-like and space-like Killing vectors of the Kerr metric. In the frame of the *locally non-rotating* (LNR) observer [13,36], which carries a tetrad basis with vectors $\vec{e}_{\hat{a}}$, the electric and magnetic field components are given by

$$E_{\hat{i}} = E_\mu\,\vec{e}^{\,\mu}_{\hat{i}} = F_{\hat{i}\hat{t}}, \qquad B_{\hat{i}} = B_\mu\,\vec{e}^{\,\mu}_{\hat{i}} = (1/2)\epsilon_{\hat{i}\hat{j}\hat{k}}F^{\hat{j}\hat{k}}, \tag{4}$$

where $F_{\mu\nu}$ is the electromagnetic field tensor in the coordinate basis. Careted components are in the LNR frame, Greek indexes run from 0 to 3 (t, r, θ, and ϕ), and Latin indexes run from 1 to 3. In Boyer–Lindquist coordinates, the components $E_{\hat{i}}$ and $B_{\hat{i}}$ are given in Eqs. (16a)–(16d) in [37] for the chargeless case ($Q = 0$) and can be written as

$$E_{\hat{r}} = -\frac{B_0 aM}{\Sigma^2 A^{1/2}}\Big[(r^2+a^2)(r^2 - a^2\cos^2\theta)(1+\cos^2\theta) - 2r^2\sin^2\theta\,\Sigma\Big], \tag{5a}$$

$$E_{\hat{\theta}} = B_0 aM\,\frac{\Delta^{1/2}}{\Sigma^2 A^{1/2}}2ra^2\sin\theta\cos\theta(1+\cos^2\theta), \tag{5b}$$

$$B_{\hat{r}} = -\frac{B_0\cos\theta}{\Sigma^2 A^{1/2}}\Big\{2Mra^2[2r^2\cos^2\theta + a^2(1+\cos^4\theta)] - (r^2+a^2)\Sigma^2\Big\}, \tag{6a}$$

$$B_{\hat{\theta}} = -\frac{\Delta^{1/2}B_0\sin\theta}{\Sigma^2 A^{1/2}}[Ma^2(r^2 - a^2\cos^2\theta)(1+\cos^2\theta) + r\Sigma^2]. \tag{6b}$$

We can now calculate the regions of charged particles' acceleration. For the present case of magnetic dominance, i.e., $B^2 > E^2$ [37], charged particles move along magnetic field lines. For magnetic field lines that cross the horizon, a particle will either move inward to the BH or be expelled outward, depending upon its charge. The electric field component parallel to the magnetic field line accelerates the particle. Therefore, we calculate the scalar product $\vec{E}\cdot\vec{B}$ on the BH horizon, $(\vec{E}\cdot\vec{B})_H$. Specifically, we are interested in the regions where $(\vec{E}\cdot\vec{B})_H$ is positive and negative, so we calculate the regions where it vanishes, which separate the regions of acceleration. At the event horizon, we have $\Delta = 0$, which

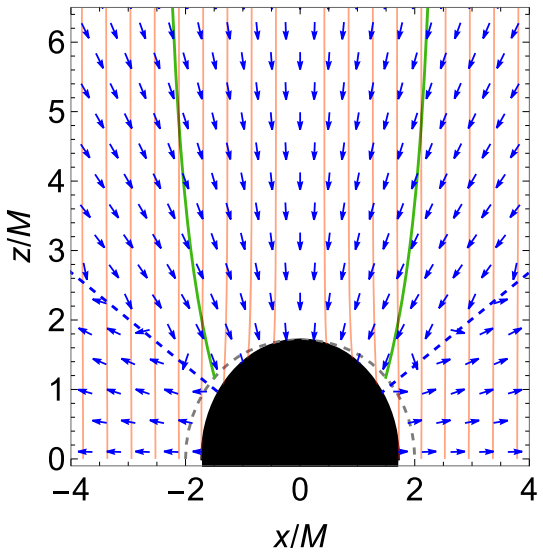

Fig. 1 BH horizon (filled-black), ergosphere (dashed-gray), $K_p = 0$ boundary (green), electric field lines (blue arrows) and magnetic field lines (red, contours of constant A_ϕ). The BH parameters are mass $M = 4M_\odot$, the spin parameter $a/M = 0.7$, and $B_0 = 4.4\times10^9$ G. For the present spin parameter, $\theta_c \approx 56.12°$, marked by the dashed-blue lines. The physical situation in the southern hemisphere is analogous due to equatorial symmetry. The figure shows the xz plane ($\phi = 0, \pi$) in Cartesian Kerr-Schild coordinates (see, e.g., [8])

leads to $(\vec{E}\cdot\vec{B})_H = (E_{\hat{r}}B_{\hat{r}})_H = E^H_{\hat{r}}B^H_{\hat{r}}$. Thus, the scalar product vanishes where either $E^H_{\hat{r}}$ or $B^H_{\hat{r}}$ vanishes. From Eq. (6a), we have $B^H_{\hat{r}} = 2\cos^2\theta B_0 M r_H(r_H^2 - a^2)/\Sigma_H^2$, which readily tells that $B^H_{\hat{r}} = 0$ on the equator, $\theta = \pi/2$. The solution of the equation $E^H_{\hat{r}} = 0$ is given by the angles θ_c that vanish the expression within the square brackets of Eq. (5a), i.e.,

$$\cos^2\theta_c = -\frac{\sigma}{2a^2} + \frac{r_H}{a}\sqrt{1+\left(\frac{\sigma}{2ar_H}\right)^2}, \tag{7}$$

where $\sigma = (r_H^2 - a^2)(r_H + M)/(r_H - M)$. We recall that this is a spherical polar angle, so it is positively measured clockwise from the polar axis, and it is in the range $[0, \pi]$. At second-order approximation in a/M, $\sigma \approx 2r_H(r_H + M)$ and the above expression reduces to the one of [38], $\cos^2\theta_c \approx r_H/[2(r_H+M)]$. At first order, $r_H \approx 2M$, so $\cos^2\theta_c \approx 1/3$.

Figure 1 shows the electric field lines (blue arrows) and the magnetic field lines (contours of constant A_ϕ, in red) for a BH with $a/M = 0.7$. We display only the northern hemisphere for the azimuthal angles $\phi = 0$ and $\phi = \pi$. The physical situation is analogous in the southern hemisphere, given the equatorial reflection symmetry of the Wald solution. For this spin value, Eq. (7) leads to $\theta_{c,1} \approx 56.12°$, shown by the dashed-blue line in the first quadrant (i.e., where $\phi = 0$, so $x > 0$ and $z > 0$). It also vanishes at $\theta_{c,2} \approx 123.88°$ which lies in the fourth quadrant, not shown in the figure. Because of the axial symmetry, the scalar product also vanishes along

a line given by the same $\theta_{c,1}$ and $\phi = \pi$, leading to the dashed-blue line in the second quadrant (i.e., where $x < 0$ and $z > 0$).

Therefore, these blue-dashed lines separate four regions where $\vec{E} \cdot \vec{B} \neq 0$, unveiling the quadrupole nature of the electric field. We call hereafter as *polar* the region within the two blue-dashed lines in the northern hemisphere. There is an analogous polar region in the southern hemisphere by equatorial reflection symmetry. We call as *equatorial* the region $\theta_{c,1} \leq \theta \leq \theta_{c,2}$. There is an analogous equatorial region in the western hemisphere by axial symmetry.

The electric field is nearly radial in these regions. It decreases nearly as $1/r^2$, just like it would exist a net *effective charge* [6,7], $|Q_{\rm eff}| = 2JB$. The net charge of the BH is zero, as testified by calculating the induced charge over the horizon. For this task, one integrates the induced surface charge density introduced by Hanni and Ruffini [39], given by the discontinuity of the electric field component perpendicular to the BH horizon, i.e., the radial electric field. An explicit calculation for the Kerr BH immersed in the magnetic field can be found in [8,40,41]. The induced charge on the two polar regions is of order $Q_{\rm eff}$ and is equal but of the opposite sign to the induced charge on the two equatorial regions [8]. The concept of effective charge has been useful in the analysis of the high-energy (MeV and GeV) emission of GRBs in the BdHN model (see, e.g., [6,7,42,43]). The above effective charge is also known as the Wald charge, Q_W, derived in [14] as the maximum charge the BH acquires by capturing charged particles along the polar axis, stopping accretion by the BH after it reaches $Q = Q_W$. We shall return to this point below in the conclusions.

3 Energy and angular momentum

Therefore, we focus on capturing charged particles with negative energy and angular momentum. The conserved energy and angular momentum of charged particles are shifted by the presence of the electromagnetic potential so that negative energies are achievable well beyond the ergosphere, and co-rotating particles can attain negative angular momentum (details below). Interesting analyses of the motion properties of charged particles in the Wald solution can be found in [44–46] (see also [47] for the case of photons but in the ergosphere).

The conserved energy and angular momentum of a particle of mass m_i and charge q_i are

$$E_i = -\pi_\mu \eta^\mu = -\pi_0, \qquad L_i = \pi_\mu \psi^\mu = \pi_3, \tag{8}$$

where $\pi_\alpha = p_\alpha + q_i A_\alpha$ is the canonical four-momentum, $p_\alpha = m_i u_\alpha$ the four-momentum, u_α the four-velocity, and $i = p, e$ stands for protons or electrons. Let us assume the particles are initially located at the position (r_i, θ_i, ϕ_i), at rest. The latter condition implies that the particle lies initially outside the ergosphere, i.e., $\Sigma_i > 2Mr_i$, so $r_i > r_{\rm erg} = M + \sqrt{M^2 - a^2\cos^2\theta_i}$, and the initial four-velocity is $u_i^\alpha = u_i^0 \delta_0^\alpha$, with $u_i^0 = (1 - 2Mr_i/\Sigma_i)^{-1/2}$. From Eq. (8), the energy and angular momentum at the initial position are

$$E_i = m_i\sqrt{1 - \frac{2Mr_i}{\Sigma_i}} \pm eaB_0\left[1 - \frac{Mr_i}{\Sigma_i}(1 + \cos^2\theta_i)\right], \tag{9a}$$

$$L_i = -m_i \frac{2Mar_i \sin^2\theta_i}{\sqrt{\Sigma_i(\Sigma_i - 2Mr_i)}} \pm \frac{1}{2}eB_0 \sin^2\theta_i\left[r_i^2 + a^2 - \frac{2Ma^2 r_i}{\Sigma_i}(1 + \cos^2\theta_i)\right], \tag{9b}$$

where e is the fundamental charge, the upper $(+)$ sign applies for protons and the lower $(-)$ sign for electrons. The terms due to the electromagnetic potential largely dominate in Eqs for astrophysical parameters (9). In the case $B_0 \gg 0.011(M_\odot/M)(m_i/m_e)$ G, $eB_0M \gg m_i$, so Eqs. (9) lead to polar protons with $E_p > 0$ and $L_p > 0$, and equatorial electrons with $E_e < 0$ and $L_e < 0$.

Those electrons' negative energy states are physically possible if (i) they do not reach infinity and (ii) a local observer measures positive kinetic energy. The first condition is automatically satisfied since equatorial electrons are accelerated inward. The four-velocity of a regular local observer at the horizon can be constructed by the linear combination of the spacetime Killing vectors [48]: $l^\mu = \eta^\mu + \Omega_H \psi^\mu$, being $\Omega_H = a/(2Mr_H)$ the BH angular velocity. Therefore, the kinetic energy this observer measures when the particles cross the event horizon is

$$K_i = -p_\mu l^\mu|_H = E_i - \Omega_H L_i. \tag{10}$$

For electrons, $K_e > 0$ at any angle in the equatorial region. For polar protons, the condition $K_p \geq 0$ constrains their initial position (r_p, θ_p), i.e., for given r_p, the boundary $K_p = 0$ defines a maximum value of θ_p, say θ_{K_p}. The maximum value of this angle occurs at $r_p = r_{\rm erg}$, say $\theta_{K_p,\max}$. Figure 1 shows the boundary $K_p = 0$ (dashed-green curves) for a BH with spin parameter $a/M = 0.7$, for which $\theta_{K_p,\max} \approx 51.81°$.

Charged particles will follow the magnetic field lines, and the latter point approximately in the $+z$ direction ($A_\phi = $ cons. implies $r\sin\theta \approx$ constant; see Fig. 1), so the BH can capture those particles whose initial position fulfills $r_i \sin\theta_i \leq r_H$. Thus, the BH captures polar protons at (r_p, θ_p) within $0 \leq \theta_p \leq \theta_{p,\max}$, where $\theta_{p,\max} = {\rm Min}(\theta_{K_p}, \theta_{p,\rm cyl})$, $\theta_{p,\rm cyl} = \arcsin(r_H/r_p)$, and equatorial electrons at (r_e, θ_e) within $\theta_c \leq \theta_e \leq \theta_{e,\max}$, where $\theta_{e,\max} = \theta_{e,\rm cyl} = \arcsin(r_H/r_e)$. Figure 2 shows $E_{p,e}$ and $L_{p,e}$ at initial positions that sat-

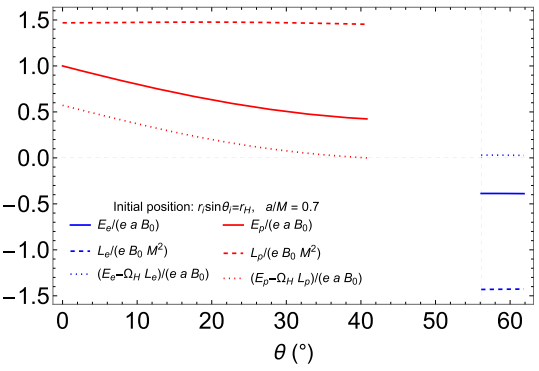

Fig. 2 E_i, L_i, given by Eq. (9), and $E_i - \Omega_H L_i$, at initial positions outside the ergosphere ($r_i > r_{\rm erg}$) leading to the particle capture by the BH in the example of Fig. 1

isfy the capture conditions mentioned above, specifically for protons initially located in the polar region at (r_p, θ_p), with $r_p = r_H/\sin\theta_p$ and $0 \leq \theta_p \leq \theta_{p,\rm max}$, and electrons in the equatorial region at (r_e, θ_e), with $r_e = r_H/\sin\theta_e$ and $\theta_c \leq \theta_e \leq \theta_{e,\rm max}$. For the present spin parameter, $a/M = 0.7$, the reference angles are $\theta_c \approx 56.12°$, $\theta_{p,\rm max} = \theta_{p,\rm cyl} \approx 40.80°$, and $\theta_{e,\rm max} = \theta_{e,\rm cyl} \approx 61.86°$.

4 Discussion and conclusion

We have analyzed the capture of charged particles by a Kerr BH embedded in a test, asymptotically aligned magnetic field given by the Wald solution. Paper [31] envisaged a situation in which the BH, by capturing charged particles along the rotation axis, gain charge up to a maximal possible value, $Q_W = 2JB_0$. After that point, the charged particle accretion should stop. Our results show that the physical situation can be more complicated and interesting. To account for the feedback of the particle capture on the BH parameters and, as we discuss below, the distribution of particles, are essential to draw any conclusions on the BH evolution. Indeed, the charged particles' energy and angular momentum at different radii and latitudes can lead to a very different scenario. Second, special attention must be paid to estimating the change of all BH parameters in the process, including its irreducible mass. The latter is of paramount relevance to assess the efficiency and plausibility of the energy extraction process.

When the BH captures a proton or electron, its mass, angular momentum, and irreducible mass change by

$$\delta M = E_i, \tag{11a}$$

$$\delta J = L_i, \tag{11b}$$

$$\delta M_{\rm irr} = \frac{M_{\rm irr}}{\sqrt{M^2 - a^2}}(\delta M - \Omega_H \delta J). \tag{11c}$$

Because $\delta M - \Omega_H \delta J = E_i - \Omega_H L_i = K_i \geq 0$ (see Fig. 2), we have $\delta M_{\rm irr}^2 \geq 0$, as expected [1–3]. Figure 2 shows that the equatorial region from which the BH captures electrons is smaller than the polar region from which it captures protons. The main reason is that the magnetic field lines are parallel to the z-axis in the Wald solution, even in the BH vicinity. This is confirmed by the magnetic flux threading the BH horizon

$$\Phi_B = \iint F_{23} d\theta d\phi, \tag{12}$$

which leads to the ratio of the polar to equatorial flux

$$\frac{1+\sqrt{5}}{2} < \frac{\Phi_B(0,\theta_c)}{\Phi_B(\theta_c,\pi/2)} = \frac{r_H}{2M}\tan^2\theta_c \leq 2, \tag{13}$$

for $0 \leq a/M < 1$. Thus, for the given magnetic field geometry, whether the net energy and angular momentum that the BH absorbs are negative or positive depending on the density of protons and electrons, n. Assuming local neutrality, protons, and electrons of number density n transfer to the BH an energy

$$\mathscr{E}_i \approx 2\pi \iint E_i n \sqrt{-g} dr d\theta, \tag{14a}$$

$$\mathscr{L}_i \approx 2\pi \iint L_i n \sqrt{-g} dr d\theta, \tag{14b}$$

where $g = -\Sigma^2 \sin^2\theta$ is the Kerr metric determinant. The constraints of the previous section give the integration boundaries. For a spherically symmetric density, $n = n(r)$, there are more capturable protons than electrons. The BH would acquire an energy $\mathscr{E} = \mathscr{E}_e + \mathscr{E}_p > 0$ and angular momentum $\mathscr{L} = \mathscr{L}_e + \mathscr{L}_p > 0$. An interesting situation occurs for an anisotropic density that increases towards the equator. As an example, Fig. 3 shows $\mathscr{E}_e$, $\mathscr{E}_p$, $\mathscr{L}_e$, $\mathscr{L}_p$, $\mathscr{E}$ and $\mathscr{L}$, for $n(r,\theta) = \mathscr{N}(r)\Psi(\theta)$, where $\mathscr{N}(r) = n_H(r_H/r)^m$, and $\Psi(\theta) = (1-\cos\theta)^2$, with $m = 2$, $n_H = 6.0 \times 10^{10}$ cm^{-3}, which corresponds to a rest-mass density $\rho = 10^{-13}$ g cm^{-3} near the BH horizon at the pole. We obtain $\mathscr{E}_p < |\mathscr{E}_e|$ and $\mathscr{L}_p < |\mathscr{L}_e|$, leading to $\mathscr{E} < 0$ and $\mathscr{L} < 0$, for values of the BH spin parameter $a/M \lesssim 0.5$.

Therefore, the long-standing question of how to extract the rotational energy of a Kerr BH is answered naturally by analyzing a rotating BH capturing not a single charged particle but a bunch of them of opposite charges, at different latitudes (see Fig. 2). We have shown, using the Wald solution, that the electrodynamical extraction of rotational energy works for an anisotropic density of protons and electrons increasing with latitude (see Figs. 2 and 3). Estimating the present rotational energy extraction process for different magnetic field configurations, matter accretion of varying nature, and more

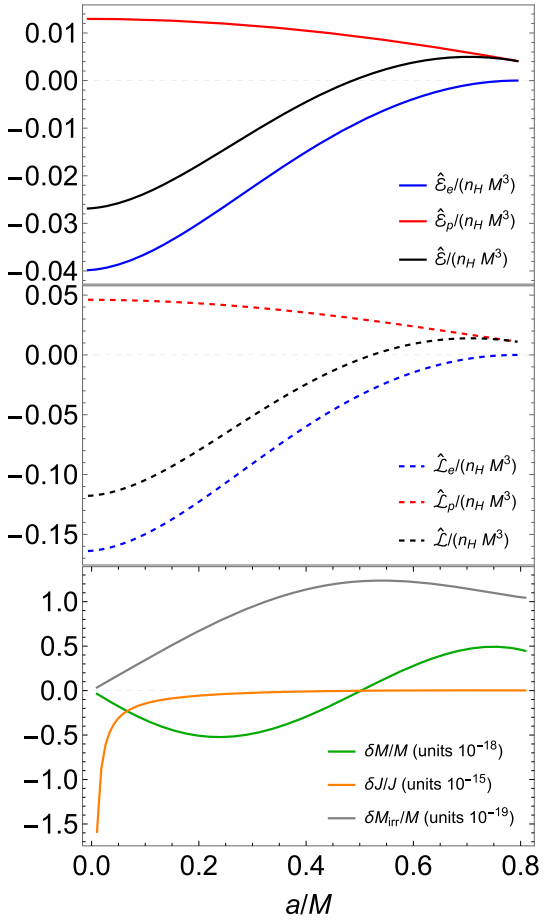

Fig. 3 Upper: $\hat{\mathcal{E}}_i = \mathcal{E}_i/(eB_0a)$ for polar protons (red) and equatorial electrons (blue) that cross the BH horizon. The net energy, $\hat{\mathcal{E}} = \hat{\mathcal{E}}_p + \hat{\mathcal{E}}_e$, is shown in black. Middle: analogous to the upper panel but for $\hat{\mathcal{L}}_i = \mathcal{L}_i/(eB_0M^2)$, and $\hat{\mathcal{L}}$. Lower: Fractional change of the BH mass, $\delta M/M$ (green, units of 10^{-18}), angular momentum, $\delta J/J$ (orange, units of 10^{-15}), and irreducible mass, $\delta M_{\rm irr}/M$ (gray, units of 10^{-19}). The particle density is $n(r,\theta) = \mathcal{N}(r)\Psi(\theta)$, where $\mathcal{N}(r) = n_H(r_H/r)^m$, with $m = 2$, $n_H = 6.0 \times 10^{10}$ cm^{-3}, and $\Psi(\theta) = (1-\cos\theta)^2$. In the upper and middle panels, the dimensionless energy and angular momentum are normalized by $n_H M^3$. This example uses $B_0 = B_c = 2\pi m_e^2 c^3/(e\,h) \approx 4.41 \times 10^{13}$ G

extended BH parameters, including non-vanishing electric charge, is now possible (Rueda and Ruffini, in preparation).

Data availability statement This manuscript has no associated data or the data will not be deposited. [Authors' comment: This article is of theoretical nature, so there is no data to be deposited.].

Funded by SCOAP^3. SCOAP^3 supports the goals of the International Year of Basic Sciences for Sustainable Development.

References

1. D. Christodoulou, Phys. Rev. Lett. **25**(22), 1596 (1970). https://doi.org/10.1103/PhysRevLett.25.1596
2. D. Christodoulou, R. Ruffini, Phys. Rev. D **4**, 3552 (1971). https://doi.org/10.1103/PhysRevD.4.3552
3. S.W. Hawking, Phys. Rev. Lett. **26**, 1344 (1971). https://doi.org/10.1103/PhysRevLett.26.1344
4. T. Piran, Rev. Mod. Phys. **76**, 1143 (2004). https://doi.org/10.1103/RevModPhys.76.1143
5. B. Zhang, *The Physics of Gamma-Ray Bursts* (Cambridge Univeristy Press, Cambridge, 2018). https://doi.org/10.1017/9781139226530
6. R. Ruffini, R. Moradi, J.A. Rueda, L. Becerra, C.L. Bianco, C. Cherubini, S. Filippi, Y.C. Chen, M. Karlica, N. Sahakyan, Y. Wang, S.S. Xue, Astrophys. J. **886**(2), 82 (2019). https://doi.org/10.3847/1538-4357/ab4ce6
7. R. Moradi, J.A. Rueda, R. Ruffini, Y. Wang, Astron. Astrophys. **649**, A75 (2021). https://doi.org/10.1051/0004-6361/201937135
8. J.A. Rueda, R. Ruffini, R.P. Kerr, Astrophys. J. **929**(1), 56 (2022). https://doi.org/10.3847/1538-4357/ac5b6e
9. J.A. Rueda, R. Ruffini, Eur. Phys. J. C **80**(4), 300 (2020). https://doi.org/10.1140/epjc/s10052-020-7868-z
10. R. Ruffini, R. Moradi, J.A. Rueda, L. Li, N. Sahakyan, Y.C. Chen, Y. Wang, Y. Aimuratov, L. Becerra, C.L. Bianco, C. Cherubini, S. Filippi, M. Karlica, G.J. Mathews, M. Muccino, G.B. Pisani, S.S. Xue, Mon. Not. R. Astron. Soc. **504**(4), 5301 (2021). https://doi.org/10.1093/mnras/stab724
11. R. Penrose, Nuovo Cimento Rivista Serie **1** (1969)
12. R. Penrose, R.M. Floyd, Nat. Phys. Sci. **229**(6), 177 (1971). https://doi.org/10.1038/physci229177a0
13. J.M. Bardeen, W.H. Press, S.A. Teukolsky, Astrophys. J. **178**, 347 (1972). https://doi.org/10.1086/151796
14. R.M. Wald, Astrophys. J. **191**, 231 (1974). https://doi.org/10.1086/152959
15. M. Bañados, J. Silk, S.M. West, Phys. Rev. Lett. **103**(11), 111102 (2009). https://doi.org/10.1103/PhysRevLett.103.111102
16. M. Bejger, T. Piran, M. Abramowicz, F. Håkanson, Phys. Rev. Lett. **109**(12), 121101 (2012). https://doi.org/10.1103/PhysRevLett.109.121101
17. J.D. Schnittman, Phys. Rev. Lett. **113**(26), 261102 (2014). https://doi.org/10.1103/PhysRevLett.113.261102
18. E. Berti, R. Brito, V. Cardoso, Phys. Rev. Lett. **114**(25), 251103 (2015). https://doi.org/10.1103/PhysRevLett.114.251103
19. S.V. Dhurandhar, N. Dadhich, Phys. Rev. D **30**(8), 1625 (1984). https://doi.org/10.1103/PhysRevD.30.1625
20. S. Parthasarathy, S.M. Wagh, S.V. Dhurandhar, N. Dadhich, Astrophys. J. **307**, 38 (1986). https://doi.org/10.1086/164390
21. A. Tursunov, N. Dadhich, Universe **5**(5), 125 (2019). https://doi.org/10.3390/universe5050125
22. R. Ruffini, J.R. Wilson, Phys. Rev. D **12**(10), 2959 (1975). https://doi.org/10.1103/PhysRevD.12.2959
23. R.D. Blandford, R.L. Znajek, Mon. Not. R. Astron. Soc. **179**, 433 (1977). https://doi.org/10.1093/mnras/179.3.433
24. P. Ghosh, M.A. Abramowicz, Mon. Not. R. Astron. Soc. **292**(4), 887 (1997). https://doi.org/10.1093/mnras/292.4.887
25. M. Livio, G.I. Ogilvie, J.E. Pringle, Astrophys. J. **512**(1), 100 (1999). https://doi.org/10.1086/306777

26. S.S. Komissarov, Mon. Not. R. Astron. Soc. **350**(2), 427 (2004). https://doi.org/10.1111/j.1365-2966.2004.07598.x
27. S.S. Komissarov, Mon. Not. R. Astron. Soc. **359**(3), 801 (2005). https://doi.org/10.1111/j.1365-2966.2005.08974.x
28. K. Parfrey, A. Philippov, B. Cerutti, Phys. Rev. Lett. **122**(3), 035101 (2019). https://doi.org/10.1103/PhysRevLett.122.035101
29. P.A. Sturrock, Astrophys. J. **164**, 529 (1971). https://doi.org/10.1086/150865
30. M.A. Ruderman, P.G. Sutherland, Astrophys. J. **196**, 51 (1975). https://doi.org/10.1086/153393
31. R.M. Wald, Phys. Rev. D **10**, 1680 (1974). https://doi.org/10.1103/PhysRevD.10.1680
32. P. Goldreich, W.H. Julian, Astrophys. J. **157**, 869 (1969). https://doi.org/10.1086/150119
33. R. Ruffini, J.D. Melon Fuksman, G.V. Vereshchagin, Astrophys. J. **883**(2), 191 (2019). https://doi.org/10.3847/1538-4357/ab3c51
34. L. Becerra, C.L. Ellinger, C.L. Fryer, J.A. Rueda, R. Ruffini, Astrophys. J. **871**(1), 14 (2019). https://doi.org/10.3847/1538-4357/aaf6b3
35. B. Carter, Phys. Rev. **174**(5), 1559 (1968). https://doi.org/10.1103/PhysRev.174.1559
36. J.M. Bardeen, Astrophys. J. **162**, 71 (1970). https://doi.org/10.1086/150635
37. T. Damour, R.S. Hanni, R. Ruffini, J.R. Wilson, Phys. Rev. D **17**(6), 1518 (1978). https://doi.org/10.1103/PhysRevD.17.1518
38. A.R. King, J.P. Lasota, W. Kundt, Phys. Rev. D **12**(10), 3037 (1975). https://doi.org/10.1103/PhysRevD.12.3037
39. R.S. Hanni, R. Ruffini, Phys. Rev. D **8**(10), 3259 (1973). https://doi.org/10.1103/PhysRevD.8.3259
40. K.S. Thorne, D. MacDonald, Mon. Not. R. Astron. Soc. **198**, 339 (1982). https://doi.org/10.1093/mnras/198.2.339
41. G. Miniutti, R. Ruffini, Nuovo Cimento B Serie **115**, 751 (2000)
42. R. Moradi, J.A. Rueda, R. Ruffini, L. Li, C.L. Bianco, S. Campion, C. Cherubini, S. Filippi, Y. Wang, S.S. Xue, Phys. Rev. D **104**(6), 063043 (2021). https://doi.org/10.1103/PhysRevD.104.063043
43. F. Rastegarnia, R. Moradi, J.A. Rueda, R. Ruffini, L. Li, S. Eslamzadeh, Y. Wang, S.S. Xue, Eur. Phys. J. C **82**(9), 778 (2022). https://doi.org/10.1140/epjc/s10052-022-10750-x
44. J. Levin, D.J. D'Orazio, S. Garcia-Saenz, Phys. Rev. D **98**(12), 123002 (2018). https://doi.org/10.1103/PhysRevD.98.123002
45. K. Gupta, Y.T.A. Law, J. Levin, Phys. Rev. D **104**(8), 084059 (2021). https://doi.org/10.1103/PhysRevD.104.084059
46. S.S. Komissarov, Mon. Not. R. Astron. Soc. **512**(2), 2798 (2022). https://doi.org/10.1093/mnras/stab2686
47. M. Kološ, A. Tursunov, Z. Stuchlík, Phys. Rev. D **103**(2), 024021 (2021). https://doi.org/10.1103/PhysRevD.103.024021
48. B. Carter, in Black Holes (Les Astres Occlus) (1973), pp. 57–214

universe

MDPI

Article

Neutron Star Binaries Produced by Binary-Driven Hypernovae, Their Mergers, and the Link between Long and Short GRBs

Laura M. Becerra [1,2,*,†], Chris Fryer [3,†], Jose F. Rodriguez [1,2,*,†], Jorge A. Rueda [2,4,5,6,7*,†] and Remo. Ruffini [2,4,8,†]

1 *GIRG*, Escuela de Física, Universidad Industrial de Santander, Bucaramanga 680002, Colombia
2 ICRANet, Piazza della Repubblica 10, 65122 Pescara, Italy
3 CCS-2, Los Alamos National Laboratory, Los Alamos, NM 87545, USA
4 ICRA, Dip. di Fisica, Sapienza Università di Roma, P.le Aldo Moro 5, 00185 Rome, Italy
5 ICRANet-Ferrara, Dip. di Fisica e Scienze Della Terra, Università Degli Studi di Ferrara, Via Saragat 1, 44122 Ferrara, Italy
6 Dip. di Fisica e Scienze della Terra, Università degli Studi di Ferrara, Via Saragat 1, 44122 Ferrara, Italy
7 INAF, Istituto de Astrofisica e Planetologia Spaziali, Via Fosso del Cavaliere 100, 00133 Rome, Italy
8 INAF, Viale del Parco Mellini 84, 00136 Rome, Italy
* Correspondence: laura.becerra7@correo.uis.edu.co (L.M.B.); joferoru@gmail.com (J.F.R.); jorge.rueda@icra.it (J.A.R.)
† These authors contributed equally to this work.

Abstract: The binary-driven hypernova (BdHN) model explains long gamma-ray bursts (GRBs) associated with supernovae (SNe) Ic through physical episodes that occur in a binary composed of a carbon-oxygen (CO) star and a neutron star (NS) companion in close orbit. The CO core collapse triggers the cataclysmic event, originating the SN and a newborn NS (hereafter νNS) at its center. The νNS and the NS accrete SN matter. BdHNe are classified based on the NS companion fate and the GRB energetics, mainly determined by the orbital period. In BdHNe I, the orbital period is of a few minutes, so the accretion causes the NS to collapse into a Kerr black hole (BH), explaining GRBs of energies $>10^{52}$ erg. BdHN II, with longer periods of tens of minutes, yields a more massive but stable NS, accounting for GRBs of 10^{50}–10^{52} erg. BdHNe III have still longer orbital periods (e.g., hours), so the NS companion has a negligible role, which explains GRBs with a lower energy release of $<10^{50}$ erg. BdHN I and II might remain bound after the SN, so they could form NS-BH and binary NS (BNS), respectively. In BdHN III, the SN likely disrupts the system. We perform numerical simulations of BdHN II to compute the characteristic parameters of the BNS left by them, their mergers, and the associated short GRBs. We obtain the mass of the central remnant, whether it is likely to be a massive NS or a BH, the conditions for disk formation and its mass, and the event's energy release. The role of the NS nuclear equation of state is outlined.

Keywords: neutron stars; gamma-ray burst; close binaries

Citation: Becerra, L.M.; Fryer, C.; Rodriguez, J.F.; Rueda, J.A.; Ruffini, R. Neutron Star Binaries Produced by Binary-Driven Hypernovae, Their Mergers, and the Link between Long and Short GRBs. *Universe* **2023**, *9*, 332. https://doi.org/10.3390/universe9070332

Academic Editor: Fridolin Weber

Received: 15 May 2023
Revised: 8 July 2023
Accepted: 9 July 2023
Published: 12 July 2023

1. Introduction

Gamma-ray bursts (GRBs) are classified using the time (in the observer's frame) T_{90}, in which 90% of the observed isotropic energy ($E_{\rm iso}$) in the gamma-rays is released. Long GRBs have $T_{90} > 2$ s and short GRBs, $T_{90} < 2$ s [1–5]. The two types of sources, short and long GRBs, are thought to be related to phenomena occurring in gravitationally collapsed objects, e.g., stellar-mass black holes (BHs) and neutron stars (NSs).

For short GRBs, mergers of binary NSs (BNSs) and/or NS-BH were soon proposed as progenitors [6–9]). For long bursts, the core-collapse of a single massive star leading to a BH (or a magnetar), a *collapsar* [10], surrounded by a massive accretion disk has been the traditional progenitor (see, e.g., [11,12], for reviews). The alternative binary-driven hypernova (BdHN) model exploits the increasing evidence for the relevance of a binary

progenitor for long GRBs, e.g., their association with Ic-type supernovae (SNe) [13–16], proposing a binary system composed of a carbon-oxygen star (CO) and an NS companion for long GRBs. We refer the reader to [17–23] for theoretical details on the model.

In this article, we are interested in the direct relationship between long and short GRBs predicted by the BdHN scenario. The CO undergoes core collapse, ejecting matter in a supernova (SN) explosion and forming a newborn NS (νNS) at its center. The NS companion attracts part of the ejected material leading to an accretion process with high infalling rates. Also, the νNS gains mass via a fallback accretion process. The orbital period is the most relevant parameter for the CO-NS system's fate. In BdHN of type I, the NS reaches the critical mass, gravitationally collapsing into a Kerr BH. It occurs for short orbital periods (usually a few minutes) and explains GRBs with energies above 10^{52} erg. In BdHN II, the orbital period is larger, up to a few tens of minutes, so the accretion rate decreases, and the NS becomes more massive but remains stable. These systems explain GRBs with energies 10^{50}–10^{52} erg. In BdHN III, the orbital separation is still larger; the NS companion does not play any role, and the energy release is lower than 10^{50} erg. If the binary is not disrupted by the mass loss in the SN explosion (see [20] for details), a BdHN I produces a BH-NS, whereas a BdHN II produces a BNS. In BdHN III, the SN is expected to disrupt the system. Therefore, in due time, the mergers of NS-BHs left by BdHNe I and of BNS left by BdHNe II are expected to lead to short GRBs.

Short GRBs from BNS mergers have been classified into short gamma-ray flashes (S-GRFs) and authentic short GRBs (S-GRBs), depending on whether the central remnant is an NS or a BH, respectively [24]. Two different subclasses of short GRBs from BNS mergers have been electromagnetically proposed [20,24,25]:

(1) *Authentic short GRBs (S-GRBs)*: short bursts with isotropic energy $E_{\rm iso} \gtrsim 10^{52}$ erg and peak energy$E_{p,i} \gtrsim 2$ MeV. They occur when a BH is formed in the merger, which is revealed by the onset of a GeV emission (see [25–27]). Their electromagnetically inferred isotropic occurrence rate is $\rho_{\rm S-GRB} \approx \left(1.9^{+1.8}_{-1.1}\right) \times 10^{-3}$ Gpc^{-3} year^{-1} [24]. The distinct signature of the formation of the BH, namely the observation of the 0.1–100 GeV emission by the *Fermi*-LAT, needs the presence of baryonic matter interacting with the newly-formed BH, e.g., via an accretion process (see, e.g., [26,28]).

(2) *Short gamma-ray flashes (S-GRFs)*: short bursts with $E_{\rm iso} \lesssim 10^{52}$ erg and $E_{p,i} \lesssim 2$ MeV. They occur when no BH is formed in the merger, i.e., when it leads to a massive NS. Their U-GRB electromagnetically inferred isotropic occurrence rate is $\rho_{\rm S-GRF} \approx 3.6^{+1.4}_{-1.0}$ Gpc^{-3} year^{-1} [24].

(3) *Ultrashort gamma-ray flashes (U-GRFs)*: in [20], it has been advanced a new class short bursts, the ultrashort GRBs (U-GRBs) produced by NS-BH binaries when the merger leaves the central BH with very little or completely without surrounding matter. An analogous system could be produced in BNS mergers. We shall call these systems ultrashort GRFs, for short U-GRFs. Their gamma-ray emission is expected to occur in a prompt short radiation phase. The post-merger radiation is drastically reduced, given the absence of baryonic matter to power an extended emission. A *kilonova* can still be observed days after the merger, in the infrared, optical, and ultraviolet wavelengths, produced by the radioactive decay of r-process yields [29–32]. Kilonova models used a *dynamical* ejecta composed of matter expelled by tides prior or during the merger, and a *disk-wind* ejecta by matter expelled from post-merger outflows in accretion disks [33], so U-GRFs are expected to have only the dynamical ejecta kilonova emission.

We focus on the BNSs left by BdHNe II and discuss how their properties impact the subsequent merger process and the associated short GRB emission, including their GW radiation. Since an accretion disk around the central remnant of a BNS merger, i.e., a newborn NS or a BH, is an important ingredient in models of short GRBs (see, e.g., [34] and references therein), we give some emphasis to the conditions and consequences for the merger leaving a disk. We study BNSs formed through binary evolution channels. Specifically, we expect these systems to form following a binary evolution channel similar to that of two massive stars leading to stripped-envelope binaries, described in previous studies (e.g., [35,36]). In this process, the CO star undergoes mass loss in multiple mass-

transfer and common-envelope phases through interactions with the NS companion (see, e.g., [37–39]). This leads to removing the H/He layers of the secondary star, which ends up as a CO star. Recently, significant progress has been made in the study of alternative evolution channels for the progenitor of BNSs, such as hierarchical systems involving triple and quadrupole configurations [40,41], which are motivated by the presence of massive stars in multiple systems [42]. These systems are out of the scope of this study.

The article is organized as follows. In Section 2, we discuss the numerical simulations of BdHNe and specialize in an example of a BNS led by a BdHN II. Section 3 introduces a theoretical framework to analyze the BNS merger outcome configuration properties based on the conservation laws of baryon number, angular momentum, and mass-energy. We present in Section 4 a specific example analyzing a BNS merger using the above-mentioned theoretical framework, including estimates of the energy and angular momentum release. We include the radiation in gravitational waves (GWs) and estimate its detection by current facilities. Section 5 presents a summary and the conclusions of this work.

2. A BNS Left by a BdHN II

Figure 1 shows a snapshot of the mass density with the vector velocity field at the binary's equatorial plane some minutes after the CO collapse and the expansion of the SN ejecta. The system's evolution was simulated with an SPH code, where the NS companion and the νNS are point particles that interact gravitationally with the SPH particles of the SN ejecta. For details of these numerical simulations, we refer to [23,43]. In these simulations, the influence of the star's magnetic field has be disregarded, as the magnetic pressure remains significantly lower than the random pressure exerted on the infalling material. The simulation of Figure 1 corresponds to a CO-NS for a CO star evolved from a zero-age main-sequence (ZAMS) star of $M_{\rm zams} = 15\ M_\odot$. The CO mass is about 3.06 $M_\odot$, whose core collapse leaves a 1.4 $M_\odot$ νNS and ejects 1.66 $M_\odot$. The NS companion's initial mass is 1.4 $M_\odot$, and the initial binary period of the system is about 4.5 min.

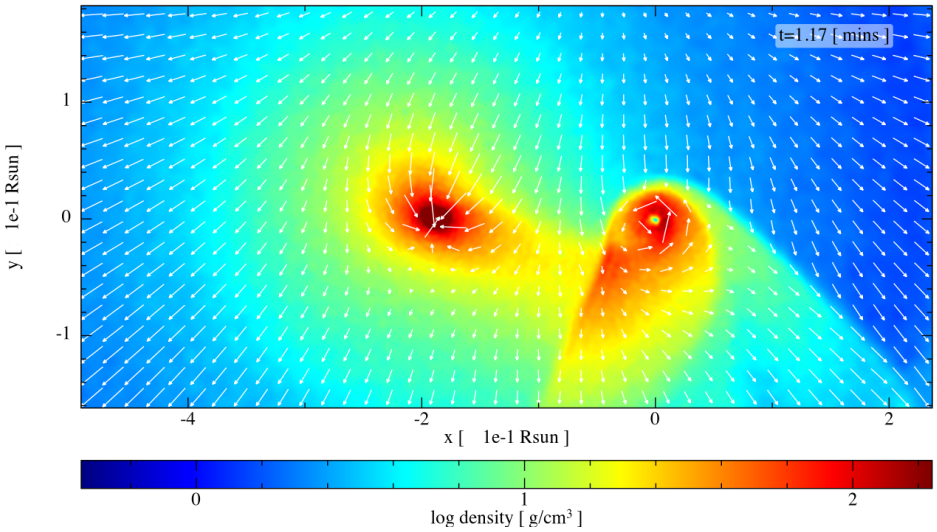

Figure 1. Massdensity snapshots and velocity field on the orbital plane of a BdHN for a CO left by a $M_{\rm zams} = 15\ M_\odot$ and a 1.4 $M_\odot$ NS companion, with an initial orbital period of about 4.5 min. We follow the expansion of the SN ejecta in the presence of the NS companion and the $\nu-$NS with a smoothed particle hydrodynamic (SPH) code. It is clear that a disk with opposite spins has formed around both stars.

From the accretion rate on the NSs, we have calculated the evolution of the mass and angular momentum of the binary components (see [43], for details). Table 1 summarizes the final parameters of the νNS and the NS, including the gravitational mass, m, dimensionless angular momentum, j, angular velocity, Ω, equatorial radius, $R_{\rm eq}$, and moment of inertia,

I. These structure parameters have been calculated with the RNS code [44] and using the GM1 [45,46] and TM1 [47] EOS (see Table 2 for details of the EOS). The BNS left by the BdHN II event has a period $P_{\rm orb} = 14.97$ min, orbital separation $a_{\rm orb} \approx 2 \times 10^{10}$ cm, and eccentricity $e = 0.45$.

Table 1. BNS produced by a BdHN II originated in a CO-NS with an orbital period of 4.5 min. The CO star mass is 3.06 $M_\odot$, obtained from the stellar evolution of a ZAMS star of $M_{\rm zams} = 15\ M_\odot$, and the NS companion has 1.4 $M_\odot$. The numerical smoothed-particle hydrodynamic (SPH) simulation follows the SN produced by the CO core collapse and estimates the accretion rate onto the νNS and the NS companion. The structure parameters of the NSs are calculated for the GM1 and TM1 EOS. We refer to [43] for additional details.

	m $[M_\odot]$	j	Ω [s^{-1}]	$R_{\rm eq}$ [km]	I [g cm^2]	Ω [s^{-1}]	$R_{\rm eq}$ [km]	I [g cm^2]
				GM1 EOS			TM1 EOS	
νNS	1.505	0.259	1114.6	14.03	2.04×10^{45}	1077.1	14.47	2.11×10^{45}
NS	1.404	−0.011	−52.14	14.01	1.85×10^{45}	−56.6	14.49	1.93×10^{45}

Table 2. Properties of the selected EOS. From left to right: maximum stable mass of non-rotating configurations, uniformly rotating configurations, set by the maximum mass of the Keplerian/mass-shedding sequence and the corresponding angular velocity.

EOS	$M_{\rm max}^{\rm j=0}$ $[M_\odot]$	$M_{\rm max}^{\rm j_{kep}}$ $[M_\odot]$	$\Omega_{\rm kep}^{\rm max}$ $[s^{-1}]$
GM1	2.38	2.84	1.001×10^4
TM1	2.19	2.62	8.83×10^3

3. Inferences from Conservation Laws

We analyze the properties of the central remnant NS formed after the merger. We use the conservation laws of baryon number, energy, and angular momentum for this aim.

3.1. Baryon Number Conservation

The total baryonic mass of the system must be conserved, so the binary baryonic mass, M_b, will redistribute among that of the postmerger's central remnant, $m_{b,c}$; the ejecta's mass, $m_{\rm ej}$, which is unbound to the system; and the matter kept bound to the system, e.g., in the form of a disk of mass m_d. Therefore, we have the constraint

$$M_b = m_{b,c} + m_{\rm ej} + m_d, \quad M_b = m_{b,1} + m_{b,2}. \tag{1}$$

For a uniformly rotating NS, the relation among its baryonic mass, $m_{b,i}$, gravitational mass, m_i, and angular momentum J_i, is well represented by the simple function

$$\frac{m_{b,i}}{M_\odot} \approx \frac{m_i}{M_\odot} + \frac{13}{200}\left(\frac{m_i}{M_\odot}\right)^2\left(1 - \frac{1}{130} j_i^{1.7}\right), \quad i = 1, 2, c, \tag{2}$$

where $j_i \equiv cJ_i/(GM_\odot^2)$, which fits numerical integration solutions of the axisymmetric Einstein equations for various nuclear EOS, with a maximum error of 2% [48]. Thus, Equation (2) is a nearly universal, i.e., EOS-independent, formula. Equation (2) applies to the merging components ($i = 1, 2$) as well as to the central remnant ($i = c$).

3.2. Angular Momentum Conservation

We can make more inferences about the merger's fate from the conservation of angular momentum. The angular momentum of the binary during the inspiral phase is given by

$$J = \mu r^2 \Omega + J_1 + J_2, \quad J_i = \frac{2}{5}\kappa_i m_i R_i^2 \Omega_i, \quad i = 1, 2, \tag{3}$$

where r is the orbital separation, $\mu = m_1 m_2 / M$ is the reduced mass, $M = m_1 + m_2$ is the total binary mass, and $\Omega = \sqrt{GM/r^3}$ is the orbital angular velocity. The gravitational mass and stellar radius of the i-th stellar component are, respectively, m_i and R_i; J_i is its angular momentum, Ω_i its angular velocity, and κ_i is the ratio between its moment of inertia to that of a homogeneous sphere. We adopt the convention $m_2 \leq m_1$. After the merger, the angular momentum is given by the sum of the angular momentum of the central remnant, the disk, and the ejecta. Angular momenta conservation implies that the angular momenta at merger, $J_{\rm merger}$, equals that of the final configuration plus losses:

$$J_{\rm merger} = J_c + J_d + \Delta J, \tag{4}$$

where J_c and J_d are, respectively, the angular momenta of the central remnant and the eventual surrounding disk, ΔJ accounts for angular momentum losses, e.g., via gravitational waves, and we have neglected the angular momentum carried out by the ejecta since it is expected to have small mass $\sim 10^{-4}$–$10^{-2}\ M_\odot$. Simulations suggest that this ejecta comes from interface of the merger, where matter is squeezed and ejected perpendicular to the orbital plane, see, e.g., [49,50]. The definition of the merger point will be discussed below.

The angular momentum of the binary at the merger point is larger than the maximum value a uniformly rotating NS can attain, i.e., the angular momentum at the Keplerian/mass-shedding limit, J_K. Thus, the remnant NS should evolve first through a short-lived phase that radiates the extra angular momentum over that limit and enters the rigidly rotating stability phase from the mass-shedding limit. Thus, we assume the remnant NS after that transition phase starts its evolution with angular momentum

$$J_c = J_K \approx 0.7 \frac{G m_c^2}{c}. \tag{5}$$

Equation (5) fits the angular momentum of the Keplerian sequence from full numerical integration of the Einstein equations and is nearly independent of the nuclear EOS (see, e.g., [48] and references therein). Therefore, the initial dimensionless angular momentum of the central remnant is

$$j_c = \frac{c J_c}{G M_\odot^2} \approx 0.7 \left(\frac{m_c}{M_\odot} \right)^2. \tag{6}$$

We model the disk's angular momentum as a ring at the remnant's inner-most stable circular orbit (ISCO). Thus, we use the formula derived in Cipolletta et al. [51], which fits, with a maximum error of 0.3%, the numerical results of the angular momentum per unit mass of a test particle circular orbit in the general relativistic axisymmetric field of a rotating NS. Within this assumption, the disk's angular momentum is given by

$$J_d = J_{\rm ISCO} \approx \frac{G}{c} m_c m_d \left[2\sqrt{3} - 0.37 \left(\frac{j_c}{m_c / M_\odot} \right)^{0.85} \right]. \tag{7}$$

Notice that Equation (7) reduces to the known result for the Schwarzschild metric for vanishing angular momentum, as it must. However, it differs from the result for the Kerr metric, which tells us that the Kerr metric does not describe the exterior spacetime of a rotating NS (see [51] for a detailed discussion).

The estimate of $J_{\rm merger}$ requires the knowledge of the merger point, which depends on whether or not the binary secondary becomes noticeably deformed by the tidal forces.

When the binary mass ratio $q \equiv m_2/m_1$ is close or equal to 1, the stars are only deformed before the point of contact [52]. Therefore, for $q \approx 1$, we can assume the point of the merger as the point of contact

$$r_{\rm merger} \approx r_{\rm cont} = \frac{(\mathcal{C}_2 + q\mathcal{C}_1)}{(1+q)\mathcal{C}_1\mathcal{C}_2}\frac{GM}{c^2}, \tag{8}$$

where $\mathcal{C}_{1,2} \equiv Gm_{1,2}/(c^2 R_{1,2})$ is the compactness of the BNS components.

When the masses are different, if we model the stars as Newtonian incompressible spheroids, there is a minimal orbital separation $r_{\rm ms}$, below which no equilibrium configuration is attainable, i.e., one star begins to shed mass to the companion due to the tidal forces. In this approximation, $r_{\rm ms} \approx 2.2 q^{-1/3} R_2$ [53]. Numerical relativity simulations of BH-NS quasi-equilibrium states suggest that the mass-shedding occurs at a distance (see [54] and references therein) of

$$r_{\rm ms} \approx (0.270)^{-2/3} q^{-1/3} R_2. \tag{9}$$

Our analysis adopts the mass-shedding distance of Equation (9). For a system with $q = 0.7$ (similar mass ratio of the one in Table 1), we have found that the less-compact star begins to shed mass before the point of contact, independently of the EOS, which agrees with numerical relativity simulations. Consequently, for non-symmetric binaries $q < 1$, we define the merging at the point as the onset of mass-shedding, $r_{\rm merger} \approx r_{\rm ms}$.

Based on the above two definitions of merger point, Equations (8) and (9), the angular momentum at the merger is given by

$$J_{\rm merger} = \begin{cases} \nu\sqrt{\frac{\mathcal{C}_2+q\mathcal{C}_1}{(1+q)\mathcal{C}_1\mathcal{C}_2}}\frac{GM^2}{c}, & q \approx 1, \\ \nu q^{1/3}[(1+q)\mathcal{C}_2]^{-1/2}\frac{GM^2}{c}, & q < 1, \end{cases} \tag{10}$$

where we have introduced the so-called symmetric mass-ratio parameter, $\nu \equiv q/(1+q)^2$.

3.3. Mass-Energy Conservation

The conservation of mass-energy before and after the merger implies the energy released equals the mass defect of the system, i.e.,

$$E_{\rm GW} + E_{\rm other} = \Delta M c^2 = [M - (m_c + m_{\rm ej} + m_d)]c^2, \tag{11}$$

where ΔM is the system's mass defect. We have also defined $E_{\rm GW} = E_{\rm GW}^{\rm insp} + E_{\rm GW}^{\rm pm}$ the total energy emitted in GWs in the inspiral regime, $E_{\rm GW}^{\rm insp}$, and in the merger and post-merger phases, $E_{\rm GW}^{\rm pm}$. The energy $E_{\rm other}$ is radiated in channels different from the GW emission, e.g., electromagnetic (photons) and neutrinos.

4. A Specific Example of BNS Merger

We analyze the merger of the $1.505 + 1.404\ M_\odot$ BNS in Table 1. For these component masses, the inferred orbital separation of $a_{\rm orb} \approx 2 \times 10^{10}$ cm and eccentricity $e = 0.45$, the merger is expected to be driven by GW radiation on a timescale [55] of

$$\tau_{\rm GW} = \frac{c^5}{G^3}\frac{5}{256}\frac{a_{\rm orb}^4}{\mu M^2}F(e) \approx 73.15\ {\rm kyr}, \quad F(e) = \frac{48}{19}\frac{1}{g(e)^4}\int_0^e \frac{g(e)^4(1-e^2)^{5/2}}{e(1+\frac{121}{304}e^2)}de \approx 0.44, \tag{12}$$

where $g(e) = e^{12/19}(1-e^2)^{-1}(1+121e^2/304)^{870/2299}$.

From Equations (2), (7) and (10), and the conservation Equations (1), (4) and (11), we can obtain the remnant and disk's mass as a function of the angular momentum losses, ΔJ, as well as an estimate of the energy and angular momentum released in the cataclysmic event. We use the NS structure parameters obtained for the GM1 EOS and the TM1 EOS. The total gravitational mass of the system is $M = m_1 + m_2 = 2.909\ M_\odot$, so using Equation (2), we obtain the total baryonic mass of the binary, $M_b = m_{b,1} + m_{b,2} \approx 3.184\ M_\odot$. The binary's mass fraction is $q = 0.933$, so we assume the merger starts at the contact point. With this,

the angular momentum at the merger, as given by Equation (10), for the GM1 and TM1 EOS is, respectively, $J_{\rm merger} \approx 5.65\, GM_\odot^2/c$ and $J_{\rm merger} \approx 5.73\, GM_\odot^2/c$.

Figure 2 shows that the disk's mass versus the central remnant's mass for selected values of the angular momentum loss for the two EOS. The figure shows the system's final parameters lie between two limiting cases: zero angular momentum loss leading to maximal disk mass and maximal angular momentum loss leading to zero disk mass.

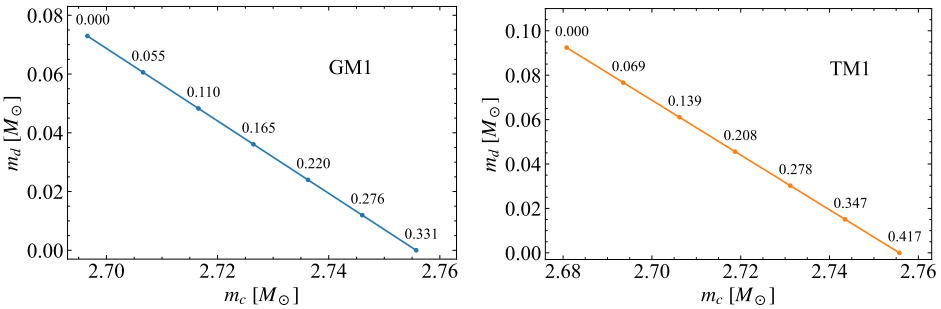

Figure 2. Disk mass versus central remnant (NS) mass. Selected values of the angular momentum loss (in units of $GM_\odot^2/c$) are shown as points. The initial BNS has a total gravitational mass of 2.909 $M_\odot$ and a mass fraction $q = 0.933$, so we assume the merger starts at the contact point. The maximum mass along the Keplerian sequence for the GM1 EOS is 2.84 $M_\odot$ and for the TM1 EOS it is 2.62 $M_\odot$ (see Table 2). Thus, for the former EOS, the central remnant is a massive fast-rotating NS, while the latter suggests a prompt collapse into a Kerr BH.

4.1. Maximal Disk Mass

We obtain the configuration corresponding to the maximum disk mass switching off angular momentum losses. Let us specialize in the GM1 EOS. By setting $\Delta J = 0$, the solution of the system of equations formed by the baryon number and angular conservation equations leads to the central remnant's mass, $m_c = 2.697\ M_\odot$, and disk's mass, $m_d = 0.073\ M_\odot$. This limiting case switches off the GW emission, so it also sets an upper limit to the energy released in mechanisms different than GWs. Thus, Equation (11) implies that $E_{\rm other} = \Delta M c^2 = [M - (m_c + m_{\rm ej} + m_d)]c^2 \approx (M - m_c - m_d)c^2 \approx 0.139\ M_\odot c^2 \approx 2.484 \times 10^{53}$ erg of energy are carried out to infinity by a mechanism different than GWs and not accompanied by angular momentum losses.

4.2. Zero Disk Mass

The other limiting case corresponds when the angular momentum loss and the remnant mass are maximized, i.e., when no disk is formed (see Figure 2). By setting $m_d = 0$, the solution of the conservation equations leads to the maximum angular momentum loss, $\Delta J = 0.331\ GM_\odot^2/c$, and the maximum remnant's mass, $m_c = 2.756\ M_\odot$.

Thus, the upper limit to the angular momentum carried out by GWs is given by the maximum amount of angular momentum losses, i.e., $\Delta J_{\rm GW} \lesssim 0.331\ GM_\odot^2/c$. In the inspiral phase of the merger, the system releases

$$E_{\rm GW}^{\rm insp} \approx \frac{Gm_1m_2}{2r_{\rm cont}} = \frac{q\mathcal{C}_1\mathcal{C}_2Mc^2}{2(1+q)(\mathcal{C}_2+q\mathcal{C}_1)} + \frac{1}{2}\left[j_1|\Omega_1| + j_2|\Omega_2|\right]\frac{GM_\odot^2}{c}. \tag{13}$$

For the binary we are analyzing, $E_{\rm GW}^{\rm insp} \approx 0.0194\, Mc^2 \approx 0.0563 M_\odot c^2 \approx 1.0073 \times 10^{53}$ erg. The transitional non-axisymmetric object (e.g., triaxial ellipsoid) formed immediately after the merger mainly generates these GWs, and their emission ends when the stable remnant NS is finally formed. We can model such a rotating object as a compressible ellipsoid with a polytropic EOS of index $n = 0.5$–1 [56]. The object will spin up by angular momentum loss to typical frequencies of 1.4–2.0 kHz. The energy emitted in GWs is $E_{\rm GW}^{\rm pm} \approx 0.0079\ M_\odot c^2 \approx 1.404 \times 10^{52}$ erg. Therefore, the energy released in GWs is,

$E_{\rm GW} = E_{\rm GW}^{\rm insp} + E_{\rm GW}^{\rm pm} \approx 0.0642\ M_\odot c^2 \approx 1.147 \times 10^{53}$ erg. If no disk is formed, i.e., for a U-GRF, the mass-energy defect is $\Delta M c^2 = [M - (m_c + m_{\rm ej})]c^2 \approx (M - m_c)c^2 \approx 0.153\ M_\odot c^2 \approx 2.734 \times 10^{53}$ erg. This implies that $E_{\rm other} = \Delta M c^2 - E_{\rm GW} \approx 0.089\ M_\odot c^2 \approx 1.591 \times 10^{53}$ erg are released in forms of energy different than GW radiation.

Therefore, combining the above two results, we conclude that for the present merger, assuming the GM1 EOS, the merger releases $0 < E_{\rm GW} \lesssim 1.147 \times 10^{53}$ erg in GWs and $1.591 \times 10^{53} \lesssim E_{\rm other} < 2.484 \times 10^{53}$ erg are released in other energy forms. The energy observed in short GRBs and further theoretical analysis, including numerical simulations of the physical processes occurring during the merger, will clarify the efficiency of converting $E_{\rm other}$ into observable radiation. Since no BH is formed (in this GM1 EOS analysis), the assumption that the merger leads to an S-GRF suggests an efficiency lower than 10%.

We now estimate the detection efficiency of the GW radiation released by the system in the post-merger phase when angular momentum losses are maximized, i.e., in the absence of a surrounding disk. We find the root-sum-squared strain of the signal, i.e.,

$$h_{\rm rss} = \sqrt{\int 2\left[|\tilde{h}_+|^2 + |\tilde{h}_\times|^2\right] df} \approx \frac{1}{\pi d \bar{f}} \sqrt{\frac{G E_{\rm GW}^{\rm pm}}{c^3}}, \tag{14}$$

where $\tilde{h}_+$ and $\tilde{h}_\times$ are the Fourier transforms of the GW polarizations, d is the distance to the source, $\bar{f}$ is the mean GW frequency in the postmerger phase. These signals are expected to be detected with a 50% of efficiency by the LIGO/Virgo pipelines [57] when $h_{\rm rss} \sim 10^{-22}$ Hz$^{-1/2}$ [58]. For the energy release in the post-merger phase, we have $\bar{f} = 1671.77$ Hz, so these signals could be detected up to a distance of $d \approx 10$ Mpc.

5. Discussion and Conclusions

As some BdHN I and II systems remain bound after the GRB-SN event, the corresponding NS-BH and BNS systems, driven by GW radiation, will merge and lead to short GRBs. For a few minutes binary, the merger time is of the order of 10^4 year. This implies that the binaries will still be close to the long GRB site by the merger time, which implies a direct link between long and short GRBs [20].

The occurrence rate of long and short bursts, however, should differ as the SN explosion likely disrupts the binaries with long orbital periods. We are updating our previous analysis on this interesting topic reported in [59]. We refer the reader to Bianco et al. [60] for a preliminary discussion.

As a proof of concept, this article examined this unique connection between long and short GRBs predicted by the BdHN scenario, emphasizing the case of mergers of BNS left by BdHNe II. For this particular case, the simulations predict that the outcome system will be a NSs binary with the star spins anti-aligned. The application of the present theoretical framework to the analysis of other merging binaries, such as the BH-NS binaries produced by BdHN I (see [20] for a general discussion), will be addressed in a separate work.

We have carried out a numerical SPH simulation of a BdHN II occurring in a CO-NS of orbital period 4.5 min. The mass of the CO is 3.06 $M_\odot$ and that of the NS companion, 1.4 $M_\odot$. The CO is the pre-SN star obtained from a ZAMS star of $M_{\rm zams} = 15\ M_\odot$ simulated from MESA code. The SPH simulation follows [23,43]. It computes the accretion rate onto the νNS (left by the CO core collapse) and the NS companion while the ejecta expands within the binary. For the event that left a νNS-NS eccentric binary of $1.505 + 1.404\ M_\odot$, orbital separation 2×10^{10} cm, orbital period of ≈15 min and eccentricity $e = 0.45$. The SN ejecta matter forms a disk around both stars with opposite spins, so we expect that the ν-NS binary will also have anti-aligned spins as well. The above parameters suggest the BNS merger leading to a short GRB occurs in ≈73 kyear after the BdHN II event.

Whether or not the central remnant of the BNS merger will be a Kerr BH or a massive, fast-rotating NS depends on the nuclear EOS. For instance, we have shown the GM1 EOS leads to the latter while the TM1 EOS leads to the former. As an example of the theoretical framework presented in this article, we quantify the properties of the merger using the GM1

EOS. We infer the mass of the NS central remnant and the surrounding disk as a function of the angular momentum losses. We then emphasize the merger features in the limiting cases of maximum and zero angular momentum loss, corresponding to a surrounding disk's absence or maximum mass. We estimated the maximum energy and angular momentum losses in GWs. We showed that the post-merger phase could release up to $\approx 10^{52}$ erg in $\approx$1.7 kHz GWs, and LIGO/Virgo could, in principle, detect such emissions for sources up to $\approx$10 Mpc. We assessed that up to a few 10^{53} erg of energy could be released in other forms of energy, so a $\lesssim$10% of efficiency of its conversion into observable electromagnetic radiation would lead to an S-GRF.

The direct link between long and short GRB progenitors predicted by the BdHN model opens the way to exciting astrophysical developments. For instance, the relative rate of BdHNe I and II and S-GRBs and S-GRFs might give crucial information on the nuclear EOS of NSs and the CO-NS parameters. At the same time, this information provides clues for the stellar evolution path of the binary progenitors leading to the CO-NS binaries of the BdHN scenario. Although challenging because of their expected ultrashort duration, observing a U-GRF would also be relevant for constraining the EOS of NS matter. An extended analysis is encouraged, including additional BNS parameters obtained from SPH simulations of BdHNe for various CO-NS systems and nuclear EOS.

Author Contributions: Conceptualization, L.M.B., C.F., J.F.R., J.A.R. and R.R.; methodology, L.M.B., J.F.R. and J.A.R.; formal analysis, L.M.B., J.F.R. and J.A.R.; investigation, L.M.B., J.F.R. and J.A.R.; writing—original draft, L.M.B., C.F., J.F.R., J.A.R. and R.R.; writing—review and editing, L.M.B., J.F.R. and J.A.R. All authors have read and agreed to the published version of the manuscript.

Funding: L.M.B. is supported by the Vicerrectoría de Investigación y Extensión—Universidad Industrial de Santander Postdoctoral Fellowship Program No. 2023000359. J.F.R. has received funding/support from the Patrimonio Autónomo—Fondo Nacional de Financiamiento para la Ciencia, la Tecnología y la Innovación Francisco José de Caldas (MINCIENCIAS–COLOMBIA) Grant No. 110685269447 RC-80740-465-2020, Project No. 69553.

Data Availability Statement: No new data were created or analyzed in this study. Data sharing is not applicable to this article.

Conflicts of Interest: The authors declare no conflict of interest.

Abbreviations

The following abbreviations are used in this manuscript:

BdHN	Binary-driven hypernova
BH	Black hole
BNS	Binary neutron star
CO	Carbon-oxygen
EOS	Equation of state
GRB	Gamma-ray burst
GW	Gravitational wave
ISCO	Innermost stable circular orbit
NS	Neutron star
νNS	Newborn neutron star
S-GRB	Short gamma-ray burst
S-GRF	Short gamma-ray flash
SN	Supernova
U-GRB	Ultrashort gamma-ray burst
U-GRF	Ultrashort gamma-ray flash
ZAMS	Zero-age main-sequence

References

1. Mazets, E.P.; Golenetskii, S.V.; Ilinskii, V.N.; Panov, V.N.; Aptekar, R.L.; Gurian, I.A.; Proskura, M.P.; Sokolov, I.A.; Sokolova, Z.I.; Kharitonova, T.V. Catalog of cosmic gamma-ray bursts from the KONUS experiment data. I. *Astrophys. Space Sci.* **1981**, *80*, 3–83. [CrossRef]
2. Klebesadel, R.W. The durations of gamma-ray bursts. In *Gamma-Ray Bursts—Observations, Analyses and Theories*; Ho, C., Epstein, R.I., Fenimore, E.E., Eds.; Cambridge University Press: Cambridge, UK, 1992; pp. 161–168.
3. Dezalay, J.P.; Barat, C.; Talon, R.; Syunyaev, R.; Terekhov, O.; Kuznetsov, A. Short cosmic events—A subset of classical GRBs? In *American Institute of Physics Conference Series*; Paciesas, W.S., Fishman, G.J., Eds.; AIP Publishing: Melville, NY, USA, 1992; Volume 265, pp. 304–309.
4. Kouveliotou, C.; Meegan, C.A.; Fishman, G.J.; Bhat, N.P.; Briggs, M.S.; Koshut, T.M.; Paciesas, W.S.; Pendleton, G.N. Identification of two classes of gamma-ray bursts. *Astrophys. J.* **1993**, *413*, L101–L104. [CrossRef]
5. Tavani, M. Euclidean versus Non-Euclidean Gamma-Ray Bursts. *Astrophys. J.* **1998**, *497*, L21–L24. [CrossRef]
6. Goodman, J. Are gamma-ray bursts optically thick? *Astrophys. J.* **1986**, *308*, L47. [CrossRef]
7. Paczynski, B. Gamma-ray bursters at cosmological distances. *Astrophys. J.* **1986**, *308*, L43–L46. [CrossRef]
8. Eichler, D.; Livio, M.; Piran, T.; Schramm, D.N. Nucleosynthesis, neutrino bursts and gamma-rays from coalescing neutron stars. *Nature* **1989**, *340*, 126–128. [CrossRef]
9. Narayan, R.; Piran, T.; Shemi, A. Neutron star and black hole binaries in the Galaxy. *Astrophys. J.* **1991**, *379*, L17–L20. [CrossRef]
10. Woosley, S.E. Gamma-ray bursts from stellar mass accretion disks around black holes. *Astrophys. J.* **1993**, *405*, 273–277. [CrossRef]
11. Mészáros, P. Theories of Gamma-Ray Bursts. *Annu. Rev. Astron. Astrophys.* **2002**, *40*, 137. [CrossRef]
12. Piran, T. The physics of gamma-ray bursts. *Rev. Mod. Phys.* **2004**, *76*, 1143–1210. [CrossRef]
13. Galama, T.J.; Vreeswijk, P.M.; van Paradijs, J.; Kouveliotou, C.; Augusteijn, T.; Bohnhardt, H.; Brewer, J.P.; Doublier, V.; Gonzalez, J.-F.; Leibundgut, B.; et al. An unusual supernova in the error box of the γ-ray burst of 25 April 1998. *Nature* **1998**, *395*, 670–672. [CrossRef]
14. Woosley, S.E.; Bloom, J.S. The Supernova Gamma-Ray Burst Connection. *Annu. Rev. Astron. Astrophys.* **2006**, *44*, 507–556. [CrossRef]
15. Della Valle, M. Supernovae and Gamma-Ray Bursts: A Decade of Observations. *Int. J. Mod. Phys. D* **2011**, *20*, 1745–1754. [CrossRef]
16. Hjorth, J.; Bloom, J.S. The Gamma-Ray Burst—Supernova Connection. In *Gamma-Ray Bursts*; Cambridge Astrophysics Series; Kouveliotou, C., Wijers, R.A.M.J., Woosley, S., Eds.; Cambridge University Press: Cambridge, UK, 2012; Volume 51, Chapter 9; pp. 169–190.
17. Rueda, J.A.; Ruffini, R. On the Induced Gravitational Collapse of a Neutron Star to a Black Hole by a Type Ib/c Supernova. *Astrophys. J.* **2012**, *758*, L7. [CrossRef]
18. Izzo, L.; Rueda, J.A.; Ruffini, R. GRB 090618: A candidate for a neutron star gravitational collapse onto a black hole induced by a type Ib/c supernova. *Astron. Astrophys.* **2012**, *548*, L5. [CrossRef]
19. Fryer, C.L.; Rueda, J.A.; Ruffini, R. Hypercritical Accretion, Induced Gravitational Collapse, and Binary-Driven Hypernovae. *Astrophys. J.* **2014**, *793*, L36. [CrossRef]
20. Fryer, C.L.; Oliveira, F.G.; Rueda, J.A.; Ruffini, R. Neutron-Star-Black-Hole Binaries Produced by Binary-Driven Hypernovae. *Phys. Rev. Lett.* **2015**, *115*, 231102. [CrossRef]
21. Becerra, L.; Cipolletta, F.; Fryer, C.L.; Rueda, J.A.; Ruffini, R. Angular Momentum Role in the Hypercritical Accretion of Binary-driven Hypernovae. *Astrophys. J.* **2015**, *812*, 100. [CrossRef]
22. Becerra, L.; Bianco, C.L.; Fryer, C.L.; Rueda, J.A.; Ruffini, R. On the Induced Gravitational Collapse Scenario of Gamma-ray Bursts Associated with Supernovae. *Astrophys. J.* **2016**, *833*, 107. [CrossRef]
23. Becerra, L.; Ellinger, C.L.; Fryer, C.L.; Rueda, J.A.; Ruffini, R. SPH Simulations of the Induced Gravitational Collapse Scenario of Long Gamma-Ray Bursts Associated with Supernovae. *Astrophys. J.* **2019**, *871*, 14. [CrossRef]
24. Ruffini, R.; Rueda, J.A.; Muccino, M.; Aimuratov, Y.; Becerra, L.M.; Bianco, C.L.; Kovacevic, M.; Moradi, R.; Oliveira, F.G.; Pisani, G.B.; et al. On the Classification of GRBs and Their Occurrence Rates. *Astrophys. J.* **2016**, *832*, 136. [CrossRef]
25. Ruffini, R.; Muccino, M.; Kovacevic, M.; Oliveira, F.G.; Rueda, J.A.; Bianco, C.L.; Enderli, M.; Penacchioni, A.V.; Pisani, G.B.; Wang, Y.; et al. GRB 140619B: A short GRB from a binary neutron star merger leading to black hole formation. *Astrophys. J.* **2015**, *808*, 190. [CrossRef]
26. Ruffini, R.; Muccino, M.; Aimuratov, Y.; Bianco, C.L.; Cherubini, C.; Enderli, M.; Kovacevic, M.; Moradi, R.; Penacchioni, A.V.; Pisani, G.B.; et al. GRB 090510: A Genuine Short GRB from a Binary Neutron Star Coalescing into a Kerr-Newman Black Hole. *Astrophys. J.* **2016**, *831*, 178. [CrossRef]
27. Ruffini, R.; Muccino, M.; Aimuratov, Y.; Amiri, M.; Bianco, C.L.; Chen, Y.C.; Eslam Panah, B.; Mathews, G.J.; Moradi, R.; Pisani, G.B.; et al. On the universal GeV emission in short GRBs. *arXiv* **2018**, arXiv:1802.07552.
28. Aimuratov, Y.; Ruffini, R.; Muccino, M.; Bianco, C.L.; Penacchioni, A.V.; Pisani, G.B.; Primorac, D.; Rueda, J.A.; Wang, Y. GRB 081024B and GRB 140402A: Two Additional Short GRBs from Binary Neutron Star Mergers. *Astrophys. J.* **2017**, *844*, 83. [CrossRef]
29. Li, L.X.; Paczyński, B. Transient Events from Neutron Star Mergers. *Astrophys. J.* **1998**, *507*, L59–L62. [CrossRef]

30. Metzger, B.D.; Martínez-Pinedo, G.; Darbha, S.; Quataert, E.; Arcones, A.; Kasen, D.; Thomas, R.; Nugent, P.; Panov, I.V.; Zinner, N.T. Electromagnetic counterparts of compact object mergers powered by the radioactive decay of r-process nuclei. *Mon. Not. R. Astron. Soc.* **2010**, *406*, 2650–2662. [CrossRef]
31. Tanvir, N.R.; Levan, A.J.; Fruchter, A.S.; Hjorth, J.; Hounsell, R.A.; Wiersema, K.; Tunnicliffe, R.L. A 'kilonova' associated with the short-duration γ-ray burst GRB 130603B. *Nature* **2013**, *500*, 547–549. [CrossRef]
32. Berger, E.; Fong, W.; Chornock, R. An r-process Kilonova Associated with the Short-hard GRB 130603B. *Astrophys. J.* **2013**, *774*, L23. [CrossRef]
33. Metzger, B.D. Kilonovae. *Living Rev. Relativ.* **2017**, *20*, 3. [CrossRef]
34. Berger, E. Short-Duration Gamma-Ray Bursts. *Annu. Rev. Astron. Astrophys.* **2014**, *52*, 43–105. [CrossRef]
35. Tauris, T.M.; Langer, N.; Podsiadlowski, P. Ultra-stripped supernovae: Progenitors and fate. *Mon. Not. R. Astron. Soc.* **2015**, *451*, 2123–2144. [CrossRef]
36. Tauris, T.M.; Kramer, M.; Freire, P.C.C.; Wex, N.; Janka, H.T.; Langer, N.; Podsiadlowski, P.; Bozzo, E.; Chaty, S.; Kruckow, M.U.; et al. Formation of Double Neutron Star Systems. *Astrophys. J.* **2017**, *846*, 170. [CrossRef]
37. Nomoto, K.; aki Hashimoto, M. Presupernova evolution of massive stars. *Phys. Rep.* **1988**, *163*, 13–36. [CrossRef]
38. Kim, H.J.; Yoon, S.C.; Koo, B.C. Observational Properties of Type Ib/c Supernova Progenitors in Binary Systems. *Astrophys. J.* **2015**, *809*, 131. [CrossRef]
39. Yoon, S.C. Evolutionary Models for Type Ib/c Supernova Progenitors. *Publ. Astron. Soc. Aust.* **2015**, *32*, e015. [CrossRef]
40. Hamers, A.S.; Fragione, G.; Neunteufel, P.; Kocsis, B. First- and second-generation black hole and neutron star mergers in 2+2 quadruples: Population statistics. *Mon. Not. R. Astron. Soc.* **2021**, *506*, 5345–5360. [CrossRef]
41. Vynatheya, P.; Hamers, A.S. How Important Is Secular Evolution for Black Hole and Neutron Star Mergers in 2+2 and 3+1 Quadruple-star Systems? *Astrophys. J.* **2022**, *926*, 195. [CrossRef]
42. Sana, H.; de Mink, S.E.; de Koter, A.; Langer, N.; Evans, C.J.; Gieles, M.; Gosset, E.; Izzard, R.G.; Le Bouquin, J.B.; Schneider, F.R.N. Binary Interaction Dominates the Evolution of Massive Stars. *Science* **2012**, *337*, 444. [CrossRef]
43. Becerra, L.M.; Moradi, R.; Rueda, J.A.; Ruffini, R.; Wang, Y. First minutes of a binary-driven hypernova. *Phys. Rev. D* **2022**, *106*, 083002. [CrossRef]
44. Stergioulas, N.; Friedman, J.L. Comparing Models of Rapidly Rotating Relativistic Stars Constructed by Two Numerical Methods. *Astrophys. J.* **1995**, *444*, 306. [CrossRef]
45. Glendenning, N.K.; Moszkowski, S.A. Reconciliation of neutron-star masses and binding of the Lambda in hypernuclei. *Phys. Rev. Lett.* **1991**, *67*, 2414–2417. [CrossRef] [PubMed]
46. Pal, S.; Bandyopadhyay, D.; Greiner, W. Antikaon condensation in neutron stars. *Nucl. Phys. A* **2000**, *674*, 553–577. [CrossRef]
47. Sugahara, Y.; Toki, H. Relativistic mean-field theory for unstable nuclei with non-linear σ and ω terms. *Nucl. Phys. A* **1994**, *579*, 557–572. [CrossRef]
48. Cipolletta, F.; Cherubini, C.; Filippi, S.; Rueda, J.A.; Ruffini, R. Fast rotating neutron stars with realistic nuclear matter equation of state. *Phys. Rev. D* **2015**, *92*, 023007. [CrossRef]
49. Oechslin, R.; Janka, H.T.; Marek, A. Relativistic neutron star merger simulations with non-zero temperature equations of state. I. Variation of binary parameters and equation of state. *Astron. Astrophys.* **2007**, *467*, 395–409. [CrossRef]
50. Bauswein, A.; Goriely, S.; Janka, H.T. Systematics of Dynamical Mass Ejection, Nucleosynthesis, and Radioactively Powered Electromagnetic Signals from Neutron-star Mergers. *Astrophys. J.* **2013**, *773*, 78. [CrossRef]
51. Cipolletta, F.; Cherubini, C.; Filippi, S.; Rueda, J.A.; Ruffini, R. Last stable orbit around rapidly rotating neutron stars. *Phys. Rev. D* **2017**, *96*, 024046. [CrossRef]
52. Bernuzzi, S. Neutron star merger remnants. *Gen. Relativ. Gravit.* **2020**, *52*, 108. [CrossRef]
53. Chandrasekhar, S. *Ellipsoidal Figures of Equilibrium*; Dover: New York, NY, USA, 1969.
54. Shibata, M.; Taniguchi, K. Coalescence of Black Hole-Neutron Star Binaries. *Living Rev. Relat.* **2011**, *14*, 6. [CrossRef]
55. Maggiore, M. *Gravitational Waves: Volume 1: Theory and Experiments*; Oxford University Press: Oxford, UK, 2007.
56. Lai, D.; Shapiro, S.L. Gravitational radiation from rapidly rotating nascent neutron stars. *Astrophys. J.* **1995**, *442*, 259–272. [CrossRef]
57. Abbott, B.P.; Abbott, R.; Abbott, T.D.; Abernathy, M.R.; Acernese, F.; Ackley, K.; Adams, C.; Adams, T.; Addesso, P.; Adhikari, R.X.; et al. All-sky search for long-duration gravitational wave transients in the first Advanced LIGO observing run. *Class. Quantum Gravity* **2018**, *35*, 065009. [CrossRef]
58. Abbott, B.P.; Abbott, R.; Abbott, T.D.; Acernese, F.; Ackley, K.; Adams, C.; Adams, T.; Addesso, P.; Adhikari, R.X.; Adya, V.B.; et al. Search for Post-merger Gravitational Waves from the Remnant of the Binary Neutron Star Merger GW170817. *Astrophys. J.* **2017**, *851*, L16. [CrossRef]

59. Ruffini, R.; Rodriguez, J.; Muccino, M.; Rueda, J.A.; Aimuratov, Y.; Barres de Almeida, U.; Becerra, L.; Bianco, C.L.; Cherubini, C.; Filippi, S.; et al. On the Rate and on the Gravitational Wave Emission of Short and Long GRBs. *Astrophys. J.* **2018**, *859*, 30. [CrossRef]
60. Bianco, C.L.; Mirtorabi, M.T.; Moradi, R.; Rastegarnia, F.; Rueda, J.A.; Ruffini, R.; Wang, Y.; Della Valle, M.; Li, L.; Zhang, S.R. Probing electromagnetic-gravitational wave emission coincidence in type I binary-driven hypernova family of long GRBs at very-high redshift. *arXiv* **2023**, arXiv:2306.05855. [CrossRef]

universe

MDPI

Article

Matching Slowly Rotating Spacetimes Split by Dynamic Thin Shells

Jonas P. Pereira [1,2,*] and Jorge A. Rueda [3,4,5,6]

[1] Núcleo de Astrofísica e Cosmologia (Cosmo-Ufes) & Departamento de Física, Universidade Federal do Espírito Santo, Vitória 29075-910, ES, Brazil
[2] Nicolaus Copernicus Astronomical Center, Polish Academy of Sciences, 00-716 Warsaw, Poland
[3] ICRA, Dipartimento di Fisica, Sapienza Università di Roma, Piazzale Aldo Moro 5, I-00185 Roma, Italy; jorge.rueda@icra.it
[4] ICRANet, Piazza della Repubblica 10, I-65122 Pescara, Italy
[5] ICRANet-Ferrara, Dipartimento di Fisica e Scienze della Terra, Università degli Studi di Ferrara, Via Saragat 1, I-44122 Ferrara, Italy
[6] INAF, Istituto di Astrofisica e Planetologia Spaziali, Via Fosso del Cavaliere 100, I-00133 Rome, Italy
* Correspondence: jpereira@camk.edu.pl

Abstract: We investigated within the Darmois–Israel thin-shell formalism the match of neutral and asymptotically flat, slowly rotating spacetimes (up to second order in the rotation parameter) when their boundaries are dynamic. It has several important applications in general relativistic systems, such as black holes and neutron stars, which we exemplify. We mostly focused on the stability aspects of slowly rotating thin shells in equilibrium and the surface degrees of freedom on the hypersurfaces splitting the matched slowly rotating spacetimes, e.g., surface energy density and surface tension. We show that the stability upon perturbations in the spherically symmetric case automatically implies stability in the slow rotation case. In addition, we show that, when matching slowly rotating Kerr spacetimes through thin shells in equilibrium, the surface degrees of freedom can decrease compared to their Schwarzschild counterparts, meaning that the energy conditions could be weakened. The frame-dragging aspects of the match of slowly rotating spacetimes are also briefly discussed.

Keywords: slow rotation; neutron stars; black holes; Darmois–Israel formalism; surface degrees of freedom; surface energy density; surface tension; general relativity; frame-dragging effect

Citation: Pereira, J.P.; Rueda, J.A. Matching Slowly Rotating Spacetimes Split by Dynamic Thin Shells. *Universe* **2023**, *9*, 305. https://doi.org/10.3390/universe9070305

Academic Editor: Herbert W. Hamber

Received: 16 May 2023
Revised: 21 June 2023
Accepted: 22 June 2023
Published: 24 June 2023

1. Introduction

Although matching two spherically symmetric spacetimes is a simple task (see [1], for instance), this is not the case for axially symmetric ones [2]. Nevertheless, particular glues have already been applied to several scenarios and contexts in the slow rotation case. We mention, for instance, the collapse of slowly rotating thin shells (onto already formed black holes [3], generating slowly rotating black holes [4], or associated with regular interior spacetimes [5]), the analysis of the kinematical effects that slowly rotating spacetime glues should exhibit [6,7], and scalar fields non-minimally coupled to glued spacetimes [8]. Concerning the match of slowly rotating spacetimes up to second order in the rotation parameter, the work of de La Cruz and Israel [3] is noteworthy. They did this for the first time by joining the Minkowski and the Kerr spacetimes using prescribed axially symmetric hypersurfaces in equilibrium. It was shown that there are infinite ways of joining these spacetimes, each characterized by a spinning shell with a different degree of ellipticity. In addition, the rigid rotation of observers inside the shell with the shell itself does not occur generally. It was not the interest of that work to assess the stability of the equilibrium radii.

Another more recent example of an interesting glue is the work of Uchikata and Yoshida [5], who investigated the matching of a slowly rotating Kerr–Newman spacetime with the de Sitter one using a thin shell in equilibrium (its stability was not investigated either). As

expected, they also found that the surface degrees of freedom are polar-angle-dependent on the thin shell. Cases were found where the surface energy density could be negative, but the authors deemed them unphysical. For further interesting slowly rotating thin-shell applications, see [9–14] and the references therein.

Clear aspects of matching axially symmetric spacetimes are the possibility of having manifolds without singularities and the possibility of more realistic models for astrophysical systems. In addition, the dragging of inertial frames is inherent in these spacetimes. We show here how this kinematic effect would allow us to scrutinize layered systems in astrophysics, shedding some light on their constitution.

We addressed the problem of matching neutral, arbitrary, slowly rotating Hartle spacetimes split by dynamic hypersurfaces, examining some of their subtleties. To the best of our knowledge, this has not been performed before. We limit our analysis to the second order in the rotation parameter since it is not known how to generically glue two axially symmetric spacetimes with arbitrary rotation parameters. As a byproduct of our investigation, we show, for instance, that the stability of thin shells in the spherically symmetric case automatically implies the stability of thin shells when slow rotation (up to second order in the rotation parameter) is present. In addition, we show that there are (realistic) situations where the corrections to the surface energy density and surface tension in the spherically symmetric case are negative. This seems to be of interest, as it would point to the likelihood of violating some energy conditions in some regions of surfaces of discontinuity in the non-perturbative context.

This article is organized as follows. In the next section, we deal with the problem of matching two slowly rotating Hartle spacetimes split by a dynamic hypersurface. Section 3 is devoted to the solution of the established system of equations for static and away-from-equilibrium hypersurfaces. The generalizations of the surface energy density and surface tension in the case of slow rotation are presented in Section 4. Kinematic effects associated with our generic glues are addressed in Section 5. In Section 6, we apply our formalism to the important case of matching two Kerr spacetimes and investigate the behavior of surface quantities and some aspects of the energy conditions. A summary and many astrophysical applications of our work can be found in Section 7.

We use geometric units throughout the article and the metric signature -2.

2. Matching Slowly Rotating Spacetimes

In the slowly rotating case, following Hartle [15], we assumed that each spacetime that we glue can be written as

$$\begin{aligned} ds^2 &= e^{\nu(r)}[1+2\epsilon^2 h(r,\theta)]dt^2 - e^{\lambda(r)}[1+2\epsilon^2 j(r,\theta)]dr^2 \\ &- r^2[1+2\epsilon^2 k(r,\theta)](d\theta^2+\sin^2\theta\{d\varphi-\epsilon\omega(r)dt\}^2), \end{aligned} \tag{1}$$

where

$$h(r,\theta) = h_0(r) + h_2(r)P_2(\cos\theta), \tag{2}$$
$$j(r,\theta) = j_0(r) + j_2(r)P_2(\cos\theta), \tag{3}$$
$$k(r,\theta) = k_2(r)P_2(\cos\theta). \tag{4}$$

As usual, we define $P_2(\cos\theta)$ as the second-order Legendre polynomial [$P_2(\cos\theta) = (3\cos^2\theta - 1)/2$].

In these approximations, we go up to the *second order in the rotation parameter*, fingerprinted by the dummy (dimensionless) quantity "ϵ". It was put in Equation (1) just as a mere indicator of the order of the rotational expansion taken into account. The functions h, j, k, ω as given by Equations (2)–(4) are to be found by Einstein's equations in the scope of axially symmetric solutions (see Reference [15] for the associated equations, some solutions, and properties). The background spacetime that is the seed for the Hartle metric is a

spherically symmetric one (for the case of a BH spacetime, it would be the Schwarzschild metric), as can be seen by putting $\epsilon = 0$ in Equation (1).

To match two spacetimes (which can then be used to obtain spacetimes made up of an arbitrary number of glues), one must also know their common hypersurface (that is to say, it must be well-defined), as well as how the coordinates of each manifold are related to the ones defined on such a hypersurface. Once this is obtained, finding the surface energy–momentum tensor that would allow such a glue is more of an algebraic exercise, made possible mainly by Lanczos' and Israel's seminal works [1,16–18].

To begin with, let us choose the intrinsic coordinates of the splitting hypersurface, defined as Σ, as $y^a = (\tilde{\tau}, \tilde{\theta}, \tilde{\varphi})$. For now, $\tilde{\tau}$ is just a label for a time-like coordinate on Σ. Further ahead, such a choice will be justified when we try to relate it to the proper time measured by observers on Σ, at least to some order in "ϵ". We shall assume that the equation for Σ is given by

$$\Psi(r, \tilde{\tau}, \tilde{\theta}) = 0, \quad \Psi(r, \tilde{\tau}, \tilde{\theta}) = r - R(\tilde{\tau}) - \epsilon^2 B(\tilde{\tau}, \tilde{\theta}). \tag{5}$$

Up to this point, R and B are unknown functions, and "ϵ" indicates the rotational order of the factors involved. In addition, let us assume that the spacetime coordinates relate to the ones of the hypersurface as

$$t = T(\tilde{\tau}) + \epsilon^2 A(\tilde{\tau}, \tilde{\theta}), \;\; \theta = \tilde{\theta}, \;\; d\varphi = d\tilde{\varphi} + \epsilon C(\tilde{\tau}) d\tilde{\tau}. \tag{6}$$

Just not to overload the notation, we dropped the "$\pm$" indexes that should be present in the coordinates of the spacetimes to be matched. Such labels would be related to a region above ("$+$") and below ("$-$") Σ, naturally defined by its normal vector.

With the ansatz given by Equations (5) and (6), our task is to find the functions A, B, C, R, and T that lead the metrics given by Equation (1) to be continuous when projected onto Σ (continuity of the first fundamental form). This is the first junction condition to be imposed when matching spacetimes whose resultant one leads to a distributional solution to Einstein's equations [18]. From Equations (1) and (6), we have to impose that (for any F, $\dot{F} \equiv \partial F / \partial \tilde{\tau}$):

$$C = \omega(R) \dot{T} \tag{7}$$

and

$$e^{\nu(R)} \dot{T}^2 - e^{\lambda(R)} \dot{R}^2 = 1, \tag{8}$$

to eliminate the first-order terms in the rotational parameter of the induced metric and retrieve our spherically symmetric solution with $\tilde{\tau}$ as the proper time on Σ. From Equation (8), we see that the well-definiteness of the induced metric does not constrain $R(\tilde{\tau})$; it is a free function whose dynamics will be related to the spherically symmetric configuration. We know from such a case that its determination is only possible when an equation of state for the (perfect-like) fluid on Σ is given [1,19,20].

Since we are working perturbatively in "ϵ", we can expand the functions A and B up to the second-order Legendre polynomials in the same fashion as it was done previously for h, j, k. Therefore, let us assume

$$B(\tilde{\tau}, \tilde{\theta}) = B_0(\tilde{\tau}) + B_2(\tilde{\tau}) P_2(\cos\tilde{\theta}), \tag{9}$$

and

$$A(\tilde{\tau}, \tilde{\theta}) = A_0(\tilde{\tau}) + A_2(\tilde{\tau}) P_2(\cos\tilde{\theta}). \tag{10}$$

On the hypersurface, Σ, the functions h_0, j_0, h_2, j_2, and k_2 (see Equations (2)–(4)) have their radial dependence just replaced by R, given that they are already second-order functions in

the rotational parameter. This notwithstanding, the spherically symmetric function e^{ν} on the hypersurface Σ, on account of Equations (5) and (9), changes to

$$e^{\nu(r)} \approx e^{\nu(R)}\left(1+\frac{\partial \nu}{\partial R}\epsilon^2 B\right), \tag{11}$$

similar to e^{λ}. Therefore, further corrections appear when one works up to ϵ^2. The one given by Equation (11) is due to the shape change of Σ due to rotation.

From Equations (1), (6)–(8) and (11), the induced metric on Σ can be cast as

$$\begin{aligned} ds^2_{\Sigma} &= d\tilde{\tau}^2\left\{1+\epsilon^2\left[e^{\nu(R)}\left(2\dot{T}\dot{A}+2h\dot{T}^2+\frac{\partial \nu}{\partial R}B\dot{T}^2\right)-e^{\lambda(R)}\left(2\dot{R}\dot{B}+2j\dot{R}^2+\frac{\partial \lambda}{\partial R}B\dot{R}^2\right)\right]\right\} \\ &+ 2\epsilon^2\left(e^{\nu(R)}\dot{T}\frac{\partial A}{\partial \tilde{\theta}}-e^{\lambda(R)}\dot{R}\frac{\partial B}{\partial \tilde{\theta}}\right)d\tilde{\tau}d\tilde{\theta}-(R^2+2RB+2kR^2)(d\tilde{\theta}^2+\sin\tilde{\theta}^2 d\tilde{\varphi}^2). \end{aligned} \tag{12}$$

If we now substitute Equations (2)–(4), (9) and (10) into Equation (12), the well-definiteness of the induced metric on Σ is guaranteed by means of the following conditions:

$$e^{\nu(R)}\left(\dot{T}\dot{A}_0+h_0\dot{T}^2\right)-e^{\lambda(R)}\left(\dot{R}\dot{B}_0+j_0\dot{R}^2\right)+\frac{B_0}{2}\left(e^{\nu(R)}\dot{T}^2\frac{\partial \nu}{\partial R}-e^{\lambda(R)}\dot{R}^2\frac{\partial \lambda}{\partial R}\right)=0, \tag{13}$$

$$e^{\nu(R)}\dot{T}A_2 = e^{\lambda(R)}\dot{R}B_2, \tag{14}$$

$$[B_2+k_2R]^{+}_{-}=0, \tag{15}$$

$$[B_0]^{+}_{-}=0, \tag{16}$$

$$[\alpha_2]^{+}_{-}=0, \tag{17}$$

with

$$\alpha_2 \equiv e^{\nu(R)}\left(\dot{T}\dot{A}_2+h_2\dot{T}^2+\frac{1}{2}\frac{\partial \nu}{\partial R}B_2\dot{T}^2\right)-e^{\lambda(R)}\left(\dot{R}\dot{B}_2+j_2\dot{R}^2+\frac{1}{2}\frac{\partial \lambda}{\partial R}B_2\dot{R}^2\right). \tag{18}$$

In the above equations, we defined $[A]^{+}_{-} \doteq A^{+}|_{\Sigma}-A^{-}|_{\Sigma}$ as the *jump of A across* Σ. We stress that each of Equations (13) and (14) is two equations, related to each region ($\pm$) defined by Σ. We then have eight unknown functions, $(A^{\pm}_0, A^{\pm}_2, B^{\pm}_2, B^{\pm}_0)$, to seven equations, Equations (13)–(17). The missing equation is related to the freedom in deforming the shape of the surface, splitting the two glued regions of space for a fixed eccentricity. Note that $B^{\pm}_0=0$ (or any given constant) renders Equation (16) an identity, and in this case, we are left with a system of six equations to six variables. Equations (13)–(18) allow us to express the (continuous) induced metric on Σ in a simplified way, namely

$$\begin{aligned} ds^2_{\Sigma} &= d\tilde{\tau}^2\left[1+2\epsilon^2\{\alpha_2\}^{+}_{-}P_2(\cos\tilde{\theta})\right]-\left[R^2+2\epsilon^2 R\{B_0\}^{+}_{-}\right. \\ &+ \left.2\epsilon^2 R\{B_2+k_2R\}^{+}_{-}P_2(\cos\tilde{\theta})\right](d\tilde{\theta}^2+\sin\tilde{\theta}^2 d\tilde{\varphi}^2), \end{aligned} \tag{19}$$

where we define for a given quantity F on Σ, $\{F\}^{+}_{-} \equiv (F|_{\Sigma^+}+F|_{\Sigma^-})/2$. Of course, that simplified way of expressing the induced metric is due to our coordinate freedom on Σ.

We stress that all of our previous reasoning remains the same if we perform the change $P_2(\cos\theta) \to \mathcal{C}P_2(\cos\theta)$, with $\mathcal{C}$ an arbitrary constant. This is related to the freedom we always have in choosing the ellipticity of Σ when matching two slowly rotating spacetimes. In addition, $\tilde{\tau}$ is not the proper-time on Σ if one takes into account Equations (13)–(18). This is not a problem since the coordinates on Σ can be chosen freely. Finally, we recall that the thin-shell formalism leads to surface quantities that are independent of the coordinate systems of the glued spacetimes and the hypersurface. We chose Hartle's spacetime and y^a because, respectively, this is physically appealing and convenient for slowly rotating extended systems such as neutron stars, and this leads to a simple induced metric on Σ.

3. Static and Away-from-Equilibrium Thin Shells

We solved Equations (13)–(18) for the case Σ, which is not endowed with a dynamics, namely when $\dot{R} = 0$ or $R(\tau) = R$ = constant. This case is very important since it tests the consistency of the system of equations obtained previously. In addition, it gives us the requisites for having static glues of slowly rotating spacetimes. For this case, Equation (8) gives us that $\dot{T} = e^{-\frac{\nu}{2}}$. It is not difficult to show that the solution to the above system of equations is

$$\epsilon^2 B_2^+ = \frac{\epsilon_+^2 (h_2^+ + \frac{\partial \nu^-}{\partial R} k_2^+ R) - \epsilon_-^2 (h_2^- + \frac{\partial \nu^-}{\partial R} k_2^- R)}{\left[\frac{\partial \nu}{\partial R}\right]_-^+}, \tag{20}$$

$$\epsilon^2 B_2^- = \frac{\epsilon_+^2 (h_2^+ + \frac{\partial \nu^+}{\partial R} k_2^+ R) - \epsilon_-^2 (h_2^- + \frac{\partial \nu^+}{\partial R} k_2^- R)}{\left[\frac{\partial \nu}{\partial R}\right]_-^+}, \tag{21}$$

$$A_2^\pm = 0, \tag{22}$$

$$\epsilon^2 A_0^\pm = -\epsilon_\pm^2 \left(h_0^\pm + \frac{B_0^\pm}{2} \frac{\partial \nu^\pm}{\partial R} \right) e^{-\frac{\nu^\pm}{2}} \tilde{\tau}, \tag{23}$$

with B_0 a jump-free ($B_0^+ = B_0^-$) and arbitrary constant. In this case, the induced metric, Equation (19), does not depend on $\tilde{\tau}$, as expected. It can be checked that this is the only case where such an aspect rises concomitantly with the self-consistency of the system of equations. This justifies the choice of Equations (13)–(18).

It is worth emphasizing that $R(\tilde{\tau})$ = constant $\equiv R$ does not automatically guarantee the thin shell's stability upon perturbations. This is just the case whenever Σ is bound. From Equation (5), one sees that stability will be ensured just when both $R(\tilde{\tau})$ and $B(\tilde{\tau}, \tilde{\varphi})$ are bound functions. In particular, for our analysis to be meaningful, that should be fulfilled by the latter function. After meeting this demand, the only one left is the bound nature of $R(\tilde{\tau})$. This can be analyzed within the thin-shell formalism in the spherically symmetric case, and we know that it is summarized by the search of the minima of an effective potential [1]. As a result, in the stable case, $\dot{R}$ is automatically bound and could be approximated by a harmonic function around R with a very small amplitude. It is simple to show in this case that the corrections to Equations (20)–(23) coming from our field Equations (13)–(17) will also be proportional to oscillating functions around $r = R$. More specifically, if $\delta R \equiv R(\tilde{\tau}) - R = \mathcal{A}\cos(\tilde{\omega}\tilde{\tau})$, where $\mathcal{A}/R \ll 1$ and $\tilde{\omega}$ is a constant, then $\delta A_0 \propto \sin(\tilde{\omega}\tilde{\tau})$, $\delta A_2 \propto \sin(\tilde{\omega}\tilde{\tau})$, $\delta B_0 \propto \cos(\tilde{\omega}\tilde{\tau})$ and $\delta B_2 \propto \cos(\tilde{\omega}\tilde{\tau})$. This must be the case mathematically since we have a system of inhomogeneous trigonometric functions to solve. From Equations (5) and (6), it also makes physical sense that δA_0 and δA_2 (δB_0 and δB_2) oscillate in the same way. Thus, we concluded that the stability of Σ in the spherically symmetric case also implies its stability in the presence of small rotations. This is a very important result and will be used in subsequent sections when we elaborate on the energy conditions of hypersurfaces in the case of slow rotation.

4. Energy–Momentum Tensor for a Slowly Rotating Thin Shell

We now determine the energy–momentum tensor on Σ that guarantees the glue of two slowly rotating spacetimes whose boundary is dynamic. We must find the normal vector to Σ to do so. Generally, the normal vector to a given hypersurface Ψ is [18]

$$n_\mu \equiv \frac{\epsilon_n \partial_\mu \Psi}{|g^{\alpha\beta}\partial_\alpha \Psi \partial_\beta \Psi|^{\frac{1}{2}}}, \tag{24}$$

where $\epsilon_n = \pm 1$, depending on whether Σ is space-like or time-like, respectively. In addition, Equation (24) ensures that n_μ is a unit vector in the direction of growth of Σ.

Let us now calculate the gradient to Σ, $\partial_\mu \Psi$. From Equation (5),

$$\partial_\mu \Psi = \left(-\frac{1}{\dot{t}}[\dot{R} + \epsilon^2 \dot{B}], 1, -\frac{\partial B}{\partial \tilde{\theta}}, 0 \right). \tag{25}$$

From Equations (1), (6), (24) and (25), one obtains

$$n_0 = e^{\frac{\nu+\lambda}{2}} \dot{R} \left\{ 1 - \epsilon^2 \left[\frac{\dot{B}}{\dot{R}} + e^{\lambda} \dot{R}^2 \left(\frac{\dot{B}}{\dot{R}} - \frac{B}{2} \frac{\partial \nu}{\partial R} - h \right) - e^{\nu} \dot{T}^2 \left(\frac{\dot{A}}{\dot{T}} - \frac{B}{2} \frac{\partial \lambda}{\partial R} - j \right) \right] \right\}, \tag{26}$$

$$n_1 = -e^{\frac{\nu+\lambda}{2}} \dot{T} \left\{ 1 + \epsilon^2 \left[\frac{\dot{A}}{\dot{T}} + e^{\lambda} \dot{R}^2 \left(\frac{\dot{B}}{\dot{R}} - \frac{B}{2} \frac{\partial \nu}{\partial R} - h \right) - e^{\nu} \dot{T}^2 \left(\frac{\dot{A}}{\dot{T}} - \frac{B}{2} \frac{\partial \lambda}{\partial R} - j \right) \right] \right\}, \tag{27}$$

$$n_2 = e^{\frac{\nu+\lambda}{2}} \dot{T} \epsilon^2 \frac{\partial B}{\partial \tilde{\theta}}, \tag{28}$$

$$n_3 = 0. \tag{29}$$

In the above normal components, we assumed that Σ is time-like, thus $\epsilon_n = -1$ in Equation (24). The contravariant components of the normal vector can be worked out simply using $n^\mu = g^{\mu\nu} n_\nu$.

Now, we proceed with the calculations of the extrinsic curvature, defined as [18]

$$K_{ab} \equiv n_{\mu;\nu} \frac{\partial x^\mu}{\partial y^a} \frac{\partial x^\nu}{\partial y^b} = -n_\mu \left(\frac{\partial^2 x^\mu}{\partial y^a \partial y^b} + \Gamma^\mu_{\alpha\beta} \frac{\partial x^\alpha}{\partial y^a} \frac{\partial x^\beta}{\partial y^b} \right). \tag{30}$$

Off-diagonal terms in K_{ab} appear for slowly rotating spacetimes. First, we recall that, in the spherically symmetric case

$$K^0_0 = \frac{\nu'(e^{-\lambda} + \dot{R}^2) + 2\ddot{R} + \lambda' \dot{R}^2}{2\sqrt{e^{-\lambda} + \dot{R}^2}}, \tag{31}$$

and

$$K^1_1 = K^2_2 = \frac{\sqrt{e^{-\lambda} + \dot{R}^2}}{R}. \tag{32}$$

For the first-order corrections in "ϵ", we also have

$$K^0_2 = \frac{1}{2} \frac{\partial \omega}{\partial R} R^2 \sin^2 \tilde{\theta} e^{-\frac{\nu+\lambda}{2}} = -R^2 \sin^2 \tilde{\theta} K^2_0. \tag{33}$$

According to Lanczos' equation [16,17], the surface energy–momentum leading to a distributional solution to Einstein's equations is

$$8\pi S^a_b = [K^a_b]^+_- - \delta^a_b [K]^+_-, \tag{34}$$

where $K \doteq h^{ab} K_{ab}$ is the trace of the extrinsic curvature.

In the spherically symmetric (ss) case, S^a_b is a diagonal tensor concerning the $(\tilde{\tau}, \tilde{\theta}, \tilde{\varphi})$ coordinates, i.e.,

$$S^a_b = \frac{1}{8\pi} \mathrm{diag}(-2[K^1_1]^+_-, -[K^0_0 + K^1_1]^+_-, -[K^0_0 + K^1_1]^+_-) \equiv \mathrm{diag}(\sigma_{ss}, -\mathcal{P}_{ss}, -\mathcal{P}_{ss}). \tag{35}$$

This is the energy–momentum tensor for a comoving frame. Thus, the fluid on Σ is perfect-like, i.e.,

$$S^{ab} = \sigma_{ss} u^a u^b + \mathcal{P}_{ss} (u^a u^b - h^{ab}). \tag{36}$$

Whenever one works up to the first-order approximation in "ϵ", similar results as the above ones also hold in the coordinate system $(\tilde{\tau}, \tilde{\theta}, \tilde{\varphi})$, with $\tilde{\varphi}$ defined by Equation (6).

Now, we turn to the case where, up to second order, corrections in "ϵ" are worked out. From what we have pointed out previously, the form of the surface energy–momentum in this case in the coordinate system $(\tilde{\tau}, \tilde{\theta}, \tilde{\varphi})$ should generically resemble

$$S^a_b = \begin{bmatrix} S^0_0 + \epsilon^2 \bar{S}^0_0 & \epsilon^2 \bar{S}^0_1 & \epsilon \bar{S}^0_2 \\ \epsilon^2 \bar{S}^1_0 & S^1_1 + \epsilon^2 \bar{S}^1_1 & 0 \\ \epsilon \bar{S}^2_0 & 0 & S^1_1 + \epsilon^2 \bar{S}^2_2 \end{bmatrix}. \tag{37}$$

Because we are just inserting rotation into the problem, we still expect the fluid on Σ to be perfect-like. Thus, from Equation (36), we have that

$$S^a_b u^b = \sigma u^a. \tag{38}$$

The above equation shows that σ is invariant; hence, it will be the same for every coordinate system on Σ. The results coming from lower orders of approximation tell us that we should accept solutions of the form

$$u^a = [u_0 + \epsilon^2 \bar{u}_0, \epsilon^2 \bar{u}_1, \epsilon \bar{u}_2], \quad \text{and} \quad \sigma = \sigma_{ss} + \epsilon^2 \bar{\sigma}. \tag{39}$$

The only solution coming from Equation (38) that satisfies such prerequisites is

$$u^a = \left\{ 1 + \epsilon^2 \left[\frac{1}{2} \left(\frac{R \sin\tilde{\theta} \bar{S}^2_0}{S^0_0 - S^1_1} \right)^2 - \{\alpha_2\}^+_- P_2(\cos\tilde{\theta}) \right], \frac{\epsilon^2 \bar{S}^1_0}{S^0_0 - S^1_1}, \frac{\epsilon \bar{S}^2_0}{S^0_0 - S^1_1} \right\}, \tag{40}$$

where we fixed the arbitrary quantities u_0 and $\bar{u}_0$ coming from the eigenvalue approach by the normalization condition $u^a u_a = 1$ and

$$\sigma = S^0_0 + \epsilon^2 \left(\bar{S}^0_0 + \frac{\bar{S}^0_2 \bar{S}^2_0}{S^0_0 - S^1_1} \right). \tag{41}$$

For the (invariant) surface tension, from Equation (38), we generically have that

$$\mathcal{P} = \frac{1}{2} S^a_b (u^b u_a - \delta^b_a). \tag{42}$$

For the slowly rotating thin-shell case, the above equation becomes

$$\mathcal{P} = -S^1_1 + \epsilon^2 \left[-\frac{\bar{S}^1_1 + \bar{S}^2_2}{2} + \frac{\bar{S}^0_2 \bar{S}^2_0}{2(S^0_0 - S^1_1)} \right]. \tag{43}$$

Note that the second-order correction in "ϵ" to $\mathcal{P}$ is polar-angle-dependent, and it is different from the one to σ (see Equations (33), (34), (41) and (43)). We finally stress that our perturbative analyses break down whenever the surface quantities in the spherically symmetric are null. That is natural because we assumed that the slow-rotation case is only a small correction to the spherically symmetric case.

5. Dragging of Inertial Frames for Glued Slowly Rotating Spacetimes

We now briefly discuss some kinematic effects related to the match of two slowly rotating Hartle's spacetimes (see Equation (1)). Let us first analyze the aspects of a static observer inside the rotating thin shell. This observer can be described by $d\varphi^- = 0$ or from Equation (6) equivalently $d\tilde{\varphi} = -(\epsilon C)^- d\tilde{\tau}$. Thus, in the fixed stars' frame of reference (stationary observers at infinity), such an observer is rotating with the angular velocity:

$$\frac{d\varphi^+_{(d\varphi^-=0)}}{dt^+} = [(\epsilon C)^+ - (\epsilon C)^-] \frac{d\tilde{\tau}}{dt^+} = (\epsilon\omega)^+ - \frac{(\epsilon\omega \dot{T})^-}{\dot{T}^+}, \tag{44}$$

where we also used Equation (7). We recall that $\dot{T}^{\pm}$ can easily be read off from Equation (8). Equation (44) states that, far away external observers see internal ones rotating, even when $\epsilon^{-} = 0$, namely when the inner spacetime is spherically symmetric. Such an effect is the well-known dragging of inertial frames, or the Lense–Thirring effect [21]. The case where $\epsilon^{-} = 0$ is interesting because it shows that the rotation of the shell intrinsically induces a rotation of the observers inside it. Whenever the inner spacetime is also endowed with a rotational parameter ($\epsilon^{-} \neq 0$), naturally, it also contributes to the final angular velocity fixed stars ascribe to internal observers at rest, as evidenced by Equation (44). Even more remarkable in this case is the possibility of the disappearance of the dragging of inertial frames (see Equation (44)). This is so even when $\epsilon^{\pm}$ and the shell parameters are given by convenient values of the inner spacetime parameters.

Furthermore, about distant observers, the rotation of the thin shell can be obtained. We know that concerning the frame with coordinates $(\tilde{\tau}, \tilde{\theta}, \tilde{\varphi})$, the shell rotates with angular velocity

$$\frac{d\tilde{\varphi}}{d\tilde{\tau}} = \frac{\epsilon \bar{S}_0^2}{S_0^0 - S_1^1}, \tag{45}$$

where we recall that the "ϵ" dependence on Equation (40) is merely an indicator that the associated surface energy–momentum tensor is of a given order on the rotational parameters $\epsilon^{\pm}$. Taking into account Equations (6) and (45), we have that the angular velocity of the shell relative to the fixed stars is

$$\frac{d\varphi_{\Sigma}^{+}}{dt^{+}} = \frac{d\tilde{\varphi}}{dt^{+}} + \epsilon^{+} C^{+} \frac{d\tilde{\tau}}{dt^{+}} = \frac{\epsilon \bar{S}_0^2}{(S_0^0 - S_1^1)\dot{T}^{+}} + (\epsilon\omega)^{+}, \tag{46}$$

where also Equation (7) was taken into account, and we recall that $\dot{T}$ is given by Equation (8). For completeness, we remark that the relative velocity of observers inside the shell with the shell itself could be obtained by Equations (44) and (46) and always vanishes at the associated "gravitational radius" of the external spacetime ($e^{\nu_{+}} = 0$), showing that rigid dragging takes place in this case [3]. Nevertheless, whenever a nontrivial inner spacetime is considered, in principle, configurations always exist that would lead the observers inside the shell to corotate with the thin shell. The interest in the effect of frame dragging [22,23] naturally lies in the fact that its measurement could give direct information about the stratification of spacetime.

6. Matching Slowly Rotating Kerr Spacetimes

A case of physical interest concerning the glue of slowly rotating spacetimes would be where they are of Kerr types. This could be, for instance, a model for slowly rotating neutral thin shells of matter collapsing onto Kerr black holes as could happen in AGNs. A natural advantage of this match is the geometric simplicity of both regions. We know that the Kerr metric in the Boyer–Lindquist coordinates $(\bar{t}, \bar{r}, \bar{\theta}, \bar{\varphi})$ is [21]

$$ds^2 = \left(1 - \frac{2M\bar{r}}{\rho^2}\right) d\bar{t}^2 - \frac{4M\bar{r}a\sin^2\bar{\theta}}{\rho^2} d\bar{t}d\bar{\varphi} - \frac{\rho^2}{\Delta} d\bar{r}^2 - \rho^2 d\bar{\theta}^2 - \frac{\Upsilon}{\rho^2}\sin^2\bar{\theta} d\bar{\varphi}^2, \tag{47}$$

where

$$\Delta \equiv \bar{r}^2 - 2M\bar{r} + a^2, \tag{48}$$

$$\Upsilon \equiv (\bar{r}^2 + a^2)^2 - \Delta a^2 \sin^2\bar{\theta}, \tag{49}$$

$$\rho^2 \equiv \bar{r}^2 + a^2\cos^2\bar{\theta}. \tag{50}$$

This solution has two arbitrary constants: the system's total mass, M, and its total angular momentum per unit mass, a. The above metric has horizons at $\Delta = 0$. We shall not elaborate anymore on the well-known properties of this solution.

We emphasize that Hartle's coordinates (t, r, θ, φ) differ from the Boyer–Lindquist ones. It is simple, though tedious, to show that the coordinate transformations linking the aforesaid coordinate systems up to second order in "ϵ" (here, $\epsilon = a/r$) are (see, e.g., Beltracchi et al. [12])

$$\bar{\theta} = \theta - \frac{a^2}{2r^2}\left(1 + \frac{2M}{r}\right)\cos\theta\sin\theta, \tag{51}$$

$$\bar{r} = r - \frac{a^2}{2r}\left[\left(1 + \frac{2M}{r}\right)\left(1 - \frac{M}{r}\right) - \left(1 - \frac{2M}{r}\right)\left(1 + \frac{3M}{r}\right)\cos^2\theta\right]. \tag{52}$$

The coordinate transformations given by Equations (51) and (52) are necessary to apply the formalism we developed previously for matching two slowly rotating spacetimes. The Kerr metric components up to second order in "ϵ" in Hartle's coordinates are

$$h_0^K(r) = \frac{M^2}{r^2}e^{-\nu}, \tag{53}$$

$$h_2^K(r) = \frac{M}{r^3}(r - 2M)(M + r)e^{-\nu}, \tag{54}$$

$$j_0^K(r) = -\frac{M^2}{(r - 2M)^2}e^{\nu}, \tag{55}$$

$$j_2^K(r) = \frac{M(5M - r)}{r(r - 2M)}e^{\nu}, \tag{56}$$

$$k_2^K(r) = -\frac{M(2M + r)}{r^2}, \tag{57}$$

and

$$e^{\nu} = 1 - \frac{2M}{r}, \tag{58}$$

$$\omega = \frac{2M}{r^2}. \tag{59}$$

We now investigate the induced shell quantities (surface energy density and tension) due to small rotations. For example, let us choose thin shells in equilibrium at the radial coordinate $R = 5M_+$, M_+ being the mass of the outer Schwarzschild spacetime seed. This analysis is interesting since test particles cannot be in stable equilibrium for $r < 6M_+$ in a Schwarzschild spacetime, unlike thin shells (which renders them special and shows the importance of searching for distributional solutions in general relativity). In addition, it would allow us to probe thin shells in strong gravitational fields, as motivated by inner accretion discs in AGNs [24] or even in stratified neutron stars. In what follows, for numerical convenience, we take $a_- = na_+$ and $M_- = mM_+$, with $(n, m) \in (\Re, \Re^+)$, respectively. As expected, for two Schwarzschild spacetimes, when $M_+ > M_-$, all induced surface quantities are positive [1].

We must also choose other parameters related to the glued thin shells to proceed. Our analysis in Section 3 concluded that shells in equilibrium could be characterized by an arbitrary jump-free constant $\epsilon^2 B_0$, related to the effective change of radius from R due to rotation. We chose for our investigations the case where $B_0 = 0$. The reasons for that were mainly connected with its physical reasonableness. One can verify that the glue of two Kerr spacetimes at $R = 5M_+$ is such that, for reasonable n (such as $-1 < n < 1$) and $m < 1$, one has that $B(\theta = 0) < 0$ and $B(\theta = \pi/2) > 0$, meaning that the resultant surface is flattened in the poles and stretched in the equator with respect to a sphere, as one expects physically when rotation takes place. Situations where $B_0 \neq 0$ are left to be investigated elsewhere.

As we have shown previously, the stability analyses of slowly rotating thin shells (around given radial positions) can be summarized by their spherically symmetric counterparts (see Section 3). Therefore, we should analyze the stability of glued Schwarzschild

spacetimes to investigate slowly rotating Kerr spacetimes. It is known in this case that a thin shell is stable at $r = R$ *iff* its associated effective potential [1]:

$$V(R) \equiv \frac{1}{2}(e^{-\lambda_-} + e^{-\lambda_+}) - \frac{1}{4}(4\pi R\sigma_{ss})^2 - \frac{1}{4}\left(\frac{[e^{-\lambda}]^+_-}{4\pi R\sigma_{ss}}\right)^2 \tag{60}$$

has a minimum there ($d^2V/dR^2 > 0$). It can be shown that [20]

$$\frac{d^2V}{dR^2} = -\frac{\left[e^{-\frac{\lambda}{2}}\left\{(2\eta+1)\left(1+\frac{R}{2}\lambda'\right) - \frac{R^2}{2}\left(\nu'' - \frac{1}{2}\lambda'\nu'\right)\right\}\right]^+_-}{R^2[e^{\frac{\lambda}{2}}]^+_-}, \tag{61}$$

where η is defined as the adiabatic speed of sound squared on the shell [20], i.e., $\eta \equiv c_s^2$. We stress that, for the thin shell formalism to make sense, $\sigma_{ss} \neq 0$, which we took in our analysis. That also justified the perturbative treatment with respect to the spherically symmetric case in the previous sections.

Figure 1 shows the stability condition ($R^2 d^2V/dR^2 > 0$) for several matches of Schwarzschild spacetimes with masses leading to $\sigma_{ss} > 0$ at $R = 5M_+$. One sees from the aforementioned plot that thin shells are stable for most η and internal-to-external mass ratios. This suggests that $r = 5M_+$ is a feasible choice for the equilibrium radius of a thin shell with nontrivial surface degrees of freedom.

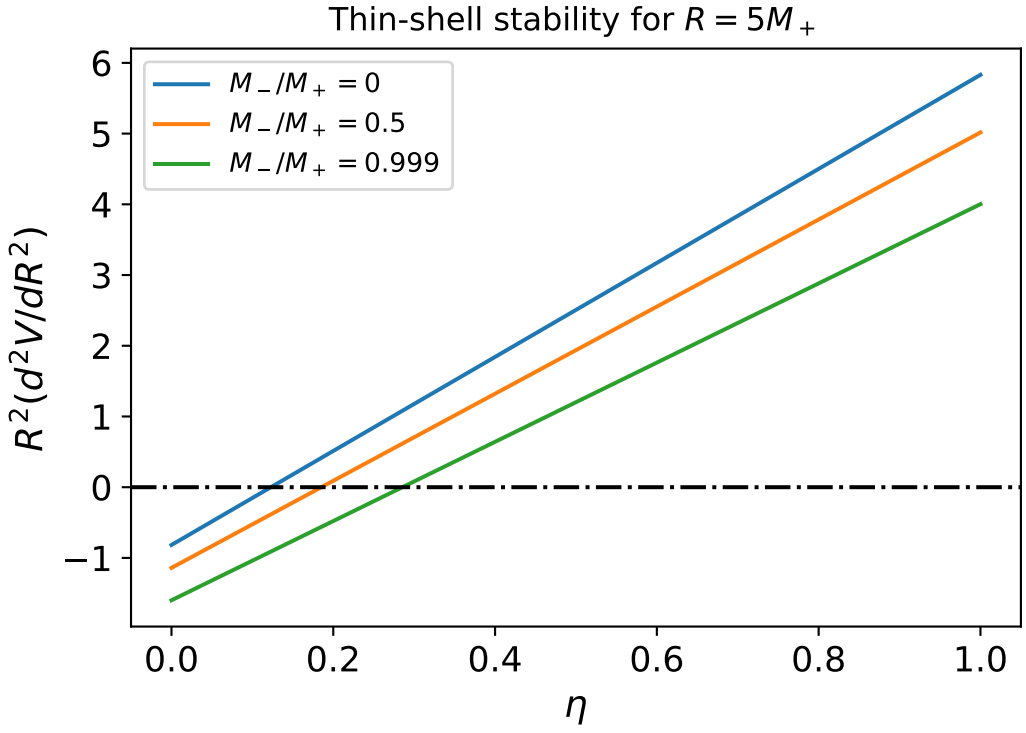

Figure 1. Thin-shell stability for some glues of Schwarzschild spacetimes where the outer masses are always larger than the inner ones, leading to $\sigma_{ss} > 0$ and $\mathcal{P}_{ss} > 0$. The equilibrium radius is taken as $R = 5M_+$ for all cases. For Schwarszchild spacetimes, the quantity of relevance is R/M_+, and M_+ could be any. In particular, when $R/M_+ = 5$, several thin shells' speed of sound lead to stable equilibria. That is the case even for very small thin-shell masses ($M_-/M_+ \sim 1$). For the case $M_-/M_+ = 0.999$, any $\eta \gtrsim 0.3$ will fulfill the stability condition.

We studied induced surface quantities on slowly rotating neutral thin shells in slowly rotating Kerr spacetimes. Figure 2 shows the relative changes for the surface energy densities ($\Delta\sigma/\sigma$) for some selected Schwarzschild seeds. For all polar angles, they decrease

when compared to their spherically symmetric counterparts. That is the case if the inner spacetime counter-rotates with respect to the outer one (because $\Delta\sigma$'s with positive and negative n do not differ much), if it has no rotation at all ($n = 0$) or if it has the same rotation as the external one ($n = 1$). That is the same concerning relative changes of the relative surface tension $\Delta\mathcal{P}/\mathcal{P} \equiv \mathcal{P}/\mathcal{P}_{ss} - 1$ (see Figure 3).

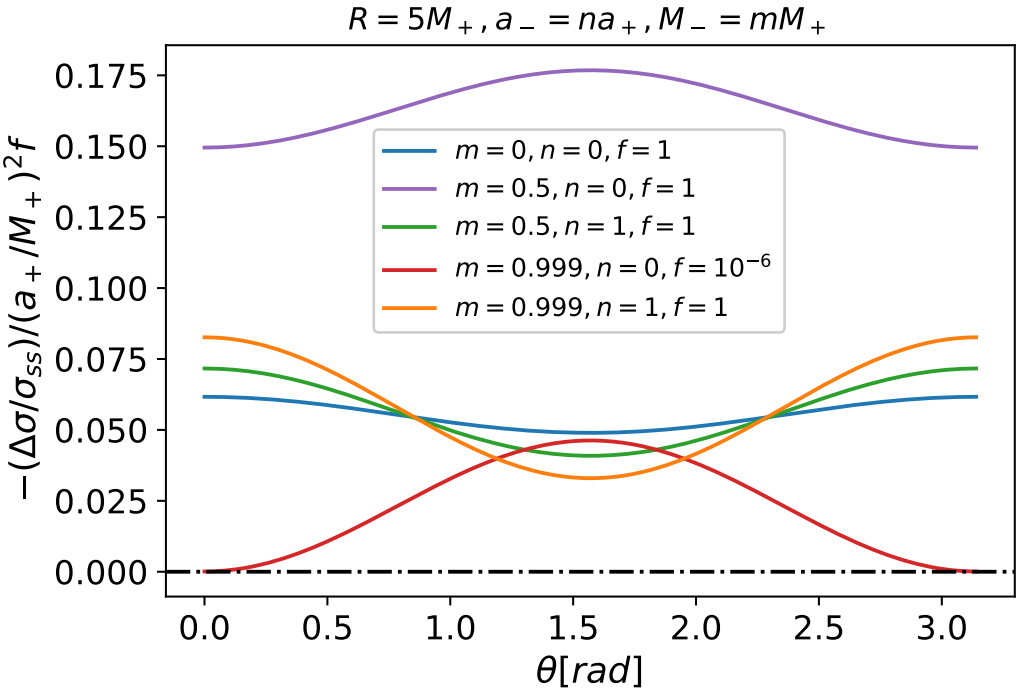

Figure 2. Relative surface energy density corrections due to rotation ($\Delta\sigma/\sigma_{ss} \equiv \sigma/\sigma_{ss} - 1$) for some parameters of the glued spacetimes. Internal and external mass ratios were chosen to coincide with those of Figure 2. To be more general, we did not specify the particular rotational parameter $(a_+/M_+)^2$; we just assumed it was small. The factor "f" is only for convenience (plotting all the cases in a similar scale). Negative n's lead to the same results as their positive counterparts. Note that, for all the cases and polar angles, $\Delta\sigma < 0$, meaning that rotation decreases the local surface energy density on the thin shell.

For all the cases in Figure 1, it is simple to verify that the weak, null, strong, and dominant energy conditions [18] are satisfied. This shows the reasonableness of our assumptions. In the presence of rotation, the aforesaid conditions are slightly weakened. Figure 4 exemplifies the previous statement due to the negativity of the induced part of the strong energy condition ($\Delta\sigma + 2\Delta\mathcal{P} < 0$) for the spacetime matches in Figure 1. Similar conclusions could be reached for the weakening of other energy conditions (weak and null) because both $\Delta\sigma$ and $\Delta\mathcal{P}$ are negative. Naturally, in the perturbative scope, this does not mean any violation of the energy conditions, but only their weakening when small rotations are present, which suggests nontrivial behavior in the non-perturbative case.

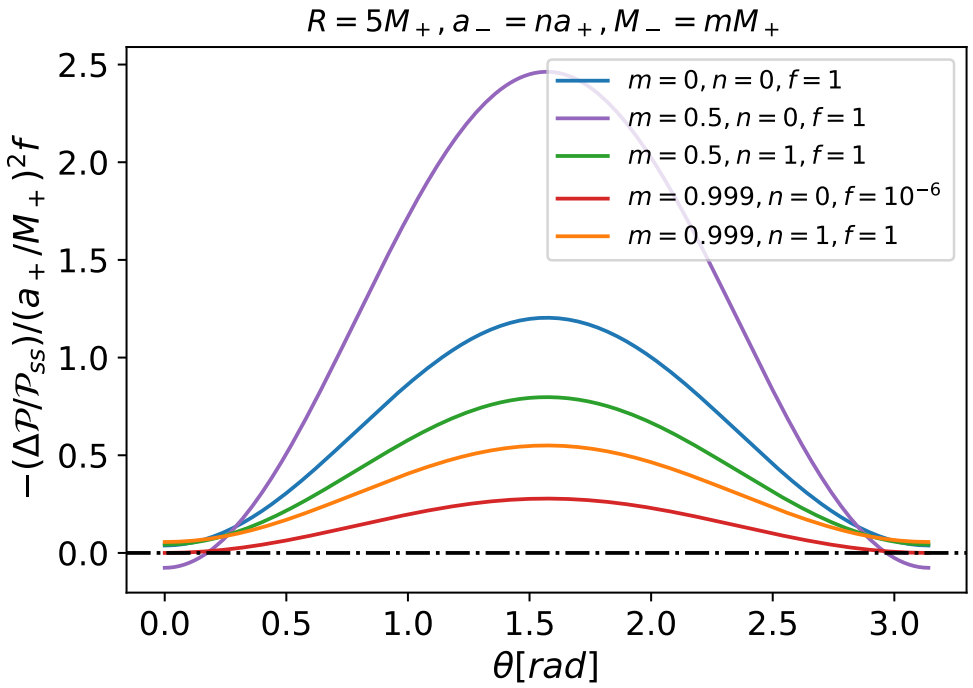

Figure 3. Relative induced surface tension ($\Delta\mathcal{P}/\mathcal{P}_{ss} \equiv \mathcal{P}/\mathcal{P}_{ss} - 1$) as a function of the polar angle θ. We chose the same mass ratios of Figure 2. Note that, for almost all choices of thin-shell mass and polar angles, the surface tension correction to the spherically symmetric case due to rotation is negative.

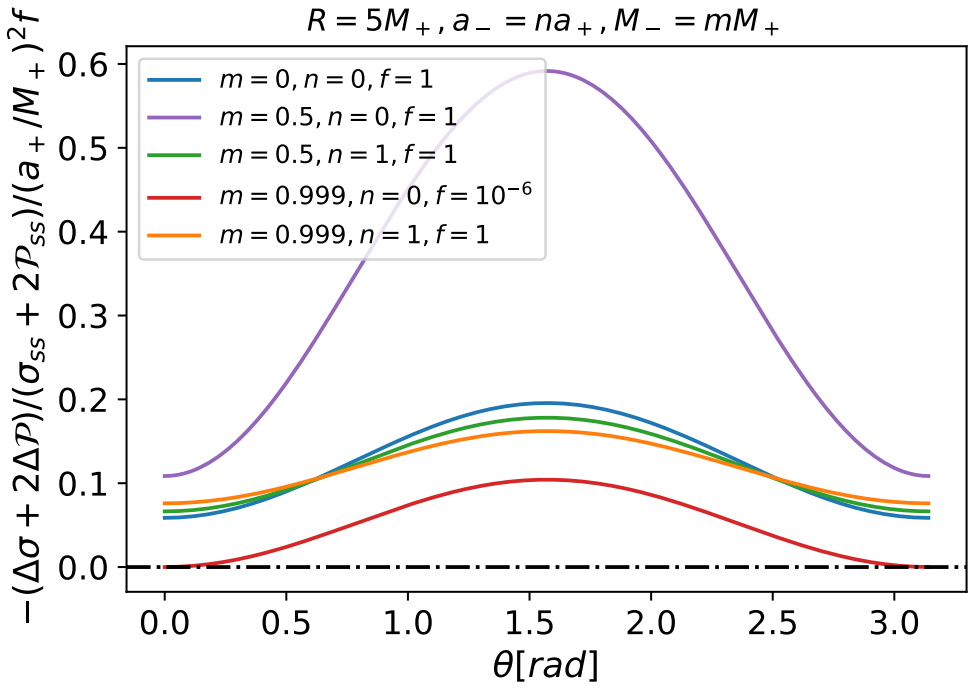

Figure 4. The parameters for the curves are the same as their counterparts in Figure 2. The induced part due to the rotation in the strong energy condition ($\Delta\sigma + 2\Delta\mathcal{P}$) is negative (clearly not the case for the selected values of the glued spacetimes, whose spherically symmetric counterparts satisfy all energy conditions), which points to the possibility of the non-validity of some energy conditions in non-perturbative analyses.

7. Concluding Remarks

This work showed the subtleties and nontrivialities in matching two slowly rotating Hartle's spacetimes through dynamic hypersurfaces. For a given matching hypersurface, we obtained generically that its equilibrium points are stable if their spherically symmetric counterparts are so. Concerning the kinematical effects, we showed that it is possible to match spacetimes where a rigid-rotation behavior appears—at least in some limit—and the frame-dragging effect can give information about the matched spacetimes. We also found that the thin shells' surface energy densities and surface tensions decrease compared to their spherical counterparts. This suggests, for instance, that the assumption of having everywhere-positive surface degrees of freedom may be broken in non-perturbative calculations. Energy conditions may also be violated in this scenario, which could have important consequences (for the relevance of the energy conditions in general relativity, see Chapter 34 of [21,25]). Another possibility would be that the possible violation of the energy conditions would preclude the existence of such thin-shell structures. Given its importance, we plan to investigate that better elsewhere.

Let us elaborate on some of the above points. The automatic stability of a slowly rotating thin shell, when its spherically symmetric seed is stable, is reasonable because a slowly rotating spacetime and thin shell perturbations there can be roughly seen as effective thin-shell perturbations in the spherical case. The fact that this stability emerges from our system of equations when matching two slowly rotating spacetimes is also relevant because it strengthens its consistency and it shows that, when the thin shell stability is concerned, it suffices to analyze just the spherically symmetric case. On the other hand, the decrease in the value of surface quantities when the slow rotation is present (as was clear when matching two Kerr spacetimes) is not trivial. A possible interpretation of it is that part of the thin-shell energy goes into rotational energy. That would reinforce the need, in general, to go beyond the slow rotation approximation we adopted. Clearly, this is not an easy task because some symmetries of the spacetimes to be matched are lost. However, it is worth mentioning that, for instance, in the case of rotating neutron stars, deviations from the spherical symmetry are essentially negligible for rotation rates of up to a few hundred Hz (see, e.g., [26,27]). Thus, we expect the slow-rotation Hartle spacetime metric to be a reasonable approximation for those configurations. Finally, Figures 3 and 4 also show that the largest relative differences for the surface tension and surface energy density when m is not too close to unity happen when the internal spacetime is flat (i.e., Minkowski). The reason here is that this case leads to the largest mass–energy content of the thin shell. Thus, one would also expect that their relative differences would be maximized with respect to other cases where the internal spacetime has mass and rotation. The results for m close to one should be taken with a grain of salt because the perturbative model investigated breaks down when $m = 1$ (no surface degrees of freedom are induced in the background spacetime).

One could apply the thin shell formalism developed here for cases involving astrophysical black holes, which are believed to be of the Kerr type. That could be for those at the centers of galaxies, such as AGNs, or even those in binaries or alone. The idea is that structures (thin shells) could be formed around black holes, wrapping them up totally or partially. For the case of black holes with masses ranging from one to two solar masses and thin shells with a (small) fraction of that mass, if their equilibrium position is $R = 4$–$6M_+$, then R is of the order of a neutron star's radius ($\approx$12 km for a 1.4 $M_\odot$ star [28,29]). The intriguing question is whether external observers could perceive those thin shells as neutron stars. If, instead, BHs of around a solar mass are wrapped up by thin shells and equilibrium radii around $R = (10^3$–$10^4)M_+$, one could perceive them as white dwarfs. In the era of gravitational-wave astronomy, these possibilities seem interesting to be better investigated because the above equilibrium radii are stable for a large range of sound speeds on the thin shells. Some gravitational-wave aspects are already known for some exotic compact objects (see, e.g., [9,11,30–37]).

Another special arena of application of this work is stratified compact stars, which have in their interiors a huge range of densities and pressures and even different matter phases (e.g., solid and liquid hadronic phases [38] or possibly even the quark and hadronic phases of hybrid stars [39]). Slow rotation would be the natural extension of the spherically symmetric case, where the stability formalism for stratified stars is already known [40] and surface degrees of freedom can be induced upon perturbations [41]. The approach presented here can be applied to the match of various matter phases since the second-order slow rotation approximation is accurate for the description of uniformly rotating neutron stars up to frequencies ∼300 Hz (see, e.g., References [26,42]). In this line, comparing and contrasting the stability when a thin shell matches different phases for static and rotating configurations seem relevant. The formalism could also be applied if the surface of a neutron star is buried with a thin layer of supernova debris (e.g., as the so-called central compact objects (CCOs) [43–45]). In addition, one could check whether or not the stringent stability of strange quark stars with an outer crust obtained in [20] changes when adding rotation. The case of neutron stars rotating in the kHz region needs the non-perturbative solution of the match of axially symmetric spacetimes, which represents the ultimate goal of the analysis proposed in this work.

Author Contributions: Conceptualization, J.P.P. and J.A.R.; numerical analysis, J.P.P.; formal analysis. J.P.P. and J.A.R.; writing—original draft preparation, J.P.P. and J.A.R. All authors have read and agreed to the published version of the manuscript.

Funding: This research was funded by Fundação do Estado do Espírito Santo (FAPES), Grant Number 04/2022.

Data Availability Statement: No new data were created.

Acknowledgments: We are grateful to Jaziel G. Coelho for useful comments, which helped us improve the work.

Conflicts of Interest: The authors declare no conflict of interest.

References

1. Lobo, F.S.N.; Crawford, P. Stability analysis of dynamic thin shells. *Class. Quantum Gravity* **2005**, *22*, 4869–4885.
2. Musgrave, P.; Lake, K. Junctions and thin shells in general relativity using computer algebra: I. The Darmois—Israel formalism. *Class. Quantum Gravity* **1996**, *13*, 1885–1899.
3. De La Cruz, V.; Israel, W. Spinning Shell as a Source of the Kerr Metric. *Phys. Rev.* **1968**, *170*, 1187–1192. [CrossRef]
4. Kegeles, L.S. Collapse to a rotating black hole. *Phys. Rev. D* **1978**, *18*, 1020–1029. [CrossRef]
5. Uchikata, N.; Yoshida, S. Slowly rotating regular black holes with a charged thin shell. *Phys. Rev. D* **2014**, *90*, 064042. [CrossRef]
6. Pfister, H.; Braun, K.H. A mass shell with flat interior cannot rotate rigidly. *Class. Quantum Gravity* **1986**, *3*, 335–345. [CrossRef]
7. Orwig, L.P. Machian effects in compact, rapidly spinning shells. *Phys. Rev. D* **1978**, *18*, 1757–1763. [CrossRef]
8. Mendes, R.F.P.; Matsas, G.E.A.; Vanzella, D.A.T. Instability of nonminimally coupled scalar fields in the spacetime of slowly rotating compact objects. *Phys. Rev. D* **2014**, *90*, 044053.
9. Pani, P. I-Love-Q relations for gravastars and the approach to the black-hole limit. *Phys. Rev. D* **2015**, *92*, 124030.
10. Uchikata, N.; Yoshida, S. Slowly rotating thin shell gravastars. *Class. Quantum Gravity* **2016**, *33*, 025005.
11. Uchikata, N.; Yoshida, S.; Pani, P. Tidal deformability and I-Love-Q relations for gravastars with polytropic thin shells. *Phys. Rev. D* **2016**, *94*, 064015.
12. Beltracchi, P.; Gondolo, P.; Mottola, E. Slowly rotating gravastars. *Phys. Rev. D* **2022**, *105*, 024002.
13. Agrawal, A.S.; Mishra, B.; Tello-Ortiz, F.; Alvarez, A. f(R)f(R) Wormholes Embedded in a Pseudo–Euclidean Space E 5. *Fortschritte Der Phys.* **2022**, *70*, 2100177.
14. Tello-Ortiz, F.; Mishra, B.; Alvarez, A.; Singh, K.N. Minimally Deformed Wormholes Inspired by Noncommutative Geometry. *Fortschritte Der Phys.* **2023**, *71*, 2200108.
15. Hartle, J.B. Slowly Rotating Relativistic Stars. I. Equations of Structure. *Astrophys. J.* **1967**, *150*, 1005. [CrossRef]
16. Lanczos, K. Flächenhafte Verteilung der Materie in der Einsteinschen Gravitationstheorie. *Ann. Der Phys.* **1924**, *379*, 518–540. [CrossRef]
17. Israel, W. Singular hypersurfaces and thin shells in general relativity. *Nuovo C. B Ser.* **1966**, *44*, 1–14. [CrossRef]
18. Poisson, E. *A Relativist's Toolkit: The Mathematics of Black-Hole Mechanics*; Cambridge University Press: Cambridge, UK, 2004.
19. Eiroa, E.F.; Simeone, C. Stability of charged thin shells. *Phys. Rev. D* **2011**, *83*, 104009.
20. Pereira, J.P.; Coelho, J.G.; Rueda, J.A. Stability of thin-shell interfaces inside compact stars. *Phys. Rev. D* **2014**, *90*, 123011. [CrossRef]

21. Misner, C.W.; Thorne, K.S.; Wheeler, J.A. *Gravitation*; W.H. Freeman and Co.: San Francisco, CA, USA, 1973.
22. Everitt, C.W.F.; Debra, D.B.; Parkinson, B.W.; Turneaure, J.P.; Conklin, J.W.; Heifetz, M.I.; Keiser, G.M.; Silbergleit, A.S.; Holmes, T.; Kolodziejczak, J.; et al. Gravity Probe B: Final Results of a Space Experiment to Test General Relativity. *Phys. Rev. Lett.* **2011**, *106*, 221101.
23. Venkatraman Krishnan, V.; Bailes, M.; van Straten, W.; Wex, N.; Freire, P.C.C.; Keane, E.F.; Tauris, T.M.; Rosado, P.A.; Bhat, N.D.R.; Flynn, C.; et al. Lense-Thirring frame dragging induced by a fast-rotating white dwarf in a binary pulsar system. *Science* **2020**, *367*, 577–580.
24. Fabian, A.C.; Wilkins, D.R.; Miller, J.M.; Reis, R.C.; Reynolds, C.S.; Cackett, E.M.; Nowak, M.A.; Pooley, G.G.; Pottschmidt, K.; Sanders, J.S.; et al. On the determination of the spin of the black hole in Cyg X-1 from X-ray reflection spectra. *MNRAS* **2012**, *424*, 217–223.
25. Kontou, E.A.; Sanders, K. Energy conditions in general relativity and quantum field theory. *Class. Quantum Gravity* **2020**, *37*, 193001.
26. Belvedere, R.; Boshkayev, K.; Rueda, J.A.; Ruffini, R. Uniformly rotating neutron stars in the global and local charge neutrality cases. *Nucl. Phys. A* **2014**, *921*, 33–59.
27. Cipolletta, F.; Cherubini, C.; Filippi, S.; Rueda, J.A.; Ruffini, R. Fast rotating neutron stars with realistic nuclear matter equation of state. *Phys. Rev. D* **2015**, *92*, 023007. [CrossRef]
28. Riley, T.E.; Watts, A.L.; Bogdanov, S.; Ray, P.S.; Ludlam, R.M.; Guillot, S.; Arzoumanian, Z.; Baker, C.L.; Bilous, A.V.; Chakrabarty, D.; et al. A NICER View of PSR J0030+0451: Millisecond Pulsar Parameter Estimation. *Astrophys. J. Lett.* **2019**, *887*, L21.
29. Miller, M.C.; Lamb, F.K.; Dittmann, A.J.; Bogdanov, S.; Arzoumanian, Z.; Gendreau, K.C.; Guillot, S.; Harding, A.K.; Ho, W.C.G.; Lattimer, J.M.; et al. PSR J0030+0451 Mass and Radius from NICER Data and Implications for the Properties of Neutron Star Matter. *Astrophys. J. Lett.* **2019**, *887*, L24.
30. Maselli, A.; Pnigouras, P.; Nielsen, N.G.; Kouvaris, C.; Kokkotas, K.D. Dark stars: Gravitational and electromagnetic observables. *Phys. Rev. D* **2017**, *96*, 023005.
31. Cardoso, V.; Franzin, E.; Maselli, A.; Pani, P.; Raposo, G. Testing strong-field gravity with tidal Love numbers. *Phys. Rev. D* **2017**, *95*, 084014.
32. Raposo, G.; Pani, P.; Emparan, R. Exotic compact objects with soft hair. *Phys. Rev. D* **2019**, *99*, 104050.
33. Maselli, A.; Pani, P.; Cardoso, V.; Abdelsalhin, T.; Gualtieri, L.; Ferrari, V. Probing Planckian Corrections at the Horizon Scale with LISA Binaries. *Phys. Rev. Lett.* **2018**, *120*, 081101.
34. Cardoso, V.; Pani, P. Testing the nature of dark compact objects: A status report. *Living Rev. Relativ.* **2019**, *22*, 4.
35. Johnson-McDaniel, N.K.; Mukherjee, A.; Kashyap, R.; Ajith, P.; Del Pozzo, W.; Vitale, S. Constraining black hole mimickers with gravitational wave observations. *Phys. Rev. D* **2020**, *102*, 123010.
36. Narikawa, T.; Uchikata, N.; Tanaka, T. Gravitational-wave constraints on the GWTC-2 events by measuring the tidal deformability and the spin-induced quadrupole moment. *Phys. Rev. D* **2021**, *104*, 084056.
37. Maggio, E.; Pani, P.; Raposo, G. Testing the Nature of Dark Compact Objects with Gravitational Waves. In *Handbook of Gravitational Wave Astronomy*; Springer: Singapore, 2021; p. 29. [CrossRef]
38. Haensel, P.; Potekhin, A.Y.; Yakovlev, D.G. *Neutron Stars 1: Equation of State and Structure*; Springer: New York, NY, USA, 2007; Volume 326, pp. 1–619. [CrossRef]
39. Pereira, J.P.; Flores, C.V.; Lugones, G. Phase Transition Effects on the Dynamical Stability of Hybrid Neutron Stars. *Astrophys. J.* **2018**, *860*, 12.
40. Pereira, J.P.; Rueda, J.A. Radial Stability in Stratified Stars. *Astrophys. J.* **2015**, *801*, 19.
41. Pereira, J.P.; Lugones, G. General Relativistic Surface Degrees of Freedom in Perturbed Hybrid Stars. *Astrophys. J.* **2019**, *871*, 47.
42. Benhar, O.; Ferrari, V.; Gualtieri, L.; Marassi, S. Perturbative approach to the structure of rapidly rotating neutron stars. *Phys. Rev. D* **2005**, *72*, 044028.
43. Ho, W.C.G. Evolution of a buried magnetic field in the central compact object neutron stars. *MNRAS* **2011**, *414*, 2567–2575.
44. Viganò, D.; Pons, J.A. Central compact objects and the hidden magnetic field scenario. *MNRAS* **2012**, *425*, 2487–2492.
45. De Luca, A. Central compact objects in supernova remnants. *J. Phys. Conf. Ser.* **2017**, *932*, 012006.

The Astrophysical Journal, 945:95 (14pp), 2023 March 10 https://doi.org/10.3847/1538-4357/acb771

GRB 171205A: Hypernova and Newborn Neutron Star

Yu Wang[1,2,3], L. M. Becerra[2,4], C. L. Fryer[5,6,7,8,9], J. A. Rueda[1,2,10,11,12], and R. Ruffini[1,2,13]
[1] ICRA, Dipartimento di Fisica, Università di Roma "La Sapienza", Piazzale Aldo Moro 5, I-00185 Roma, Italy; yu.wang@inaf.it, laura.marcela.becerra@gmail.com, fryer@lanl.gov
[2] ICRANet, Piazza della Repubblica 10, I-65122 Pescara, Italy; jorge.rueda@icra.it
[3] INAF–Osservatorio Astronomico d'Abruzzo, Via M. Maggini snc, I-64100, Teramo, Italy; ruffini@icra.it
[4] Escuela de Física, Universidad Industrial de Santander, A.A.678, Bucaramanga, 680002, Colombia
[5] Center for Theoretical Astrophysics, Los Alamos National Laboratory, Los Alamos, NM, 87545, USA
[6] Computer, Computational, and Statistical Sciences Division, Los Alamos National Laboratory, Los Alamos, NM, 87545, USA
[7] The University of Arizona, Tucson, AZ 85721, USA
[8] Department of Physics and Astronomy, The University of New Mexico, Albuquerque, NM 87131, USA
[9] The George Washington University, Washington, DC 20052, USA
[10] ICRANet-Ferrara, Dipartimento di Fisica e Scienze della Terra, Università degli Studi di Ferrara, Via Saragat 1, I-44122 Ferrara, Italy
[11] Dipartimento di Fisica e Scienze della Terra, Università degli Studi di Ferrara, Via Saragat 1, I-44122 Ferrara, Italy
[12] INAF–Istituto di Astrofisica e Planetologia Spaziali, Via Fosso del Cavaliere 100, I-00133 Rome, Italy
[13] INAF, Viale del Parco Mellini 84, I-00136 Rome, Italy
Received 2022 August 4; revised 2023 January 9; accepted 2023 January 29; published 2023 March 9

Abstract

GRB 171205A is a low-luminosity, long-duration gamma-ray burst (GRB) associated with SN 2017iuk, a broad-line type Ic supernova (SN). It is consistent with having been formed in the core collapse of a widely separated binary, which we have called the binary-driven hypernova of type III. The core collapse of the CO star forms a newborn NS (νNS) and the SN explosion. Fallback accretion transfers mass and angular momentum to the νNS, here assumed to be born non-rotating. The accretion energy injected into the expanding stellar layers powers the prompt emission. The multiwavelength power-law afterglow is explained by the synchrotron radiation of electrons in the SN ejecta, powered by energy injected by the spinning νNS. We calculate the amount of mass and angular momentum gained by the νNS, as well as the νNS rotational evolution. The νNS spins up to a period of 47 ms, then releases its rotational energy powering the synchrotron emission of the afterglow. The paucity of the νNS spin explains the low-luminosity characteristic and that the optical emission of the SN from the nickel radioactive decay outshines the optical emission from the synchrotron radiation. From the νNS evolution, we infer that the SN explosion had to occur at most 7.36 h before the GRB trigger. Therefore, for the first time, the analysis of the GRB data leads to the time of occurrence of the CO core collapse leading to the SN explosion and the electromagnetic emission of the GRB event.

Unified Astronomy Thesaurus concepts: Gamma-ray bursts (629); Neutron stars (1108); Pulsars (1306)

1. Introduction

The Burst Alert Telescope of the Neil Gehrels Swift Observatory on board (Swift-BAT) triggered and located GRB 171205A at 07:20:43 UT on 2017 December 17. Swift's X-Ray Telescope (XRT) began to observe 144.7 s after the BAT trigger (D'Elia et al. 2017). Soon, Izzo et al. (2017a) found that the burst was located in a nearby galaxy at redshift $z = 0.0368$, which was later confirmed by the X-shooter telescope on board the Very Large Telescope (VLT/X-shooter; Izzo et al. 2017b). About 5 days after, the associated type Ic supernova (SN) started to emerge and was detected by the 10.4 m Gran Telescopio Canarias (GTC; de Ugarte Postigo et al. 2017) and the SMARTS 1.3 m telescope (Cobb 2017).

This source has gained much observational attention since it was the third nearest gamma-ray burst (GRB) at the time of its discovery. D'Elia et al. (2018) performed a multiwavelength analysis of GRB 171205A using the data from the Swift and Konus-Wind satellites, covering from the optical to the sub-megaelectronvolt energies. Their cutoff power-law fit gives the peak energy at ~100 keV and the isotropic energy in the order of 10^{49} erg, which implies this burst is a low-luminosity GRB and is an outlier of the Amati relation. Wang et al. (2018) reported the spectroscopic observation of the SN associated with the GRB, SN 2017iuk, and of the host galaxy. These observations showed that SN 2017iuk is a typical type Ic SN that resembles SN 2006aj, and that the host is an early-type, star-forming galaxy of high mass, low star formation rate, and low solar metallicity. In this source, for the first time, the polarization in the millimeter and radio bands during the afterglow phase was observed, thanks to the intensive combined use of the Submillimeter Array (SMA), the Atacama Large Millimeter/submillimeter Array (ALMA), and the Very Large Array (VLA), and showed a linear polarization $<1\%$ indicative of Faraday depolarization (Urata et al. 2019; Laskar et al. 2020). The observation continued for 1 yr, the ASKAP, ATCA, and μGMRT radio observations lasted ~1000 days, the radio afterglow decays followed a shallow power law, and no jet break was exhibited (Maity & Chandra 2021; Leung et al. 2021). Figure 1 shows the multiwavelength light curve of GRB 171205A.

1.1. GRB 171205A in the Traditional Scenario

The origin of low-luminosity GRBs is still an open debate, and some interpretations include that these are bursts observed off-axis (Waxman 2004; Soderberg et al. 2006a, 2006b;

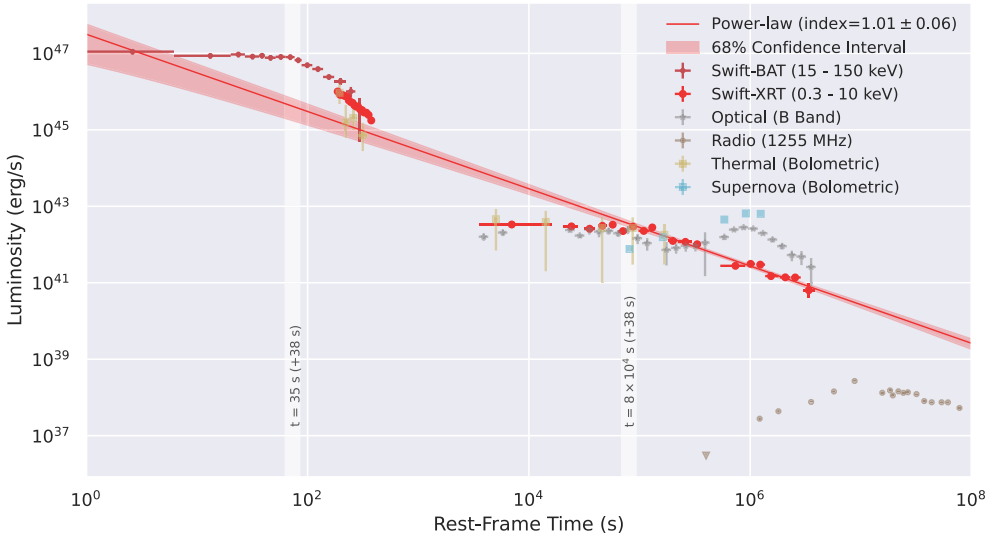

Figure 1. Luminosity light curve of Swift-BAT (deep red), Swift-XRT (red), optical *B* band from D'Elia et al. (2018) (gray), and radio 1255 MHz from Maity & Chandra (2021) (brown), the triangles represent the upper limit. We also plot the thermal luminosity (yellow). The Swift-XRT data at time $>8 \times 10^4$ s is fitted by a power law index of 1.01 ± 0.06 and extrapolated to the earlier and the later time (red solid line, the red shadow represents the 68% confidence interval). Here, $T_0 = 0$ s is the starting time of the burst, corresponding to 38 s before the BAT trigger time.

Kathirgamaraju et al. 2016; Fraija et al. 2019a; Izzo et al. 2020), shock-wave breakout from the progenitor's shell (Campana et al. 2006; Li 2007; Soderberg et al. 2008; Barniol Duran et al. 2015; Irwin & Chevalier 2016; Fraija et al. 2019b), and emission from a jet-heated cocoon (Nakar 2015; Kasliwal et al. 2017; Gottlieb et al. 2018). GRB 171205A, as a low-luminosity GRB at a low redshift, provides a testing ground for the theoretical models. Izzo et al. (2019) found thermal X-ray and optical emissions radiated from material whose velocity evolves from $\sim 0.3c$–$0.1c$ in the first 7 days, and with a chemical composition that differs from that of SN 2017iuk, which has a lower velocity ($<0.1c$) evidenced by the spectroscopic analysis. They proposed the high-velocity material is a portion of the accelerated cocoon, which becomes transparent at $\sim$7 days, and then the SN dominates the optical emission. Suzuki & Maeda (2022) performed hydrodynamic simulations of a powerful jet penetrating the progenitor star and showed that jet-induced chemical mixing can lead to the observed chemical composition of the high-velocity material. Maity & Chandra (2021) analyzed GRB 171205A with the shock-wave breakout and the canonical off-axis jet models and show that both are inconsistent with the 1000 day observations. Compared to the observation, the shock-wave breakout model predicts a longer duration, a lower peak energy, and requires a higher column density. Moreover, the radius ($\sim 10^{13}$ cm) derived from the thermal component is too large for a typical progenitor. For the off-axis model, the discrepancies arise because the burst does not exhibit expected off-axis properties like a low peak energy, an increasing luminosity in the afterglow, and a frequency-independent break in the light curve (D'Elia et al. 2018). There are alternative models, e.g., Suzuki et al. (2019) modeled the burst as mildly relativistic spherical ejecta interacting with an ambient wind-like medium producing forward and reverse shocks and forming a thin shell. In their model, the prompt gamma-ray and X-ray emissions are produced when the optical depth of the shell reaches transparency, and subsequently, the radio and X-ray emissions are produced in the shock fronts by synchrotron and inverse Compton processes. They claimed this model can fit the prompt luminosity and duration, as well as the late-time X-ray, optical, and radio light curves.

1.2. The BdHN Scenario

Therefore, a satisfactory explanation of the multiwavelength data and the evolution with time of GRB 171205A remains an open issue. In this work, we analyze this source from the perspective of the binary-driven hypernova (BdHN) model of long GRBs. The progenitor of the GRB in the BdHN model is a binary system composed of a carbon-oxygen (CO) star and a neutron star (NS) companion. Numerical simulations of the sequence of physical processes occurring in a BdHN have been performed in the last decade and have led to a detailed picture and interpretation of the GRB observables (see, e.g., Izzo et al. 2012; Rueda & Ruffini 2012; Fryer et al. 2014; Becerra et al. 2015; Fryer et al. 2015; Becerra et al. 2016; Ruffini et al. 2018c; Becerra et al. 2019). The core collapse of the CO star leads to the formation of a newborn NS (νNS) at its center and ejects the outer layers of the star in an SN explosion. The ejecta accretes onto the NS companion and due to matter fallback there is also accretion onto the νNS (see, e.g., Wang et al. 2022; Becerra et al. 2022; Rueda et al. 2022b, and references therein). Both accretion processes are hypercritical (i.e., highly super-Eddington) in view of the activation of a very efficient neutrino emission (Becerra et al. 2016, 2018). For orbital periods of a few minutes, the NS companion reaches the critical mass for gravitational collapse, leading to a Kerr black hole (BH). These BdHN are referred to as type I (BdHN I). BdHN I explain the energetic GRBs with isotropic energies $\gtrsim 10^{52}$ erg. The accretion processes are observed as precursors of the prompt emission (see, e.g., Wang et al. 2019). The gravitomagnetic interaction of the newborn Kerr BH with the surrounding magnetic field induces an electric field. For a sufficiently supercritical magnetic field, the electric field becomes also supercritical leading to an electron–positron (e^+e^-) pair plasma. The self-acceleration of this plasma to Lorentz factors $\Gamma \sim 100$ and its transparency explain the ultrarelativistic prompt emission (UPE) phase (see Moradi et al. 2021b for the UPE analysis of

Table 1
Physical Phenomena that Occur in BdHN I–III, and their Associated Observables in the GRB Data

Physical Phenomenon/Reference	BdHN Type	GRB Observable				
		νNS Rise (soft-hard X-rays)	UPE (MeV)	GeV emission	SXFs HXFs	Afterglow (X/optical/radio)
Early SN emission (a)	I, II, III	⊗				
Hypercritical accretion onto νNS (b)	I, II, III	⊗				
Hypercritical accretion onto NS (b)	I, II	⊗				
BH formation from NS collapse (c)	I			⊗		
Transparency of e^+e^- (from vacuum polarization) with low baryon load region (d)	I		⊗			
Synchrotron radiation inner engine: BH+B-field+SN ejecta (e)	I			⊗		
Transparency of e^+e^- (from vacuum polarization) with high baryon load (f)	I				⊗	
Synchrotron emission from SN ejecta with energy injection from νNS (g)	I, II, III					⊗
Pulsar-like emission from νNS (g)	I, II, III					⊗

Note. UPE stands for ultrarelativistic prompt emission, SXFs for soft X-ray flares, and HXFs for hard X-ray flares.
References. (a) Y. Aimuratov et al. (2023, in preparation), Wang et al. (2019, 2022), Rueda et al. (2022b), (b) Fryer et al. (2014), Becerra et al. (2016, 2022), Rueda et al. (2022b), Wang et al. (2022), (c) Ruffini et al. (2019), Moradi et al. (2021a, 2021b), (d) Bianco et al. (2001), Moradi et al. (2021b), Rastegarnia et al. (2022), (e) Ruffini et al. (2019), Rueda & Ruffini (2020), Moradi et al. (2021a), Rueda et al. (2022a), (f) Ruffini et al. (2018c), (g) Ruffini et al. (2018a), Wang et al. (2019), Rueda et al. (2020).

GRB 190114C, and Rastegarnia et al. 2022 for GRB 180720B). The electric field accelerates electrons to ultrarelativistic energies leading to synchrotron radiation, which explains the observed gigaelectronvolt emission (Ruffini et al. 2019; Rueda & Ruffini 2020; Moradi et al. 2021a; Rueda et al. 2022a). There is an additional synchrotron radiation process by relativistic electrons in the ejecta expanding in the νNS magnetic field. The νNS also injects energy into the ejecta. This synchrotron radiation explains the afterglow emission in the X-ray, optical, and radio wavelengths (see, e.g., Ruffini et al. 2018a; Wang et al. 2019; Rueda et al. 2020). Finally, the release of nickel decay (into cobalt) in the SN ejecta powers the bump observed in the optical in the late afterglow.

For longer orbital periods, of the order of tens of minutes, the NS companion does not reach the critical mass, so it remains a massive, fast-rotating NS. These BdHN are referred to as type II (BdHN II). BdHN II explain the less energetic GRBs with isotropic energies $\lesssim 10^{52}$ erg. The physical processes and related observables associated with the presence of the BH are clearly not observed in the BdHN II (e.g., the UPE and the gigaelectronvolt emission). The synchrotron afterglow in the X-ray, optical, and radio wavelengths, instead, is present both in BdHN I and II because it is powered by the νNS and the SN ejecta (see Wang et al. 2019, 2022 for GRB 180728A and GRB 190829A).

1.3. GRB 171205A and the Quest for BdHN III

When considering BdHN with longer and longer orbital periods, possibly of hours, the effects associated with the presence of the binary companion become observationally irrelevant. Therefore, there is no GRB observable that can discriminate the presence or absence of a binary companion. Under the above circumstances, we model GRB 171205A neglecting the observational consequences of a companion NS. We shall refer to these low-luminous sources with energies $\lesssim 10^{49}$–10^{50} erg as BdHNe III.

Table 1 summarizes the sequence of physical phenomena that occur in BdHN I–III, and their corresponding observables in the GRB data. Signatures from a binary companion appear only in BdHN I and II, while BdHN III shows only observables associated with the SN and the νNS.

In Section 2, we analyze the Swift observations and fit the time-resolved spectra using the Markov Chain Monte Carlo method, and then we generate the light curves for the prompt emission and afterglow, shown in Figures 1 and 2. The special feature of this burst is the presence of a thermal component in the early afterglow, where the temperature drops from about 90 to 70 eV in the first 300 s. In Section 3, we describe the physical process of this burst, we suggest that this low-luminosity burst originates from a strong SN (or a hypernova). The fallback accretion after the SN collapse heats up the SN ejecta, accelerating its outermost layer to mildly relativistic and the heated ejecta emits thermal radiation. This process is similar to the cocoon model, but the opening angle for the energy release of the fallback accretion is much larger than the traditional jet. This large opening angle is consistent with the absence of the jet break signal in the afterglow. Meanwhile, the fallback accretion spins up the central NS, which in turn injects energy to power the afterglow by losing its rotational energy. In Section 4, we establish the analytical solutions for the spin-up of the νNS due to the mass and angular momentum transfer during the accretion. We derive an analytical solution for the time required for the spin-up process using an accurate Padè approximant in the expression of the angular velocity as a function of time (see Figures 3 and 4). The spin period of the

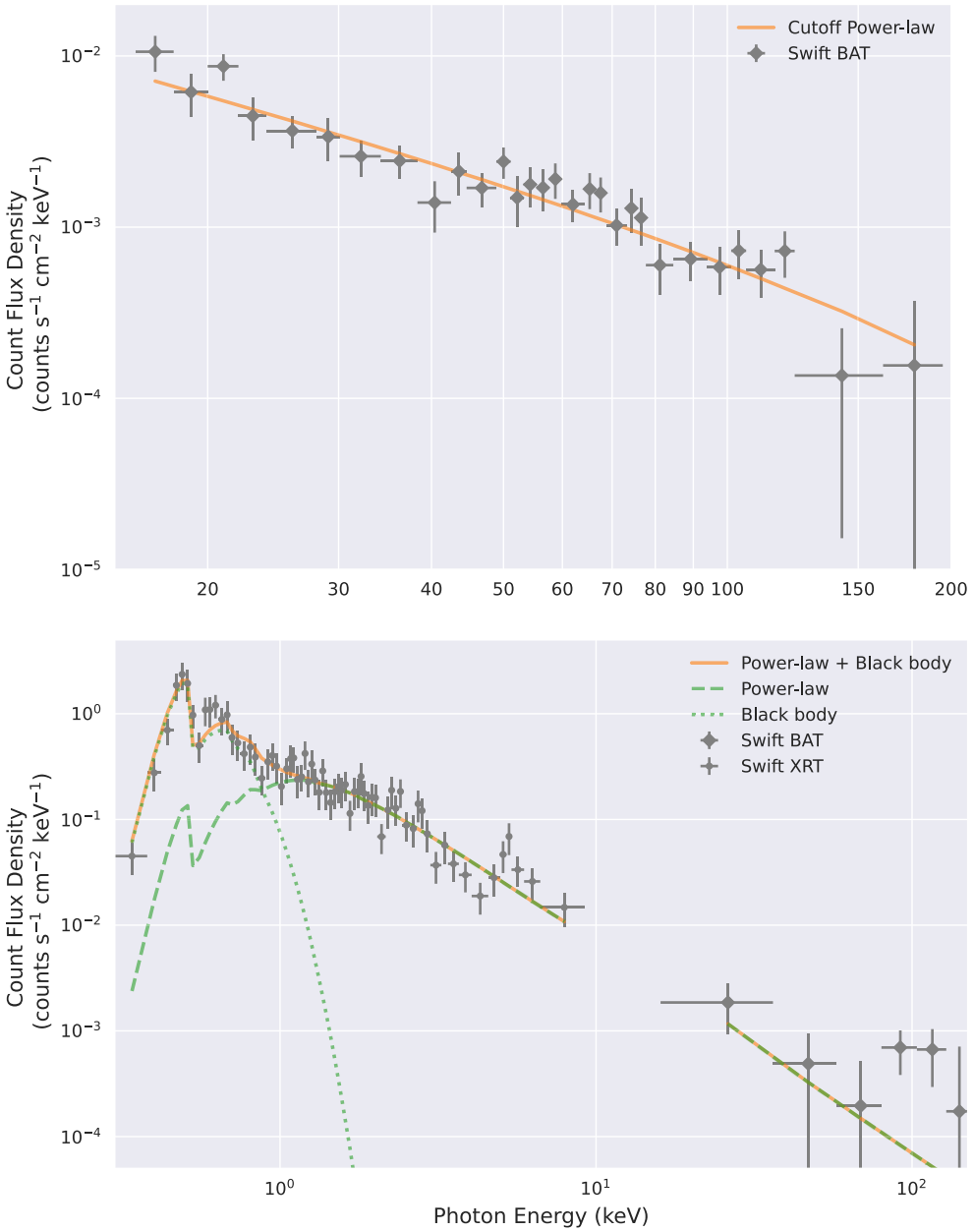

Figure 2. Top: spectrum of T_{90} observed by BAT, fitted by a cutoff power-law model with a photon index of $\alpha = 1.10 \pm 0.35$ and peak energy $E_p = 148.55 \pm 121.97$ keV. Bottom: jointly spectral fitting of BAT and XRT from 151–162 s after the BAT trigger with a composite spectrum of a power law index of $\alpha = 2.00 \pm 0.17$ plus a blackbody of temperature $kT = 77.48 \pm 7.46$ eV.

NS required by the theory can be obtained from the observation by assuming that the energy of the X-ray afterglow is mainly contributed by the rotational energy of the νNS. From the observation of GRB 171205A, we derive that the νNS is possibly accelerated to a spin period of 47 ms, and 0.026 $M_\odot$ are accreted by the νNS via fallback. We show that this process takes 7.36 hr for a νNS born with zero spin. In Section 5, we present the model of the afterglow in the X-ray, optical, and radio wavelengths as originating from synchrotron radiation in the expanding SN ejecta with the energy injection from the central 47 ms spinning νNS pulsar. Section 6 shows the results of the fit of the X-ray, optical, and radio light curves with the above model (see Figure 5). Our conclusions are given in Section 7.

2. Spectrum and Light Curve

Swift-BAT and Swift-XRT data are retrieved from UKSSDC,[14] and the data reduction is performed by HEAsoft 6.29,[15] then the exported spectra are fitted by the Multi-Mission Maximum Likelihood framework (3ML; Vianello et al. 2015). In order to produce the luminosity light curve, the BAT data are binned following the thresholds that the signal-to-noise ratio is at least 6 and the maximal bin size is at most 50 s. Then each binned spectrum is fitted by a cutoff power-law function and is integrated from 15–150 keV according to the BAT bandwidth

[14] http://www.Swift.ac.uk
[15] http://heasarc.gsfc.nasa.gov/lheasoft/

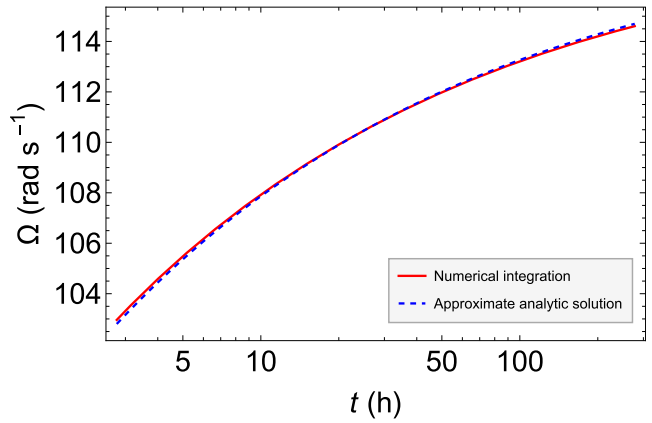

Figure 3. Comparison of the approximate solution of Equations (5) and (6) given by Equation (20), with the results from the full numerical integration, in the case $\mu(t_0) = 1.4$, $\Omega(t_0) = 0$, and $\chi = 0.15$.

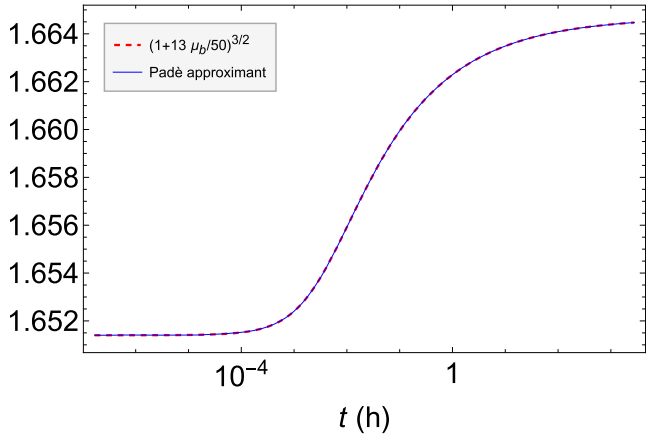

Figure 4. Comparison of the Padè approximant given by Equation (27) with the result of the full numerical integration.

to obtain the flux. After having the fitting parameters, the fluxes, and by adopting the FRW cosmology[16], the k-corrected luminosity light curve is obtained (Bloom et al. 2001). We generate the light curve of XRT in the energy range of 0.3–10 keV following a similar procedure, and the corresponding binning thresholds change to at least 200 counts and 10 s duration for the windows timing (WT) mode, as well as at least 100 counts and 100 s duration per bin for the photon counting mode. All the XRT spectra are fitted by a power-law function[17] with the photoelectric absorption models of our galaxy and the host galaxy. The generated Swift luminosity light curves are presented in Figure 1. We notice that this burst is seen since ∼38 s before the BAT trigger, hence, we set T_0 as 38 s before the BAT trigger time. The XRT light curve later than 8×10^4 s is fitted by a power-law function using lmfit (Newville et al. 2021), a python package for nonlinear optimization and curve fitting. lmfit implements the Levenberg–Marquardt method for optimization and is extended by numdifftool[18] to estimate the covariance matrix and then calculate parameter uncertainties. We obtain a power-law index of 1.01 ± 0.06 with the 1σ uncertainty (68% confidence level). We show the power-law fit in Figure 1 with the 1σ uncertainty region. The extrapolation of the power-law function coincides with the initial prompt luminosity.

The T_{90} of the BAT observation lasts 189.19 s, and its time-integrated can be described by a cutoff power-law model with a power-law index of $\alpha = 1.10 \pm 0.35$, while the peak energy cannot be precisely constrained $E_p = 148.55 \pm 121.97$ keV. These parameters are consistent with those in D'Elia et al. (2018), which jointly fitted BAT and Konus-Wind data. They obtained $\alpha = 0.85^{+0.54}_{-0.41}$ and $E_p = 122^{+111}_{-32}$ keV, where the uncertainty of peak energy has been tightened because Konus-Wind covers higher energies than BAT. The integrated flux gives $(1.56 \pm 0.31) \times 10^{-8}$ erg cm^{-2} s^{-1} in the observed 15–150 keV bandwidth, and extrapolated to $(2.63 \pm 0.54) \times 10^{-8}$ erg cm^{-2} s^{-1} in 1–10^4 keV, which corresponds to the isotropic energy $E_{\rm iso} = (1.71 \pm 0.35) \times 10^{49}$ erg.

The presence of a thermal component in the afterglow of GRB 171205A has been reported in several articles (Campana et al. 2017; D'Elia et al. 2018; Izzo et al. 2019). Our time-resolved analysis also confirms that the additional thermal component significantly improves the fit to the low energy band of the XRT (<1 keV) until 324 s with a fitting blackbody temperature that drops from ∼90 to ∼70 eV, with an uncertainty of ∼10 eV. Afterward, the thermal spectrum gradually fades out of the XRT band (0.3–10 keV) as the temperature decreases. The WT data of XRT is unable to constrain the temperature at a times later than ∼4000 s, while the optical telescopes start to capture the thermal component that cools to the optical band (Izzo et al. 2019).

There is a common time window for BAT and XRT observing the source, from ∼151 s when XRT had slewed to the GRB position, until ∼162 s, the end of the T_{90} of BAT. The BAT data at the end of the prompt emission is adequate to constrain the cutoff energy, hence, the model of a power law index of $\alpha = -2.00 \pm 0.17$ plus a blackbody component of $kT = 77.53 \pm 8.28$ eV is implemented to fit the entire data, as shown in Figure 2.

The optical and radio light curves shown in Figure 1 are reproduced from D'Elia et al. (2018) and Maity & Chandra (2021), respectively. The optical luminosity is unusually bright compared to the X-rays. Izzo et al. (2019) found that the evolution of the optical spectrum before and after 7 days is dominated by two black bodies with different evolution laws. The 1000 day radio light curve shows a shallow decay without any jet break signature. We refer to D'Elia et al. (2018), Izzo et al. (2019), Maity & Chandra (2021) for a detailed analysis and discussion of the optical and radio data, including the SN optical observation.

3. Physical Picture

At a given moment, a type Ic SN occurs from the core collapse of the CO star, forming at the same time a νNS at its center. The fallback accretion spins up the νNS (see Section 4), while releasing the accretion energy. From Becerra et al. (2019), the initial accretion rate is up to $10^{-3}\,M_\odot$ s^{-1} and lasts

[16] The Friedman–Lemaître–Robertson–Walker metric is used for computing the luminosity distance, Hubble constant $H_0 = 67.4 \pm 0.5$ km s^{-1} Mpc^{-1}, and matter density $\Omega_M = 0.315 \pm 0.007$ (Planck Collaboration et al. 2020).

[17] To have more data points for the light curve, our binning is more concerned with sufficiently short time resolution than with exact spectra. Therefore, the power-law model is used uniformly to fit the spectra, rather than the more accurate power-law plus blackbody model for which the data of each small bin cannot constrain all parameters. This introduces an error of less than 5%, which is in an acceptable level.

[18] https://numdifftools.readthedocs.io

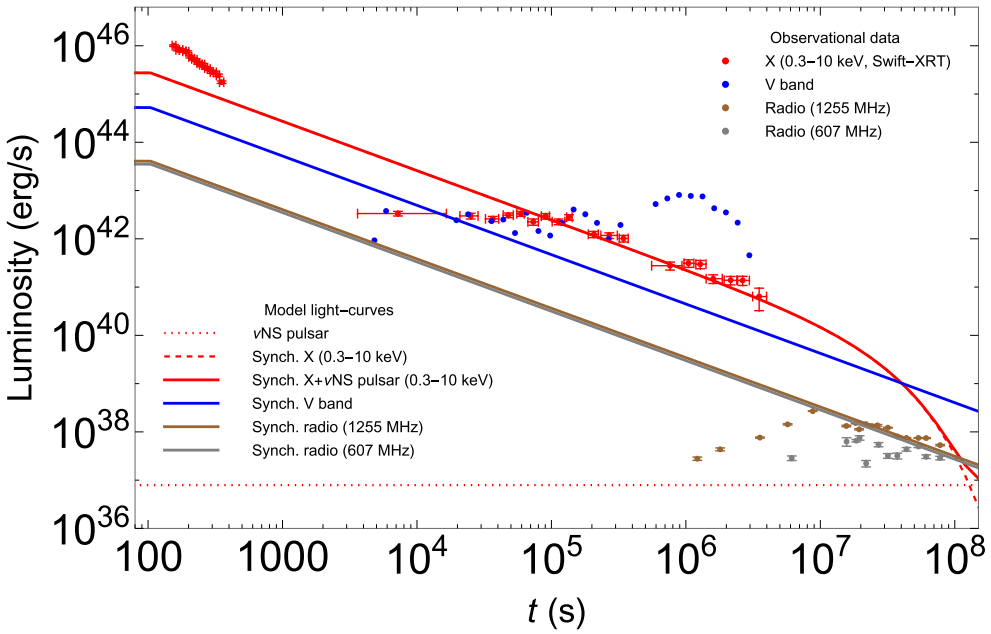

Figure 5. Luminosity of GRB 171205A in the X-ray (0.3–10 keV), optical (V band), and radio (607 MHZ and 1.255 GHz) energy bands compared with the luminosity predicted by the theoretical model. The rising part of the radio luminosity in the time interval of 10^6–10^7 s is due to synchrotron self-absorption (see Maity & Chandra 2021, for details), here unmodeled. The X-ray data is retrieved from the Swift-XRT repository and analyzed in this article, and the optical and radio data are reproduced from D'Elia et al. (2018) and Maity & Chandra (2021).

tens of seconds, then it drops following a power law depending on the SN density profile. Therefore, in the initial phase of tens of seconds, the total energy generated from the accretion and to be injected into the stellar shells reaches $\sim 10^{52}$ erg, which is comparable to the kinetic energy of SN ejecta inferred from the optical emissions at a later time. Different from the traditional jetted model of GRBs, this amount of energy is emitted in a large opening angle of probably tens of degrees, it propagates in a portion of shells and accelerates the outermost shell to mildly relativistic velocity. The hydrodynamics can be referred to the simulation in Ruffini et al. (2018c), where has been simulated the propagation of GRB injected energy in the expanding stellar shells. The Lorentz factor of the shock wave is lower than 5 when it breaks out the outermost shell at $\sim 10^{12}$ cm. The acceleration of the accretion-powered blastwave is similar to that proposed for the shock-accelerated GRB model (Colgate 1974). In this scenario, a supernova blastwave accelerates as it propagates down the steep density gradient at the edge of a massive star (Colgate 1974; Tan et al. 2001). Although these models can produce highly relativistic ejecta in idealized conditions, the bulk of the material reaches only mildly relativistic velocities. Our model mirrors this evolution, differing only from this picture because the blastwave is propagating through an exploding CO star and is not spherical. Our asphericity has many of the features of the cocoon produced in jet models (see, e.g., Meszaros & Rees 2001; Ramirez-Ruiz et al. 2002; Zhang et al. 2004; Nakar & Piran 2017; Soker 2022; Eisenberg et al. 2022) that the jet pushes the stellar shells sideways to form a hot cocoon, a part of the cocoon emerges from the shells and expands outward with mildly relativistic velocity. Hence, both our picture and the cocoon picture involve some heated high-velocity material originating from the stellar shells expanding and emitting a thermal spectrum. The evolution of such this blackbody spectrum has been indeed observed by Swift-XRT and several optical telescopes, and a mass of $1.1 \times 10^{-3}\, M_\odot$ moving above $10^5\,\mathrm{km\,s^{-1}}$ has been inferred; see Figure 2 and Izzo et al. (2019). The difference is that in our picture, we expect a wider opening angle than in a jet, as we consider this low-luminosity GRB originates from a strong SN or hypernova in which the central compact object is the νNS. From the observations, there is no signature of any jet break in the afterglow until $\sim$1000 days (Maity & Chandra 2021; Leung et al. 2021), hence, preferring a large opening angle description.

At this stage, our system has three energy sources: the accretion, the spinning νNS, and the high-velocity material. For the prompt emission, this low-luminosity GRB deviates from the Amati relation (Amati et al. 2002); its peak energy ($E_p = 148.55$ keV, see Figure 2) is about one order of magnitude higher than the typical value of a weak GRB with isotropic energy $\sim 10^{49}$ erg (D'Elia et al. 2018). The deviation indicates this burst could be an extreme case or is formed by a different mechanism. Izzo et al. (2019) suggest that the jet deposits the majority of energy in the creation of the cocoon and only a small fraction of energy is emitted in gamma rays. In our framework, accretion dominates the energy release once the SN explodes, and the majority of energy is injected into the stellar shells, converting to the internal and kinetic energy of the SN ejecta, and producing the fast-moving material. The low isotropic energy of the prompt emission can be either produced by the tail of accretion or by the fast-moving material (De Colle et al. 2018). For the X-ray afterglow, it can be accounted for, at early times, by the synchrotron emission converted from the kinetic energy of the fast-moving material, and at times after the plateau, by the release of rotational energy of the νNS that has been spun up to periods of the order of milliseconds. We performed the numerical fitting of the spectrum and light curve using this scenario for several GRBs (see, e.g., Ruffini et al. 2018a; Wang et al. 2019; Rueda et al. 2020). This is also supported by that the ending time of the plateau coincides with

the transparency of the fast-moving material at $\sim 10^5$ s. For the optical afterglow, we share the same opinion as Izzo et al. (2019) that the fast-expanding mass dominates the optical emission before 4 days, then the dominance is overtaken by photons diffused out from the massive SN ejecta heated by the nickel radioactive decay.

The above picture contains many different physical processes, most of which have been discussed in detail and simulated, in the references mentioned in the text. However, after the birth of a νNS, the fallback accretion, the mass change, and the spin-up process have been rarely discussed in GRB studies. Hence, we will focus on modeling the properties of the νNS in the next section.

4. Spin-up and Fallback Accretion onto the νNS

We turn now to estimate the spin-up and the amount of mass that the νNS has accreted to gain enough rotational energy to power the X-ray afterglow emission, as specified in the BdHN model (see, e.g., Ruffini et al. 2021, for the analysis of 380 BdHNe).

Assuming the X-ray luminosity as a good proxy of the bolometric luminosity of the afterglow, we can estimate the change in the νNS rotational energy from a time t_1 to a time $t_2 > t_1$ from the energy balance equation, i.e.,

$$\int_{t_1}^{t_2} \dot{E}_{\rm rot}\, dt = E_{\rm rot}(t_2) - E_{\rm rot}(t_1) \approx -\int_{t_1}^{t_2} L_X dt. \tag{1}$$

After an infinite time, the νNS will have lost all its rotational energy; therefore, when $t_2 \to \infty$, we have $E_{{\rm rot},\infty}(t_2) \to 0$. So, assuming the time t_1 to be a generic time t, and the power-law luminosity

$$L_X = A_X t^{-\alpha_X}, \tag{2}$$

we obtain from Equation (1) that the νNS angular velocity evolves as

$$\Omega(t) \approx \sqrt{\frac{2A_X\, t^{1-\alpha_X}}{(\alpha_X - 1)I}}, \tag{3}$$

where I is the stellar moment of inertia, which we have assumed constant with time, and can be estimated, for instance, using the EOS-independent approximate expression (Wei et al. 2019)

$$I \approx \left(\frac{G}{c^2}\right)^2 M^3 \sum_{i=1}^{4} \frac{b_i}{(M/M_\odot)^i}, \tag{4}$$

where $b_1 = 1.0334$, $b_2 = 30.7271$, $b_3 = -12.8839$, and $b_4 = 2.8841$.

In the case of GRB 171205A, the X-ray luminosity is fitted by a power law at times $t > t_{\rm pl} \approx 8 \times 10^4$ s, with $A_X = (3.165 \pm 0.238) \times 10^{47}$ erg s^{-1}, and $\alpha_X = 1.022 \pm 0.055$. Using these values, we estimate from Equation (3) that the rotation period of the νNS at $t = t_{\rm pl}$ is $P(t_{\rm pl}) \approx 51.01$ ms. If we assume that the νNS is spinning down from the νNS rise, i.e., from $t = t_{\nu\rm NS} \approx 35$ s, but the emission from it is partially absorbed by the high-velocity material, which is opaque before $\sim 10^5$ s, then by extrapolating from $t = t_{\rm pl}$ backward in time to $t = t_{\nu\rm NS}$, we infer that at the νNS-rise time, the νNS rotation period was $P_{\nu\rm NS} \equiv P(t_{\nu\rm NS}) \approx 46.85$ ms, i.e., $\Omega(t_{\nu\rm NS}) = 134.11$ rad s^{-1}.

We now estimate the mass accreted by the νNS before the νNS rise to spin it up to the above rotation rate. The accretion rate onto the νNS, set by the amount of mass from the inner layers of the expanding matter that fall back onto the νNS and their infalling speed, proceeds at hypercritical rates (see, e.g., Fryer et al. 1996). The accretion process makes the νNS increase its mass energy and rotation rate from the transfer of baryonic mass and angular momentum. The evolution of the νNS gravitational mass and angular momentum can be calculated from (Becerra et al. 2019)

$$\dot{M} = \left(\frac{\partial M}{\partial M_b}\right)_J \dot{M}_b + \left(\frac{\partial M}{\partial J}\right)_{M_b} \dot{J}, \tag{5}$$

$$\dot{J} = \tau_{\rm acc}, \tag{6}$$

where $J = I\Omega$ is the angular momentum, M is the gravitational mass, M_b is the baryonic mass, $\dot{M}_b$ is the baryonic mass accretion rate, and $\tau_{\rm acc}$ is the accretion torque.

Equation (5) must be complemented with the expressions of the two partial derivatives. These relations can be calculated from the fitting formula of the NS binding energy obtained in Cipolletta et al. (2015)

$$\mu_b - \mu = \frac{13}{200}\mu^2\left(1 - \frac{1}{130}j^{1.7}\right), \tag{7}$$

where $j \equiv cJ/(GM_\odot^2)$ is the dimensionless angular momentum and $\mu = M/M_\odot$. From it, we readily obtain

$$\left(\frac{\partial \mu}{\partial \mu_b}\right)_j = \frac{1}{1 + \frac{13}{100}\mu\left(1 - \frac{1}{130}j^{1.7}\right)}, \tag{8}$$

$$\left(\frac{\partial \mu}{\partial j}\right)_{\mu_b} = \frac{\frac{1.7}{2000}\mu^2 j^{0.7}}{1 + \frac{13}{100}\mu\left(1 - \frac{1}{130}j^{1.7}\right)}. \tag{9}$$

The numerical simulations of BdHNe performed in Becerra et al. (2019) show that the material accreted by the νNS circularizes around it in a sort of Keplerian disk structure before being accreted. Therefore, we assume that the accreted matter exerts onto the νNS the torque

$$\tau_{\rm acc} = \chi\, l\, \dot{M}_b, \tag{10}$$

where l is the specific (i.e., per unit mass) angular momentum of the innermost stable circular orbit around the νNS, and $\chi \leqslant 1$ is an efficiency parameter of angular momentum transfer. For the angular momentum of the last stable circular orbit, we use the approximate EOS-independent results presented in Cipolletta et al. (2017),

$$l = 2\sqrt{3}\frac{GM}{c}\left[1 \mp 0.107\left(\frac{j}{M/M_\odot}\right)^{0.85}\right]. \tag{11}$$

We can obtain an approximate, analytic solution to Equation (6). For this task, we use the following analytic formula that fits the numerical results of the fallback accretion rate calculated in Becerra et al. (2019, 2022),

$$\dot{M}_b \approx \dot{M}_0(1 + \bar{t})^{-p}, \tag{12}$$

where $\dot{M}_0 = 7.2 \times 10^{-4} M_\odot$ s^{-1}, $t_{\rm acc} = 12$ s, $p = 1.3$, and we have introduced the notation $\bar{t} = t/t_{\rm acc}$.

For the involved rotation rates ($j \sim 0.01$), the contribution of the rotation terms in Equations (7) and (11) is negligible, so we can retain only the first term in those equations. With this

assumption, and integrating Equation (12), we have

$$\mu_b = \mu_b(t_0) + \frac{\dot{M}_0 t_{\rm acc}}{p-1}[1-(1+\bar{t})^{1-p}], \tag{13}$$

$$\mu \approx \frac{100}{13}\left(\sqrt{1+\frac{13}{50}\mu_b}-1\right), \tag{14}$$

$$l \approx 2\sqrt{3}\frac{GM_\odot}{c}\mu, \tag{15}$$

where $\mu_b(t_0) \approx \mu_0 + (13/200)\mu_0^2$, $\mu_0 = M(t_0)/M_\odot$ is the initial νNS gravitational mass, and we have inverted Equation (7) to write the gravitational mass in terms of the baryonic mass. Equations (13) and (14) imply that in the limit $t \to \infty$ the baryonic mass and the gravitational mass approach a maximum value

$$\mu_{b,\max} = \mu_b(t_0) + \frac{\dot{M}_0 t_{\rm acc}}{p-1} = \mu_b(t_0) + 0.0288, \tag{16}$$

$$\mu_{\max} = \frac{100}{13}\left(\sqrt{1+\frac{13}{50}\mu_{b,\max}}-1\right). \tag{17}$$

We now approximate the angular momentum derivative as $\dot{J} \approx I\dot{\Omega} \approx I_{\max}\dot{\Omega}$, where $I_{\max} = I(\mu_{\max})$, so that Equation (6) becomes

$$\dot{\Omega} \approx \beta\mu(t)(1+\bar{t})^{-p}, \quad \beta = \frac{2\sqrt{3}GM_\odot^2\chi\dot{\mu}_0}{cI_{\max}}, \tag{18}$$

whose solution can be written as

$$\Omega(t) = \Omega(t_0) + \beta\int_{t_0}^{t}\mu(t)(1+\bar{t})^{-p}dt. \tag{19}$$

Making the change in variable $x = (1+\bar{t})^{1-p}$, the integration of Equation (19) is straightforward leading to

$$\begin{aligned}\Delta\Omega &= \Omega(t) - \Omega(t_0)\\ &= \omega\left\{x + \frac{2}{3}k\left[\left(1+\frac{13\mu_b}{50}\right)^{3/2} - \alpha^{3/2}\right] - 1\right\},\end{aligned} \tag{20}$$

where we have defined

$$\omega = \frac{100}{13}\frac{\beta\, t_{\rm acc}}{p-1}, \quad \Delta\mu_b = \frac{\dot{M}_0 t_{\rm acc}}{p-1} = 0.0288, \tag{21}$$

$$k = \frac{50}{13}\frac{1}{\Delta\mu_b} = 133.547, \quad \alpha = 1 + \frac{13}{50}\mu_{b,0} \tag{22}$$

and we have set the initial time $t_0 = 0$ since the fallback accretion begins soon after the SN explosion (see, e.g., Becerra et al. 2019). Figure 3 compares the approximate analytic solution (20) with the solution from the full numerical integration of Equations (5) and (6), in the case of $\mu(t_0) = 1.4$, $\Omega(t_0) = 0$, and $\chi = 0.15$.

Equation (20) tells us that in the limit $t \to \infty$ ($x \to 0$), the νNS reaches asymptotically a maximum angular velocity gain of

$$\Delta\Omega_{\max} = \omega\left\{\frac{2}{3}k\left[\left(1+\frac{13\mu_{b,\max}}{50}\right)^{3/2} - \alpha^{3/2}\right] - 1\right\}, \tag{23}$$

which as expected is larger for larger values of the angular momentum transfer efficiency parameter, χ. Since we assume that after the νNS rise the νNS is spinning down, we seek solutions with a spinning up phase that ends with an angular velocity approaching the value that we have inferred at the νNS rise, i.e.,

$$\Omega_{\max} \approx \Omega(t_{\nu\rm NS}), \tag{24}$$

where $\Omega_{\max} = \Delta\Omega_{\max} + \Omega(t_0)$. We have used the approximate symbol in Equation (24) because by definition the value $\Omega_{\max}$ is reached only asymptotically. For practical purposes, we seek solutions in which $\Omega(t_{\nu\rm NS}) = 0.9\,\Omega_{\max}$. Therefore, given the values of M and $\Omega(t_{\nu NS})$, the above constraint leads to a specific value of χ that leads to the self-consistent spin-up phase. For instance, for a νNS mass $M = 1.4M_\odot$ and

$$\Omega_{\nu\rm NS} \equiv \Omega(t_{\nu\rm NS}) = \sqrt{\frac{2A_X\, t_{\nu\rm NS}^{1-\alpha_X}}{(\alpha_X-1)I}} \approx 134.11 \text{ rad s}^{-1}, \tag{25}$$

we obtain $\chi = 0.182$.

We can also obtain a simple analytic estimate of the mass accreted by assuming that during the spin-up phase, the accretion rate, the gravitational mass, and the moment of inertia are constant and have their maximum values. Under this assumption, Equations (6) and (10) lead to the accreted mass in a time Δt,

$$\Delta\mu_b \approx \frac{cI_{\max}\Delta\Omega}{2\sqrt{3}\chi GM_\odot^2\mu_{\max}}. \tag{26}$$

For the above parameters, Equation (26) gives $\Delta\mu_b \approx 0.02570$. This is very close to the value obtained from the full numerical integration, $\Delta\mu_b = 0.02592$, which represents an error of only 0.85%. The accuracy of Equation (26) resides in the fact that the fallback accretion rate decreases as a power law, see Equation (12), hence most of the baryonic mass is accreted in the first minutes of the evolution. This explains why the above value of the accreted mass is close to the maximum accreted mass given by Equation (16), i.e., $\Delta\mu_{b,\max} = 0.0288$.

We turn to obtain an analytic expression of the time interval Δt elapsed since the beginning of the fallback accretion, up to the instant when the νNS reaches a given angular velocity, or a given angular velocity gain, $\Delta\Omega$. In principle, we can obtain it by inverting Equation (20). However, the equation is highly nonlinear, so to obtain a relatively simple expression for it we use an accurate Padè approximant for the quantity involving the baryonic mass, i.e.,

$$\begin{aligned}\left(1+\frac{13\mu_b}{50}\right)^{3/2} &= b^{3/2}(\tilde{\alpha}+X)^{3/2} \approx b^{3/2}(\mathcal{F}+\tilde{\alpha}^{3/2}),\\ \mathcal{F} &= \frac{6\tilde{\alpha}^{3/2}X}{4\tilde{\alpha}-X},\end{aligned} \tag{27}$$

where $b = 1/k = (13/50)\Delta\mu_{b,\max}$, $\tilde{\alpha} = \alpha/b$, and we have introduced the variable $X = 1-x$. For the same example in Figure 3, we show in Figure 4 the excellent performance of the Padè approximant (27), which approximates the expression with a tiny error of only 10^{-9}.

Using the approximant (27), Equation (20) becomes a second-order polynomial in the variable X whose solution is

straightforward, leading to the time interval:

$$\Delta t = t_{\rm acc}[(1 - X)^{\frac{1}{1-p}} - 1], \tag{28}$$

where

$$X = \frac{B + \sqrt{B^2 + 4C}}{2}, \tag{29}$$

$$B = 4\tilde{\alpha} - 4\tilde{\alpha}^{3/2}\sqrt{b} - \Delta\Omega/\omega, \tag{30}$$

$$C = 4\tilde{\alpha}\Delta\Omega/\omega. \tag{31}$$

The relevance of the above time interval is that it allows computation of the time elapsed to reach the angular velocity at the νNS rise, $\Omega(t_{\nu\rm NS})$. Since it is close to the maximum value reachable by the fallback accretion, that time interval gives an estimate of the time elapsed since the SN explosion (SN rise), $t_{\rm SN}$. For the present example, we obtain

$$t_{\rm SN} = \Delta t(\Delta\Omega) = \Delta t(\Omega_{\nu\rm NS}) \approx 7.36\ {\rm hr}, \tag{32}$$

where we have used $\Delta\Omega = \Omega_{\nu\rm NS} - \Omega(t_0) = 134.11\ {\rm rad\ s^{-1}}$, as given by Equation (25). The full numerical integration leads to 7.20 hr, which implies that Equation (28) estimates the time interval with an error of only 2.2%.

5. Synchrotron and Pulsar Emission

We turn now to the specific modeling of the multi-wavelength afterglow of GRB 171205A. In the present scenario, the nonthermal component of the afterglow originates from the synchrotron radiation in the SN ejecta. The SN ejecta gets energy injected from the νNS fallback accretion and the multipolar emissions. Numerical calculations of this model applied to the description of the afterglow of specific GRBs can be found in Ruffini et al. (2018a), Wang et al. (2019), and Rueda et al. (2020). An analytic treatment of the model has been presented in Rueda (2022), and Wang et al. (2022) have applied it to model the afterglow of GRB 180720B. Our afterglow model relies more on continuous energy injections than the traditional forward shock-wave model, which relies on the kinetic energy of the jet. And unlike the traditional model that only considers the injection of dipole emission as an additional energy source to explain the short-duration plateau (e.g., internal plateau) (Dai & Lu 1998a, 1998b; Zhang & Mészáros 2001; Metzger et al. 2011; Lehner et al. 2012; Chen et al. 2017; Li et al. 2018; Zhao et al. 2020), our modeling process takes into account the fallback accretion, the dipole, and quadrupole radiation, such that continuous energy injections produce the long-lasting afterglow. Here, we follow the latter to estimate for GRB 171205A the emission generated by the synchrotron mechanism in the X-ray, optical, and radio wavelengths, and the νNS pulsar emission.

5.1. Synchrotron Emission by the Expanding Ejecta

The distribution of radiating electrons per unit energy, $N(E, t)$, is obtained from the solution of the kinetic equation (Kardashev 1962)

$$\frac{\partial N(E,\,t)}{\partial t} = -\frac{\partial}{\partial E}[\dot{E}\,N(E,\,t)] + Q(E,\,t), \tag{33}$$

where $Q(E, t)$ is the number of injected electrons into the ejecta per unit time t, per unit energy E, and $\dot{E}$ is the electron energy loss rate.

Following Rueda (2022) and Wang et al. (2022), we adopt the solution to Equation (33) for a self-similar uniform expansion

$$N(E,\,t) \approx \begin{cases} \dfrac{q_0}{\beta B_{*,0}^2(\gamma-1)}\hat{t}^{\,2}E^{-(\gamma+1)}, & t < t_q \\ \dfrac{q_0(t_q/t_*)^k}{\beta B_{*,0}^2(\gamma-1)}\hat{t}^{\,2-k}E^{-(\gamma+1)}, & t_q < t < t_b, \end{cases} \tag{34}$$

where $E_b < E < E_{\rm max}$,

$$E_b = \frac{\hat{t}}{\mathcal{M}t_*}, \quad t_b = \mathcal{M}t_*^2E_{\rm max}. \tag{35}$$

The model parameters are defined as follows. The ejecta expands self-similarly with the radiating layer being $r = R_* = R_{*,0}\,\hat{t}$, $\hat{t} \equiv t/t_*$, $t_* = R_*/v_* = R_{*,0}/v_{*,0}$, $v_* = R_*(t)/t = v_{*,0}$, $B_*(t) = B_{*,0}R_{*,0}/r = B_{*,0}\hat{t}^{-1}$ is the magnetic field strength at $r = R_*$, $\mathcal{M} \equiv \beta B_{*,0}^2/2$, $\beta = 2e^4/(3m_e^4c^7)$. We assume the injection power-law distribution of $Q(E,\ t) = Q_0(t)E^{-\gamma}$ (Kardashev 1962; Pacini & Salvati 1973; Rybicki & Lightman 1979; Longair 2011), where γ and $E_{\rm max}$ are parameters to be determined from the observational data, and $Q_0(t)$ can be related to the power released by the νNS and injected into the ejecta from $L_{\rm inj}(t) = L_0(1 + t/t_q)^{-k} = \int_0^{E_{\rm max}} E\ Q(E,\,t)dE$, so $Q_0(t) = q_0(1 + t/t_q)^{-k}$, where $q_0 \equiv (2 - \gamma)L_0/E_{\rm max}^{2-\gamma}$.

The bolometric synchrotron radiation power of a single electron is given by (see, e.g., Longair 2011)

$$P_{\rm syn}(E,\,t) = \beta B_*^2(t)E^2 \approx \frac{\beta}{\alpha}B_*\nu, \tag{36}$$

where in the last equality we have used the fact that most of the radiation is emitted at frequencies near the so-called critical frequency, $\nu_{\rm crit} = \alpha B_*E^2$, where $\alpha = 3e/(4\pi m_e^3c^5)$. By setting $N(E,\,t) = \eta\,\hat{t}^{\,l}E^{-p}$, so that with the constants η , l, and p obtained by comparing this expression with Equation (34), the synchrotron luminosity radiated at frequencies from ν_1 to $\nu_2 > \nu_1$ can be written as

$$\begin{aligned} L_{\rm syn}(\nu_1,\,\nu_2;\,t) &= \int_{\nu_1}^{\nu_2} J_{\rm syn}(\nu,\,t)d\nu \approx \nu J_{\rm syn}(\nu,\,t), \\ &\approx \frac{\beta}{2}\alpha^{\frac{p-3}{2}}\eta B_{*,0}^{\frac{p+1}{2}}\hat{t}^{\frac{2l-n(p+1)}{2}}\nu^{\frac{3-p}{2}}, \end{aligned} \tag{37}$$

where $\nu_1 = \nu$, $\nu_2 = \nu + \Delta\nu$, $\Delta\nu$ is the bandwidth. Here, $J_{\rm syn}$ is the spectral density, which is given by $J_{\rm syn}(\nu,\,t)d\nu \approx P_{\rm syn}(\nu,\,t)N(E,\,t)dE$ (see, e.g., Longair 2011). In Equation (37), we have made the approximation $\Delta\nu/\nu \ll 1$ because of the power-law character of the spectral density. Despite the synchrotron radiation of a single electron being beamed along the velocity of the particle, here we consider an isotropic distribution of a large number of electrons with an isotropic distribution of pitch angles, hence, leading to an isotropic total synchrotron luminosity.

5.2. νNS Evolution and Pulsar Emission

The νNS is subjected to the angular momentum loss driven by the magnetic field braking. In the point dipole+quadrupole magnetic field model presented in Petri (2015), the total

magnetic torque is given by

$$\tau_{\rm mag} = \tau_{\rm dip} + \tau_{\rm quad}, \tag{38}$$

$$\tau_{\rm dip} = -\frac{2}{3}\frac{B_{\rm dip}^2 R^6 \Omega^3}{c^3}\sin^2\alpha, \tag{39}$$

$$\tau_{\rm quad} = -\frac{32}{135}\frac{B_{\rm quad}^2 R^8 \Omega^5}{c^5}\sin^2\theta_1(\cos^2\theta_2 + 10\sin^2\theta_2), \tag{40}$$

where α is the inclination angle of the magnetic dipole moment with respect to the rotation axis, and the angles θ_1 and θ_2 specify the geometry of the quadrupole field. The strength of the magnetic dipole field is $B_{\rm dip}$. The dipole pure axisymmetric mode ($m=0$) is set by $\alpha=0$, and the pure $m=1$ mode by $\alpha=\pi/2$. The strength of the quadrupole magnetic field is $B_{\rm quad}$. The quadrupole $m=0$ mode is set by $\theta_1=0$, the $m=1$ mode by $\theta_1=\pi/2$ and $\theta_2=0$, while the $m=2$ mode is set by $\theta_1=\theta_2=\pi/2$. For the fit of the data, we shall adopt the $m=1$ mode for the dipole while the quadrupole can range between the $m=1$ and $m=2$ modes. The existence of multipolar magnetic fields in the νNS is supported by some theories and observations (Mastrano et al. 2013; Tiengo et al. 2013; Rodríguez Castillo et al. 2016; Pons & Viganò 2019). Therefore, we can write the total magnetic torque (38) as

$$\tau_{\rm mag} = -\frac{2}{3}\frac{B_{\rm dip}^2 R^6 \Omega^3}{c^3}\left(1 + \xi^2\frac{16}{45}\frac{R^2\Omega^2}{c^2}\right), \tag{41}$$

where ξ is the quadrupole-to-dipole magnetic field strength ratio is defined by

$$\xi \equiv \sqrt{\cos^2\theta_2 + 10\sin^2\theta_2}\,\frac{B_{\rm quad}}{B_{\rm dip}}, \tag{42}$$

and the spin-down luminosity as

$$L_{\rm sd} = \Omega\,|\tau_{\rm mag}| = \frac{2}{3}\frac{B_{\rm dip}^2 R^6 \Omega^4}{c^3}\left(1 + \xi^2\frac{16}{45}\frac{R^2\Omega^2}{c^2}\right). \tag{43}$$

The evolution of the νNS is obtained from the energy conservation equation

$$-(\dot{W} + \dot{T}) = L_{\rm tot} = L_{\rm inj} + L_{\rm sd}, \tag{44}$$

where W and T are, respectively, the νNS gravitational and rotational energy.

6. Results

The emission of GRB 171205A comprises thermal and nonthermal components. In Section 1.1, we recalled that Izzo et al. (2019) explain the thermal component up to 10^5 s in the X-rays and in the optical due to the cooling of fast-moving material. Here we here address the nature of the nonthermal component once the material is transparent. Therefore, the present model of synchrotron radiation described in Section 5 aims to explain the data that shows a decreasing power-law luminosity in the different energy bands with similar power-law indexes.

Table 2 summarizes the values of the model parameters that fit the afterglow of GRB 171205A in the X-ray, optical, and radio energy bands, as shown in Figure 5, obtained according to the above guidelines and the fitting procedure outlined in the Appendix.

Table 2
Value of the Synchrotron Model Parameters that Fit the Multiwavelength Observational Data of GRB 1701205A as Shown in Figure 5

Parameter	Value
t_* (10^4 s)	2.650 ± 110.276
$B_{*,0}$ (10^5 G)	3.774 ± 157.021
γ	1.606 ± 0.231
$E_{\rm max}$ ($10^4\ m_e c^2$)	3.738
k	1.219 ± 0.170
L_0 (10^{47} erg s^{-1})	1.011 ± 0.801
t_q (s)	100.00
$B_{\rm dip}$ (10^{12} G)	1.000
$P_{\nu\rm NS}$ (ms)	46.852 ± 64.910

In the X-rays, the model describes the decreasing power-law behavior at times $>10^5$ s, and in the radio at times $>10^7$ s. We do not model the rising part of the radio emission in the time interval of 10^6–10^7 s, which is due to synchrotron self-absorption (see Maity & Chandra 2021, for details).

The first relevant feature to notice is that the afterglow luminosity fades with time with an approximate power law t^{-1}. This power law is shallower than in GRBs of higher luminosity in which $t^{-1.3}$ (see, e.g., GRB 130427A or GRB 190114C in Ruffini et al. 2018a; Rueda et al. 2020). The pulsar emission from magnetic braking predicts a luminosity with a sharper power law, in a pure magnetic dipole the luminosity falls as t^{-2}, and for a pure magnetic quadrupole as $t^{-3/2}$ (see equations of Section 5.2 and Ruffini et al. 2018a; Rueda et al. 2020). Therefore, models based on pulsar emission from magnetic braking alone (even including higher-order multipole fields) are unable to fit the afterglow luminosity of GRB 171205A. This is the first indication of the necessity of an additional mechanism, in this case, the synchrotron radiation. The second relevant feature is that the afterglow in the X-ray and radio bands shows a similar power-law index (see the red, gray, and brown data points), as expected from the synchrotron model.

The optical data shows, instead, a flat behavior followed by the bump that characterizes the peak of the SN emission powered by the decay of nickel in the ejecta (Arnett 1996; Izzo et al. 2019). Both the synchrotron radiation and the SN radioactive decay contribute to the optical emission, but in GRB 171205A the latter dominates over the former. This explains the deviation of the optical luminosity from the typical power-law behavior of synchrotron radiation. This feature is consistent with the BdHN III nature of the source. In fact, BdHN III are low-luminous sources in which the νNS is not a very fast rotator, so it injects less energy into the ejecta in comparison to BdHNe I (e.g., GRB 130427A, 180720B, or 190114C; see Ruffini et al. 2018a; Rueda et al. 2020) and BdHNe II (e.g., GRB 190829A; see Wang et al. 2022). Therefore, the synchrotron emission is not very luminous and the emergent optical SN outshines the optical synchrotron luminosity. Interestingly, this latter feature of the emergent optical SN emission is also fulfilled in the most general situation of BdHN I and BdHN II (Y. Aimuratov et al. 2023, in preparation). SN 2017iuk is similar to the SNe associated with high-luminous GRBs, indicating that the pre-SN progenitor (i.e., the CO star and an NS companion) leading to the νNS in its core-collapse event, is similar for all long GRBs irrespective of their energetics (Y. Aimuratov et al. 2023, in preparation).

In the X-rays, the synchrotron luminosity fades off after a few 10^6 s, when $h\nu_{\rm crit}$ falls below a kiloelectronvolt. At later

times, the power-law behavior continues in the optical and radio bands. The pulsar emission is characterized by a plateau followed by a power-law decay (at times longer than the characteristic spin-down timescale). For a plateau luminosity comparable (but smaller) to the synchrotron power-law luminosity, the sum of the two contributions can lead to a luminosity with a less sharp power-law behavior than that of the pure synchrotron. The afterglow of GRB 171205A does not show any signs of a change in the power law of the synchrotron emission (see Figure 5), so we cannot constrain the magnetic field strength and structure. In Figure 5, we have adopted ≈47 ms as the initial rotation period of the νNS and a pure dipole field ($\xi = 0$) of $B_{\rm dip} = 10^{12}$ G to guide the eye of the reader. For magnetic fields $\gtrsim 5 \times 10^{13}$ G, the plateau luminosity of the pulsar emission contributes appreciably to the total X-ray luminosity affecting the goodness of the fit. Therefore, we can assume the above estimate as an upper limit to the dipole magnetic field. For the present synchrotron model parameters, X-ray data after times of a few 10^6 s could help constrain the presence of the pulsar emission. A sanity check of the model is that the energy injected into the ejecta is $\sim 10^{49}$ erg, of the same order as the rotational energy of the νNS, for a moment of inertia of a few 10^{45} g cm^2.

7. Conclusions

In this article, we have interpreted GRB 171205A within the BdHN model of long GRBs. In particular, because of the low energy release of only a few 10^{49} erg, we have classified GRB 171205A as a BdHN III, systems with long orbital periods, perhaps of the order of hours, in which the NS companion does not play any role in the cataclysmic event. Most of these binaries are also expected to be disrupted by the SN explosion (Fryer et al. 2015; Ruffini et al. 2016, 2018b). Under these circumstances, the GRB event is explained by the sole activity of the νNS and its interaction with the SN ejecta.

Here, we have shown that GRB 171205A is a low-luminous GRB consistent with it having been produced in the core collapse of a single CO star that forms the νNS and the type Ic SN. There are several new results related to the sequence of physical phenomena occurring in this system and the related GRB observables:

1. The fallback accretion is initially of a few of $10^{-3}\,M_\odot$ s^{-1} and lasts tens of seconds (Becerra et al. 2019, 2022). The accretion energy is $\sim 10^{52}$ erg, comparable to the kinetic energy of the SN ejecta. This energy is injected into the ejecta, propagates, and accelerates the outermost shell to the observed mildly relativistic velocity. The hydrodynamics is similar to the case of the expanding SN ejecta with the GRB energy injection presented in Ruffini et al. (2018c). The Lorentz factor of the shock wave is $\lesssim 5$ when it gets transparency at $\sim 10^{12}$ cm, and emits a thermal spectrum. This scenario explains the prompt emission of GRB 171205A. This is also similar to the cocoon scenario advanced for this source in Izzo et al. (2019). Both pictures predict the heating of stellar shells (in our case by the physical process of the fallback accretion originating from the SN explosion and in the other by the postulation of an unspecified jet) that get boosted to high velocity and emit a thermal spectrum. The associated blackbody emission has been indeed observed in GRB 171205A, and it has been inferred that ≈10^{-3} $M_\odot$ of material expands at velocities above 10^5 km s^{-1} (see Izzo et al. 2019 and Figure 2). The main difference between the two models is that in our picture there is no jet. This solution seems favored since the associated jet break expected in the afterglow of jetted GRB models is not observed in the data up to the last observations at ∼1000 days (Maity & Chandra 2021; Leung et al. 2021).
2. Regarding the afterglow emission, we have first inferred from an energy conservation argument, that the νNS should have started to lose its rotational energy at $t = 35$ s after the GRB trigger, i.e., from what we call the νNS rise, with a rotation period of 47 ms.
3. We have shown that the afterglow of GRB 171205A cannot be explained by the sole pulsar emission of the νNS by magnetic braking, even including higher multipole fields (e.g., quadrupole).
4. The multiwavelength afterglow is explained by synchrotron radiation emitted by electrons in the expanding SN, which is further powered by energy injected by the νNS. We have calculated the synchrotron luminosity in the X-ray, optical, and radio wavelengths with an analytic treatment of the above physical situation. We have shown that the X-rays and the radio luminosities follow the expectation from the synchrotron model. The rising part of the radio luminosity in the time interval of 10^6–10^7 s is due to synchrotron self-absorption (see Maity & Chandra 2021, for details). The observed optical luminosity shows a flat behavior followed by the bump of the optical SN powered by the energy release in the ejecta of the radioactive decay of nickel into cobalt. We have shown that the synchrotron luminosity in those optical wavelengths lies below the luminosity of the emergent SN optical emission. This implies that the observed optical emission contains the contribution of both the synchrotron radiation and the optical SN.
5. Another remarkable fact to be highlighted is that SN 2017iuk, an SN associated with the low-luminous GRB 171205A, a BdHN III, shows similar properties (e.g., peak luminosity and peak time) to the SNe associated with high-luminous GRBs (BdHN I and II). This suggests that the pre-SN progenitor (i.e., the CO star) is similar for all long GRBs, irrespective of their energetics (Y. Aimuratov et al. 2023, in preparation).
6. There is a corollary of the above result. In low-luminous GRBs, i.e., in BdHN III like GRB 171205A, the relatively slow rotation (47 ms period) of the νNS implies the lower amount of energy injected into the ejecta, hence, the low energetics of the associated synchrotron emission. Under these circumstances, the optical emission of the SN powered by the nickel radioactive decay is able to outshine the optical synchrotron luminosity.
7. We calculated the evolution of the νNS mass and angular momentum (assumed to be initially zero) during the fallback accretion process leading to its spinning up to the 47 ms rotation period. From this evolution, we have inferred that the SN explosion occurred at most 7.36 hr before the GRB trigger time. This sets an estimate of the time delay between the SN explosion and the electromagnetic emission of the GRB event, assuming a νNS born with zero spin.

We thank the Referee for comments and suggestions that helped us in the presentation of this article. L.M.B. is supported by the Vicerrectoría de Investigación y Extensión—Universidad Industrial de Santander Postdoctoral Fellowship Program No. 2022000293.

Appendix
Fitting Procedure

In this appendix, we describe how we set the value of the model parameters from the physical scenario and specific observables, including the attached uncertainties. The parameters to be specified are the index of the electron's energy injection, γ, the parameters defining the injected power k, L_0, and t_q, the maximum energy of the electrons, $E_{\rm max}$, the self-similar expansion timescale, t_*, the magnetic field at the initial time of reference of the expansion, $B_{*,0}$, and the νNS dipole magnetic field strength $B_{\rm dip}$. In Section 4, we have already fixed the νNS rotation period, $P_{\nu\rm NS}$. Our aim is to estimate the uncertainty in each parameter from the propagation of the 1σ uncertainty of the power-law fit of the X-ray and radio luminosities.

Equation (37) shows that the signature of the present synchrotron model is the power-law luminosity in the different bands with (ideally) the same power-law index. Therefore, we constrain the synchrotron model parameters using the observational data showing the above property. Figure 5 shows that the X-ray (0.3–10 keV) luminosity data behaves as a power law in the time interval of $t \approx (0.87\text{–}5) \times 10^6$ s, and the radio (1255 MHz) data in the time interval $t \approx (2.92\text{–}8) \times 10^7$ s. The two luminosities are fitted by

$$L_X = A_X\, t^{-\alpha_X}, \qquad L_r = A_r\, t^{-\alpha_r}, \tag{A1}$$

where $A_X = (3.165 \pm 0.238) \times 10^{47}$ erg s^{-1}, $\alpha_X = 1.022 \pm 0.055$, $A_r = (4.290 \pm 0.178) \times 10^{42}$ erg s^{-1}, and $\alpha_r = 0.616 \pm 0.081$. The uncertainties at 1σ level. To estimate the uncertainties in the value of the model parameters, derived from the above fit, we follow the standard theory of error propagation. For instance, given quantity f that is a function of the independent variables a_i, i.e., $f(a_1, a_2,...,a_n)$, its uncertainty can be estimated as (see, e.g., Ku 1966)

$$\delta f = \sum_{i=1}^{n} \sqrt{\left| \frac{\partial f}{\partial a_i} \right|^2 (\delta a_i)^2} \approx \sum_{i=1}^{n} \left| \frac{\partial f}{\partial a_i} \right| \delta a_i. \tag{A2}$$

Thus, the uncertainties of the luminosities given by the power-law fits, Equation (A1), at a time t, can be estimated by

$$\delta L_i \approx \left| \frac{\partial L_i}{\partial A_i} \right| \delta A_i + \left| \frac{\partial L_i}{\partial \alpha_i} \right| \delta\alpha_i = \frac{\delta A_i}{A_{i,c}} + |-\ln t|\, \delta\alpha_i, \qquad i = X,\, r, \tag{A3}$$

where $A_{X,c} = 3.165 \times 10^{47}$ erg s^{-1}, $A_{r,c} = 4.290 \times 10^{42}$ erg s^{-1}, $\delta A_X = 0.238 \times 10^{47}$ erg s^{-1}, $\alpha_{X,c} = 1.022$, $\alpha_{r,c} = 0.616$, $\delta A_r = 0.178 \times 10^{42}$ erg s^{-1}, $\delta\alpha_X = 0.055$, and $\delta\alpha_r = 0.081$.

We turn to the self-similar expansion timescale, t_*, for which we must set values for $R_{*,0}$ and $v_{*,0}$. For $v_{*,0}$, we chose a fiducial value according to numerical simulations of the SN explosion (see, e.g., Becerra et al. 2016, 2019), so we set $v_{*,0} = 10^8$ cm s^{-1} and there is no propagated uncertainty to calculate for. With the above, we set the expansion timescale and its attached uncertainty

$$t_* = \frac{R_{*,0}}{v_{*,0}}, \qquad \delta t_* = \frac{\delta R_{*,0}}{v_{*,0}}. \tag{A4}$$

According to our working assumption of uniform expansion, the inner radius and its uncertainty are

$$R_{*,0} = v_{*,0}\, t_{\rm SN}, \qquad \delta R_{*,0} = v_{*,0}\, \delta t_{\rm SN}, \tag{A5}$$

where $t_{\rm SN}$ is the time since the SN explosion given by Equations (28) and (32), and $\delta t_{\rm SN}$ its uncertainty. For the above expansion velocity $v_{*,0}$, and the time since the SN explosion estimated in Section 4, $t_{\rm SN} \approx 2.650 \times 10^4$ s $\approx$7.36 hr, we have $R_{*,0} \approx 2.65 \times 10^{12}$ cm and $t_* = t_{\rm SN} = 2.65 \times 10^4$ s. The uncertainty attached to the time $t_{\rm SN}$ can be estimated as

$$\delta t_{\rm SN} = \left| \frac{\partial t_{\rm SN}}{\partial \Omega_{\nu\rm NS}} \right| \delta\Omega_{\nu\rm NS}, \qquad \frac{\partial t_{\rm SN}}{\partial \Omega_{\nu\rm NS}} = \frac{1}{\omega} \frac{4\tilde{\alpha} - X}{2X - B} \frac{t_{\rm acc}}{1-p} [(1-X)^{\frac{p}{1-p}}], \tag{A6}$$

where X and B are given by Equations (29) and (30), evaluated at the time $t = t_{\nu\rm NS}$ s, so $\Delta\Omega = \Omega_{\nu\rm NS}$. The uncertainty in estimating $\Omega_{\nu\rm NS}$ from Equation (25) is given by

$$\delta\Omega_{\nu\rm NS} = \left| \frac{\partial \Omega_{\nu\rm NS}}{\partial A_X} \right| \delta A_X + \left| \frac{\partial \Omega_{\nu\rm NS}}{\partial \alpha_X} \right| \delta\alpha_X,$$
$$\frac{\partial \Omega_{\nu\rm NS}}{\partial A_X} = \frac{\Omega_{\nu\rm NS}}{2A_X},$$
$$\frac{\partial \Omega_{\nu\rm NS}}{\partial \alpha_X} = -\frac{\Omega_{\nu\rm NS}}{2} \left(\frac{1}{\alpha_X - 1} + \ln t_{\nu\rm NS} \right). \tag{A7}$$

For the present parameters, i.e., $t_{\nu\rm NS} = 35$ s and $\Omega_{\nu\rm NS} = 134.11$ rad s^{-1}, we obtain from Equation (A7), $\delta\Omega_{\nu\rm NS} \approx 185.795$ rad s^{-1}, so an uncertainty in the rotation period, $\delta P_{\nu\rm NS} = |\partial P_{\nu\rm NS}/\partial\Omega_{\nu\rm NS}|\delta\Omega_{\nu\rm NS} = 2\pi\delta\Omega_{\nu\rm NS}/\Omega^2_{\nu\rm NS} \approx 64.910$ ms. Using the above in Equation (A6), we obtain $\delta t_{\rm SN} \approx 110.276 \times 10^4$ s ≈ 306.220 hr. Thus, we get from Equation (A5), $\delta R_{*,0} \approx 110.276 \times 10^{12}$ cm, and from Equation (A4), $\delta t_* = \delta t_{\rm SN}$.

At large distances from the νNS, we expect the toroidal component of the magnetic field to dominate, which decays with distance as r^{-1} (see, e.g., Goldreich & Julian 1969). Assuming a toroidal field of the same order as the poloidal field near the νNS surface, its value at the radius $r = R_{*,0}$ is

$$B_{*,0} \approx B_{\rm dip} \frac{R}{R_{*,0}} = B_{\rm dip} \frac{R}{v_{*,0} t_*}, \tag{A8}$$

where $B_{\rm dip}$ is the strength of the dipole magnetic field and R is the fiducial νNS radius. As discussed in Section 7 the data does not constrain the dipole field but only sets an approximate upper limit of $B_{\rm dip,max} \approx 5 \times 10^{13}$ G. Therefore, we shall adopt a fiducial, conservative magnetic field value $B_{\rm dip} = 10^{12}$ G. By using a fiducial νNS radius $R = 10^6$ cm, and the value of $R_{*,0}$ given by Equation (A5), we obtain $B_{*,0} \approx 3.774 \times 10^5$ G. With the choice, Equation (A8), the attached uncertainty is given by

$$\delta B_{*,0} = B_{*,0} \frac{\delta R_{*,0}}{R_{*,0}} = B_{*,0} \frac{\delta t_*}{t_*} = B_{*,0} \frac{\delta t_{\rm SN}}{t_{\rm SN}}, \tag{A9}$$

which leads to $\delta B_{*,0} \approx 157.021 \times 10^5$ G.

We now set the index γ. From Equation (37), we infer that the ratio of the synchrotron luminosity at two frequencies, ν_1 and ν_2, is given by $L_{\rm syn}(\nu_1)/L_{\rm syn}(\nu_2) = (\nu_1/\nu_2)^{\frac{3-p}{2}}$, where $p = \gamma + 1$. Therefore, we can constrain the value of the index γ using the data in the X-rays and in the radio as

$$\gamma = 2\left[1 - \frac{\ln(L_X/L_r)}{\ln(\nu_X/\nu_r)}\right], \tag{A10}$$

where L_X and L_r are given in Equation (A1). Since the fitted power laws are not equal, the value of γ inferred from Equation (A10) depends on the time at which we calculate the ratio of the luminosities. Therefore, we adopt for γ the value given by the mean $\langle\gamma\rangle = \Delta t^{-1}\int\gamma dt$. We obtained $\langle\gamma\rangle \approx 1.6060$, where we have used $\Delta t \approx 8\times10^7$ s, $\nu_X = 10\,{\rm keV}/h \approx 2.423\times10^{18}$ Hz, and $\nu_r = 1255$ MHz. From Equation (A10), the uncertainty in the choice of γ can be estimated as

$$\begin{aligned}\delta\gamma &= \left|\frac{\partial\gamma}{\partial L_X}\right|\delta L_X + \left|\frac{\partial\gamma}{\partial L_r}\right|\delta L_r \\ &= \frac{2}{\ln(\nu_X/\nu_r)}\left(\frac{\delta L_X}{L_X} + \frac{\delta L_r}{L_r}\right),\end{aligned} \tag{A11}$$

whose mean for the above parameters is $\langle\delta\gamma\rangle = 0.231$.

The synchrotron emission peaks around the critical frequency

$$\nu_{\rm crit} = \alpha B_* E^2 = \alpha B_{*,0} E^2 \frac{t_*}{t}, \tag{A12}$$

and then cuts off exponentially, where E is the electron energy. Since the critical frequency decreases with time, there is a hard-to-soft evolution of the cutoff and the X-ray data give the strongest constraint. The electrons of maximum energy, $E_{\rm max}$, produce the maximum critical frequency, $\nu_{\rm crit,max}$. By requiring that $\nu_{\rm crit,max} = \nu_X$ at a cutoff time $t_{\rm cut,X} > t_{f,X}$, where $t_{f,X} \approx 3.5\times10^6$ s is the time of the last observational X-ray data, we obtain that the maximum electron energy must at least have the value

$$E_{\rm max} = \sqrt{\frac{\nu_X\, t_{\rm cut,X}}{\alpha\, t_*\, B_{*,0}}} = \sqrt{\frac{\nu_X\, \nu_{*,0}\, t_{\rm cut,X}}{\alpha\, B_{\rm dip} R}}, \tag{A13}$$

where in the last equality we have used Equation (A8). The cutoff time must allow the power-law luminosity to extend at least up to $t_{f,X}$. Thus, we chose $t_{\rm cut,X}$ such that the exponential cutoff at the time $t = t_{f,X}$ has reduced the power-law X-ray luminosity to one part in a thousand. With this condition, we find $t_{\rm cut,X} \approx 2.418\times10^7$ s, so $E_{\rm max} = 3.738\times10^4 m_e c^2$. Equation (A13) tells us that $E_{\rm max}$, chosen in this way, depends only on fiducial values that we have set for $\nu_{*,0}$, $B_{\rm dip}$, R, and $t_{\rm cut,X}$, so we cannot estimate an attached uncertainty to it.

Having set all the above parameters, it remains to set the parameters of the injected power, L_0, k, and t_q. The synchrotron luminosity increases at times $t < t_q$ (see Section 5.1) and decreases at times $t > t_q$. The X-rays' luminosity always shows a decreasing behavior, so we set $t_q = 100$ s, which roughly corresponds to the initial time of the X-ray data. For the parameters L_0 and k, we equate the model synchrotron luminosity, Equation (37), in the case of X-rays with the power-law luminosity (A1). From this equality, we obtain

$$\begin{aligned}k &= \frac{2 + 2\alpha_X - \gamma}{2}, \\ L_0 &= 2\frac{A_X}{t_*^{\alpha_X}}\frac{\gamma-1}{2-\gamma}\left(\frac{t_*}{t_q}\right)^k\left(\frac{t_{\rm cut},\ X}{t_*}\right)^{\frac{2-\gamma}{2}} \\ &= 2A_X\frac{\gamma-1}{2-\gamma}t_q^{-\alpha_X}\left(\frac{t_{\rm cut},\ X}{t_q}\right)^{\frac{2-\gamma}{2}},\end{aligned} \tag{A14}$$

where we have used Equation (A13). For the present parameters, we obtain k=1.219 and $L_0 = 1.011\times10^{47}$ erg s^{-1}. Therefore, we can estimate the error of the above quantities as

$$\begin{aligned}\delta k &= \left|\frac{\partial k}{\partial\alpha_X}\right|\delta\alpha_X + \left|\frac{\partial k}{\partial\gamma}\right|\delta\gamma = \delta\alpha_X + \frac{1}{2}\delta\gamma, \\ \delta L_0 &= \left|\frac{\partial L_0}{\partial A_X}\right|\delta A_X + \left|\frac{\partial L_0}{\partial\alpha_X}\right|\delta\alpha_X + \left|\frac{\partial L_0}{\partial\gamma}\right|\delta\gamma \\ &= L_0\left[\frac{\delta A_X}{A_X} + \ln t_q\,\delta\alpha_X + \left|\frac{1}{(\gamma-1)(2-\gamma)}\right.\right. \\ &\quad \left.\left. - \frac{1}{2}\ln\left(\frac{t_{\rm cut,X}}{t_q}\right)\right|\delta\gamma\right],\end{aligned} \tag{A15}$$

which read as $\delta k = 0.170$ and $\delta L_0 \approx 0.792 L_0 \approx 0.801\times10^{47}$ erg s^{-1}.

The large uncertainty in the estimate of t_* and $B_{*,0}$ is a consequence of the propagation of the uncertainty of $R_{*,0}$, which arises from the uncertainty in the estimate of the SN time, $t_{\rm SN}$, because it is sensitive to the function of $\Omega_{\nu{\rm NS}}$.

ORCID iDs

C. L. Fryer https://orcid.org/0000-0003-2624-0056
R. Ruffini https://orcid.org/0000-0003-0829-8318

References

Amati, L., Frontera, F., Tavani, M., et al. 2002, A&A, 390, 81
Arnett, D. 1996, Supernovae and Nucleosynthesis: An Investigation of the History of Matter from the Big Bang to the Present (Princeton, NJ: Princeton University Press)
Barniol Duran, R., Nakar, E., Piran, T., & Sari, R. 2015, MNRAS, 448, 417
Becerra, L., Bianco, C. L., Fryer, C. L., Rueda, J. A., & Ruffini, R. 2016, ApJ, 833, 107
Becerra, L., Cipolletta, F., Fryer, C. L., Rueda, J. A., & Ruffini, R. 2015, ApJ, 812, 100
Becerra, L., Ellinger, C. L., Fryer, C. L., Rueda, J. A., & Ruffini, R. 2019, ApJ, 871, 14
Becerra, L., Guzzo, M. M., Rossi-Torres, F., et al. 2018, ApJ, 852, 120
Becerra, L. M., Moradi, R., Rueda, J. A., Ruffini, R., & Wang, Y. 2022, PhRvD, 106, 083002
Bianco, C. L., Ruffini, R., & Xue, S.-S. 2001, A&A, 368, 377
Bloom, J. S., Frail, D. A., & Sari, R. 2001, AJ, 121, 2879
Campana, S., Beardmore, A., D'Ai, A., et al. 2017, GCN Circ., 22191, 1
Campana, S., Mangano, V., Blustin, A. J., et al. 2006, Natur, 442, 1008
Chen, W., Xie, W., Lei, W.-H., et al. 2017, ApJ, 849, 119
Cipolletta, F., Cherubini, C., Filippi, S., Rueda, J. A., & Ruffini, R. 2015, PhRvD, 92, 023007
Cipolletta, F., Cherubini, C., Filippi, S., Rueda, J. A., & Ruffini, R. 2017, PhRvD, 96, 024046
Cobb, B. E. 2017, GCN Circ., 22921, 1
Colgate, S. A. 1974, ApJ, 187, 333
Dai, Z. G., & Lu, T. 1998a, A&A, 333, L87

Dai, Z. G., & Lu, T. 1998b, PhRvL, 81, 4301
De Colle, F., Lu, W., Kumar, P., Ramirez-Ruiz, E., & Smoot, G. 2018, MNRAS, 478, 4553
de Ugarte Postigo, A., Izzo, L., Kann, D. A., et al. 2017, GCN Circ., 22204, 1
D'Elia, V., Campana, S., D'Aì, A., et al. 2018, A&A, 619, A66
D'Elia, V., D'Ai, A., Lien, A. Y., & Sbarufatti, B. 2017, GCN Circ., 22177, 1
Eisenberg, M., Gottlieb, O., & Nakar, E. 2022, MNRAS, 517, 582
Fraija, N., Pedreira, A. C. C. d. E. S., & Veres, P. 2019b, ApJ, 871, 200
Fraija, N., Colle, F. D., Veres, P., et al. 2019a, ApJ, 871, 123
Fryer, C. L., Benz, W., & Herant, M. 1996, ApJ, 460, 801
Fryer, C. L., Oliveira, F. G., Rueda, J. A., & Ruffini, R. 2015, PhRvL, 115, 231102
Fryer, C. L., Rueda, J. A., & Ruffini, R. 2014, ApJL, 793, L36
Goldreich, P., & Julian, W. H. 1969, ApJ, 157, 869
Gottlieb, O., Nakar, E., Piran, T., & Hotokezaka, K. 2018, MNRAS, 479, 588
Irwin, C. M., & Chevalier, R. A. 2016, MNRAS, 460, 1680
Izzo, L., Rueda, J. A., & Ruffini, R. 2012, A&A, 548, L5
Izzo, L., Kann, D. A., Fynbo, J. P. U., Levan, A. J., & Tanvir, N. R. 2017a, GCN Circ., 22781, 1
Izzo, L., Selsing, J., Japelj, J., et al. 2017b, GCN Circ., 22180, 1
Izzo, L., de Ugarte Postigo, A., Maeda, K., et al. 2019, Natur, 565, 324
Izzo, L., Auchettl, K., Hjorth, J., et al. 2020, A&A, 639, L11
Kardashev, N. S. 1962, SvA, 6, 317
Kasliwal, M. M., Nakar, E., Singer, L. P., et al. 2017, Sci, 358, 1559
Kathirgamaraju, A., Barniol Duran, R., & Giannios, D. 2016, MNRAS, 461, 1568
Ku, H. H. 1966, JRNBS, 70C, 263
Laskar, T., Hull, C. L. H., & Cortes, P. 2020, ApJ, 895, 64
Lehner, L., Palenzuela, C., Liebling, S. L., Thompson, C., & Hanna, C. 2012, PhRvD, 86, 104035
Leung, J. K., Murphy, T., Ghirlanda, G., et al. 2021, MNRAS, 503, 1847
Li, L., Wu, X.-F., Lei, W.-H., et al. 2018, ApJS, 236, 26
Li, L.-X. 2007, MNRAS, 375, 240
Longair, M. S. 2011, High Energy Astrophysics (Cambridge: Cambridge Univ. Press)
Maity, B., & Chandra, P. 2021, ApJ, 907, 60
Mastrano, A., Lasky, P. D., & Melatos, A. 2013, MNRAS, 434, 1658
Mészáros, P., & Rees, M. J. 2001, ApJL, 556, L37
Metzger, B. D., Giannios, D., Thompson, T. A., Bucciantini, N., & Quataert, E. 2011, MNRAS, 413, 2031
Moradi, R., Rueda, J. A., Ruffini, R., & Wang, Y. 2021a, A&A, 649, A75
Moradi, R., Rueda, J. A., Ruffini, R., et al. 2021b, PhRvD, 104, 063043
Nakar, E. 2015, ApJ, 807, 172
Nakar, E., & Piran, T. 2017, ApJ, 834, 28
Newville, M., Otten, R., Nelson, A., et al. 2021, lmfit/lmfit-py: v1.0.3, Zenodo, doi:10.5281/zenodo.5570790
Pacini, F., & Salvati, M. 1973, ApJ, 186, 249
Pétri, J. 2015, MNRAS, 450, 714
Planck Collaboration, Aghanim, N., Akrami, Y., et al. 2020, A&A, 641, A6
Pons, J. A., & Viganò, D. 2019, LRCA, 5, 3
Ramirez-Ruiz, E., Celotti, A., & Rees, M. J. 2002, MNRAS, 337, 1349
Rastegarnia, F., Moradi, R., Rueda, J. A., et al. 2022, EPJC, 82, 778
Rodríguez Castillo, G. A., Israel, G. L., Tiengo, A., et al. 2016, MNRAS, 456, 4145
Rueda, J. A. 2022, arXiv:2202.00316
Rueda, J. A., & Ruffini, R. 2012, ApJL, 758, L7
Rueda, J. A., & Ruffini, R. 2020, EPJC, 80, 300
Rueda, J. A., Ruffini, R., Karlica, M., Moradi, R., & Wang, Y. 2020, ApJ, 893, 148
Rueda, J. A., Ruffini, R., & Kerr, R. P. 2022a, ApJ, 929, 56
Rueda, J. A., Ruffini, R., Li, L., et al. 2022b, PhRv, 106, 083004
Ruffini, R., Rueda, J. A., Muccino, M., et al. 2016, ApJ, 832, 136
Ruffini, R., Karlica, M., Sahakyan, N., et al. 2018a, ApJ, 869, 101
Ruffini, R., Rodriguez, J., Muccino, M., et al. 2018b, ApJ, 859, 30
Ruffini, R., Wang, Y., Aimuratov, Y., et al. 2018c, ApJ, 852, 53
Ruffini, R., Moradi, R., Rueda, J. A., et al. 2019, ApJ, 886, 82
Ruffini, R., Moradi, R., Rueda, J. A., et al. 2021, MNRAS, 504, 5301
Rybicki, G. B., & Lightman, A. P. 1979, Radiative Processes in Astrophysics (New York: Wiley)
Soderberg, A. M., Kulkarni, S. R., Nakar, E., et al. 2006a, Natur, 442, 1014
Soderberg, A. M., Nakar, E., Berger, E., & Kulkarni, S. R. 2006b, ApJ, 638, 930
Soderberg, A. M., Berger, E., Page, K. L., et al. 2008, Natur, 453, 469
Soker, N. 2022, RAA, 22, 122003
Suzuki, A., & Maeda, K. 2022, ApJ, 925, 148
Suzuki, A., Maeda, K., & Shigeyama, T. 2019, ApJ, 870, 38
Tan, J. C., Matzner, C. D., & McKee, C. F. 2001, ApJ, 551, 946
Tiengo, A., Esposito, P., Mereghetti, S., et al. 2013, Natur, 500, 312
Urata, Y., Toma, K., Huang, K., et al. 2019, ApJL, 884, L58
Vianello, G., Lauer, R. J., Younk, P., et al. 2015, arXiv:1507.08343
Wang, Y., Rueda, J. A., Ruffini, R., et al. 2019, ApJ, 874, 39
Wang, Y., Rueda, J. A., Ruffini, R., et al. 2022, ApJ, 936, 190
Wang, J., Zhu, Z. P., Xu, D., et al. 2018, ApJ, 867, 147
Waxman, E. 2004, ApJ, 602, 886
Wei, J.-B., Figura, A., Burgio, G. F., Chen, H., & Schulze, H. J. 2019, JPhG, 46, 034001
Zhang, B., & Mészáros, P. 2001, ApJL, 552, L35
Zhang, W., Woosley, S. E., & Heger, A. 2004, ApJ, 608, 365
Zhao, L., Liu, L., Gao, H., et al. 2020, ApJ, 896, 42